Aalto University
School of Science
Master's in Advanced Materials for Innovation and Sustainability(AMIS)

Monish Chakravarty Rajkumar

Understanding the Effect of Heat Treatment on Microstructure and Mechanical properties of A205

Master's Thesis

GKN Aerospace
Trollhättan,
Sweden.

Supervisor: Dr. Ceena Joseph, GKN Aerospace
Prof. Robin Ras, Aalto University

Aalto University
School of Science
Master's Programme in Advanced Materials for Innovation and Sustainability

Aalto University
School of Science

ABSTRACT OF
MASTER'S THESIS

Author: Monish Chakravarty Rajkumar(ID: 728078)
Title:
Understanding the effect of heat treatment on microstructure and mechanical properties of A205

Date: 28-June-2019 **Pages**: 82

Major: Advanced Materials for Innovation and Sustainability **Code**: SCI3083

Supervisor(s):
Dr. Ceena Joseph (GKN Aerospace)
Prof. Robin Ras (Aalto University)

Advancements in aero-engine technology are constantly bringing down the operating temperatures of cold structures in engines. Aluminium alloys, having a low density and being significantly cheaper than Titanium alloys - which are currently being used for many cold structures, could potentially bring cost and weight savings. Aluminium A205 is one such recently developed castable Al-Cu-Mg-Ag(AMS4471) alloy containing in-situ formed TiB_2 and Al_3Ti particles, shown to have better mechanical properties at elevated temperatures(above 150^oC) relative to other high strength aluminium alloys.

In this thesis, a general understanding of the theory behind A205 has been developed. The effect of T7-heat treatment with a special interest on aging parameters on microstructure and hardness was understood. The change in mechanical properties of the T7-heat treated A205 after prolonged thermal exposures at 150^oC and 200^oC were investigated. The tensile properties at room temperatures and elevated temperatures were investigated. The Low Cycle Fatigue(LCF) properties of T7 heat treated A205 were investigated with fractography and the predominant initiators were identified. Fractography and EDS analyses were performed on fractured LCF and tensile tested specimens to reason out the fracture mechanisms and role of microstructural features on crack propagation on LCF life and tensile properties.

Applicability of ThermoCalc-Prisma to predict the precipitate($CuAl_2$) growth and coarsening during aging and prolonged thermal exposures was explored. A simple and functional tool that uses Larson-Miller Parameter has been proposed to predict the yield strength of T7 treated A205 after prolonged thermal exposures at temperatures less than 200^oC. Further to this, a mathematical tool to effectively optimize the aging temperature and time has been proposed and validated with experimental results.

Keywords: Aluminium, A205, MMC, Casting, LCF, Mechanical testing,

Language: English

Acknowledgement

I wish to express my gratitude to my supervisor Dr. Ceena Joseph at GKN Aerospace for her patience, understanding and support when I needed them. I would also like to thank everyone in the Design Engineering, Material Testing and Chemistry departments of GKN Aerospace for helping me get the results presented in the thesis work. I wish to extend my thanks to Team Extreme, especially Swerea(RISE), Jönkoping for the advice and training on SEM. I wish to thank my supervisor Prof. Robin Ras at Aalto University for being supportive with all the procedures from the beginning to the end of my thesis.

Trollhättan,

30-June-2019

Monish Chakravarty Rajkumar

Abbreviations

YS	Yield strength
UTS	Ultimate tensile strength
LCF	Low cycle fatigue
MMC	Metal Matrix Composite
SEM	Scanning Electron Microscope
EDS	Energy Dispersive Spectroscopy
TEM	Transmission Electron Microscope
AR	Aspect ratio
HIP	Hot Isostatic Pressing
Wt%	Weight-percent
Vol%	Volume-percent
CTE	Coefficient of Thermal Expansion

Contents

Chapter 1

Introduction

Materials research in aerospace industries is centered on reducing weight and increasing service life of components while not compensating on reliability. Therefore, aerospace industries tend to focus on material systems with high specific strength, sensible manufacturing cost and reproducible quality. In terms of density, aluminium has a density that is about one-third that of steel. With moderate strength, aluminium alloys show considerably high corrosion resistance. These factors have motivated aerospace industries to use a lot of aluminium alloys since 1930s. Aerospace industries ever since their incipient stages have explored the advantages of aluminium. It is interesting to note that precipitation hardened Al-8Cu(wt%) alloy was used in the historic first flight of Wright Brothers in 1903. Tons of duralumin, an Al-Cu-Mg alloy was used by Germans during the world war I in zeppelins[1].

Although aluminium has a high strength to weight ratio relative to other metallic alloys, one of its drawbacks is its loss of strength at elevated temperatures. Especially in aero-engine components, the temperatures could be quite high for aluminum alloys to retain their strength.

Titanium alloys known for their specific strength at elevated temperatures often overshadow aluminium alloys forcing Aerospace industries to prefer titanium alloys over aluminium for several applications. However, high-quality aluminium alloy systems like A201.0 and A357.0 with enhanced mechanical properties have kept research on aerospace grade aluminium alloy development alive. Titanium alloys like Ti-6Al-4V and aluminium alloys like A201 and A357 are used to construct several aero components. The operating temperatures of these parts can be as high as 150^{o}C eliminating most of the aluminium alloys from being used for this purpose. In general, titanium alloys are also more expensive than aluminium alloys because of their manufacturing coasts. At times, high strength is not required. For example, a component made of Ti-6Al-4V that has roughly twice the strength than what is required by design and can very well be replaced by a cast aluminium alloy, provided it possess the desired strength at the operating temperature. It has also been identified that, with constantly advancing aero-engines, the hot part of engines are getting hotter while the cold parts are getting colder opening more possibilities for aero-engine manufacturers to use aluminium alloys.

While A201 and A357 could be potential candidates for weight and cost savings, they have some problems rendering them incompetent against the conventional titanium alloys. Aluminium alloy A201

has shown very good mechanical properties[2] but poses several casting issues such as susceptibility to porosity. On the other hand, Al-Si alloys such as A357 have a good castability[2] but do not retain their room temperature mechanical properties at elevated temperatures. This provides space for research on aluminium to develop an alloy that has better mechanical properties at elevated temperatures and is also castable. The Aluminium A205 is an alloy recently developed and commercially available that has shown promising qualities for aerospace applications. A205 is a heat treatable metal matrix composite with an Al-Cu-Mg-Ag matrix reinforced with in-situ formed TiB_2 particles. It could be said that A205 is more developed derivative of A201 in terms of castability and strength. The advantageously formed second phase particles(Al_3Ti and TiB_2) allows the alloy to have an unique solidification mechanism refining the grain structure. Over the past several decades, metallic composites have been well researched and noticed to constantly replace non-composite metallic systems widely especially in aerospace. Aluminium alloys having a lot of space for improvement have invited researchers to explore aluminium metal matrix composites to enhance mechanical properties.

1.1 Problem statement

GKN Aerospace has been constantly looking for opportunities to reduce weight and cost of aero-engine components. As already stated, with more and more advancements the colder part of engines are getting colder. This opens up possibilities for replacing alloys such as Ti-6Al-4V which are heavy with less weighing alternatives – aluminium alloys. The main drawback of high strength aluminium alloys are their inability to maintain the high strength at elevated temperatures(above 150^{o}C). As the operating temperatures are going down, GKN Aerospace has gained interest in a recently developed cast aluminium alloy A205 that could potentially replace heavier materials for cold-structures such as Ti-6Al-4V. Since A205 is castable, it would also cut down the manufacturing costs significantly. In aerospace industries, it is very important to have the mechanical properties of the materials properly investigated before implementing them into the actual component. The mechanical response of the alloy at different conditions including real operating conditions had to be justified with scientific reasons. This thesis entails the theoretical background on grain refining and other strengthening mechanisms in A205 and discusses the experimental results on how the precipitation strengthening and overaging affects the mechanical properties.

In the last two decades with the development of softwares such as ThermoCalc and JMatPro, Integrated Computational Materials Engineering(ICME) has attracted a lot of attention. Since the final strength of the alloy system in consideration depends on the precipitation characteristics during heat-treatment, it

would be an effective tool if the precipitation of $CuAl_2$ plates could be simulated and then related to the yield strength at different conditions. This would pave way for predicting the yield strength of the alloy during aging and after prolonged exposures at elevated temperatures. It would hopefully define the service life of the component at a chosen operating temperature. Testing the material experimentally after very long times such as 10,000 h can be unfeasible. The applicability of PRISMA module of ThermoCalc to predict the precipitation characteristics is tested in this thesis work. Owing to the complexity and absence of material parameters readily available in Prisma, alternatives to optimize the aging process and to predict the yield strength after prolonged thermal exposures had to be found. To this extent, one tool involving LM-Parameter has been proposed to predict yield strength after prolonged thermal exposures.

The heat-treatment process was taking a long time, and opportunities to bring the heat-treatment time down were to be found. One other mathematical tool was also found out in order to optimize the aging process.

1.2 Structure of the thesis

The next chapter of thesis will introduce a brief background to aluminium alloys, followed by the strengthening mechanisms operating in A205 alloys, effect of various alloying elements in A205. The background will include systematic presentation of various literature on similar topics, with special interest on A201 and how it compares with A205. The chapter 2 emphasizes the effect of TiB_2 and other phases formed in the alloy on the mechanical properties of A205.

The third chapter will give the experimental conditions and methods followed to perform each test/experiment.

The fourth chapter presents the results and discusses them. The effect of heat treatment on microstructure and hardness is discussed first. Then, the mechanical response of the alloy at estimated and exceeding operating temperatures(150^oC) are discussed. The mechanical properties under focus are tensile properties – tensile strength, yield strength and elongation, and Low Cycle Fatigue(LCF) life. The results include appropriate fractographs and most predominant defects initiating fatigue cracks. In the third phase, the results of ThermoCalc simulations are presented and their accuracy is discussed.

The fifth chapter lists the conclusions drawn from the thesis work.

Chapter 2

Background

2.1 Aluminium and its alloys

Aluminium owing to its remarkable strength to weight ratio has attracted a lot of industries and researchers ever since its discovery. Table 2.1 gives an overview of properties of light-weight metallic systems – Aluminium, Magnesium and Titanium compared to Steels as a reference. Aluminium alloys being cost effective and light-weight dominates over magnesium alloys. However, they can only be considered as tough competitors against titanium alloys which perform better at both room and high temperatures unlike aluminium alloys which become too weak at elevated temperatures. Sometimes, the best specific strength and capacity to retain the strength at very high temperatures are not required by design which opens up possibilities for aerospace industries to have cast aluminium in some components to cut down weight and cost.

Table 2.1. *Summary of advantageous properties of Aluminium alloys compared against Magnesium and Titanium alloys and Steels*[3]

Alloy	Density ρ (Mg m^{-3})	Young's Modulus E (GN m^{-2})	Yield Strength σ_y (MN m^{-2})	E/ρ	σ_y/ρ	Creep temperature (°C)
Al alloys	2.7	71	25-600	26	9-220	150-250
Mg alloys	1.7	45	70-270	25	41-160	150-250
Ti alloys	4.5	120	170-1280	27	38-280	400-600
(Steels)	(7.9)	(210)	(220-1600)	27	28-200	(400-600)

2.1.1 Cast Aluminum alloys

Based on how the alloys are fabricated, aluminium alloys can be broadly classified as cast and wrought alloys. Since this thesis work is on cast aluminum alloy A205, discussions are focused on cast alloys, although most strengthening mechanisms apply in general irrespective of the type. Although wrought alloys are in general stronger than cast alloys, thicker sections such as ribs and bosses are easier to be cast than machined, with the desired mechanical properties. Challenges in casting center on selecting the right casting parameters. Casting parameters have a phenomenal effect in defining the properties of

the product by defining its microstructure. Like all other metallurgical processes, the solidification microstructure derives from thermodynamics and kinetics.

It should be noted that the alloying elements influence the mechanical properties of the alloy and in most cases decide the capacity to improve properties by post processing. In the following section, different strengthening mechanisms in metallic alloys are discussed.

2.2 Alloying in Aluminium alloys

Pure aluminium has very low strength($\sigma_{0.2}$ < 60 MPa) which necessitates the need for alloying. Every element present in an aluminium alloy other than aluminium can be classified into three principal groups: basic alloying elements, ancillary elements(dopants) and impurities.

In the domain of aluminium alloys, there are only four major alloying elements: magnesium(Mg), zinc(Zn), copper(Cu), silicon(Si). Al-Si alloys are the most studied cast alloys known for their mechanical properties and castability. The 'basic' alloying element is the one that contributes most significantly to the properties of the alloys irrespective of its weight fraction. For example, in an Al-Si alloy with around 7% Si and 0.3% of Mg, it is Mg that define the strength thereby makes it a basic alloying element despite its small amount[4].

All the principal alloying elements form eutectic phase diagrams with aluminium. This easily restricts the major binary combinations to four groups[4]:

1. Solid solution type: Characterized by presence of non-equilibrium degenerate eutectic reation which is manipulated by heat-treatment processes. One good example would be Al-Cu alloy in which non-equilibrium nano/micro-precipitates are used to strengthen the alloy rather than using the natural eutectic phase that forms in equilibrium conditions.
2. Hypo-eutectic: The majorly used Al-Si alloys with Si content less than 12% fall in this category.
3. Eutectic: The binary eutectic phase primarily forms the whole microstructure – for example, Al-12%Si alloy.
4. Others: Alloys with primary crystals of constituent particles - for example, less common hyper-eutectic Al-Si castings

Figure 2.1 shows where the above four types fit in a typical eutectic diagram and the compositions that are preferred to be cast or wrought. (Al), commonly represented as α-Al is the aluminium rich phase while β is the solute rich phase.

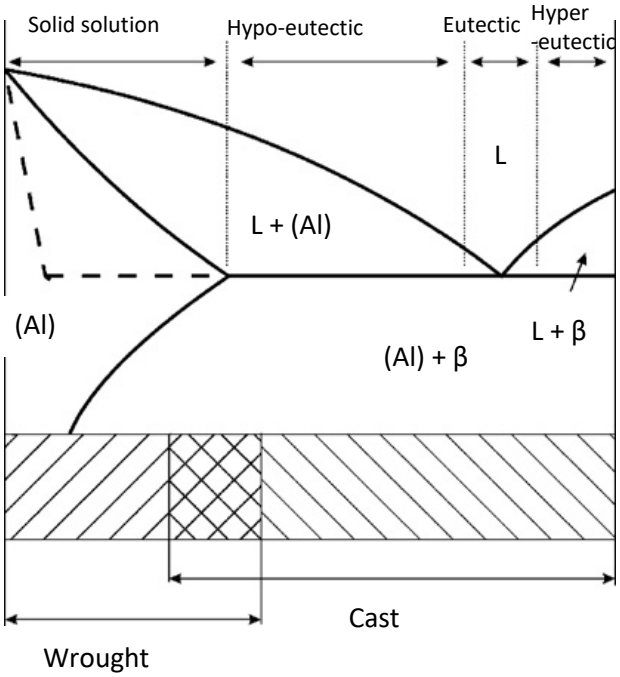

Figure 2.1. *Schematic of a binary phase diagram Al–X (2nd component) of eutectic type*[4].

Usually, aluminium alloys used in industries are not binary and are more complex with several alloying elements. It is interesting to note that, elements like iron(Fe), which are added in small amounts to improve castability might form some phases with principal alloying elements thereby influencing the properties of the cast product.

From a chemical perspective under equilibrium conditions, the interaction between alloying elements and aluminium can be understood from corresponding phase diagrams. In order to understand how the alloying elements affect the strength of the alloy, the next section briefly discusses the various strengthening mechanism operating in A205 and the roles various alloying elements play in deciding the strength of the alloy.

2.3 Strengthening mechanisms

2.3.1 Solid solution strengthening

Some elements dissolve in aluminium to certain temperature-dependent compositions as dictated by their phase diagrams and harden the alloy. The solute atoms in the solution, differing in size, stiffness and charge from the solvent atoms are randomly distributed in the FCC lattice of aluminium. The strain

fields that are created around them as a result of 'mismatch' in the lattice thwart the motion of dislocations, therefore, impart strength.

The increased yield strength varies proportionally with the solute concentration and the magnitude of mismatch between solute and solvent as defined by[3]:

$$\sigma_y \, \alpha \, \varepsilon_s^{3/2} C^{1/2} \qquad \text{…Exp. 2.1}$$

where C is the solute concentration, ε_s represents the lattice strain created by the solute and σ_y is the yield strength of the alloy.

2.3.2 Grain boundary strengthening

Grain boundaries in any polycrystalline metal are regions of disorder that thwarts dislocation motion. Therefore, by refining the grains, the area of grain boundaries increase, and the alloy strengthens. This phenomenon was explained by Hall-Petch who mathematically related the yield strength to grain size as[5]

$$\sigma_y = \sigma_o + k d^{-\frac{1}{2}} \qquad \text{…Exp. 2.2}$$

where σ_y is the yield stress, σ_o is the friction stress when dislocations glide on the slip plane, d is the average grain size, and k is the stress concentration factor.

It is interesting to note that, of all the strengthening mechanisms operating in polycrystalline metals, grain refining is the only one which can improve both strength and toughness. All other strengthening mechanisms increase strength while compensating on toughness.

2.3.3 Precipitation strengthening

Precipitation strengthening is the primary mode of strengthening in A205 which makes it an important topic of focus in this thesis work. The strengthening mechanism involves increasing the resistance to dislocation motion by precipitating second phase particles in the alloy matrix. This requires that the second phase is soluble at an elevated temperature and the solubility is significantly reduced at lower temperatures. The elevated temperature at which the second phase is soluble in the alloy matrix is usually chosen as 'solutionizing temperature'. After solutionizing, the microstructure of the matrix is frozen with the dissolved second phase by rapid cooling(usually water or polymer quenching) and then

'aged' naturally or artificially by leaving it in room temperature, or heating it well below the solvus temperature to precipitate the second phase as small precipitates. In a typically precipitation strengthened Al-Cu system, the second phase precipitates would be Al_2Cu. This precipitation mechanism will be discussed in detail in Section 2.4.1. Various interaction mechanisms between dislocation and particles have been proposed to explain the strengthening: particle bypassing by Orowan looping, bypass slip and particle shearing[6,7].

2.3.3.1 Dislocation-Particle Interaction

The second phase particles in the metal matrix creates a strain field in the lattice that pins the dislocations approaching them. Figure 2.2 shows a simple schematic of forces on a dislocation interacting with a second phase particle. F is the resistance to dislocation motion offered by the particle and T is the line tension of the dislocation.

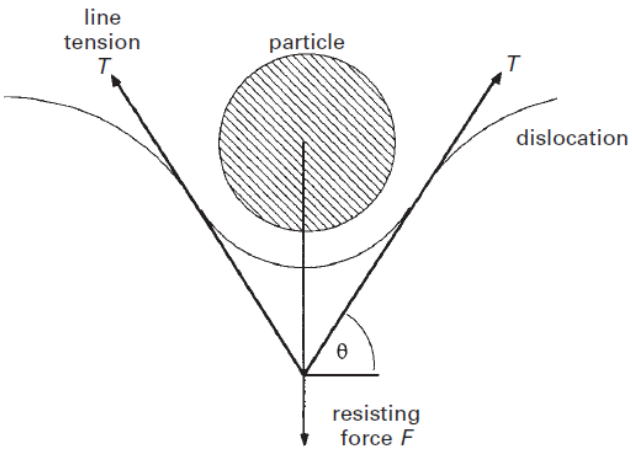

Figure 2.2. *Forces acting on a dislocation interacting with a particle/precipitate.*[7]

If the forces on the dislocation are in equilibrium, then the forces would satisfy the equation:

$$F = 2T \sin \theta \qquad \ldots \text{Exp. 2.3}$$

The degree of bowing θ increases as F increases, and when θ reaches π/2 radians, F reaches its maximum. At this point, two scenarios can be imagined with respect to the resistance offered by the particle:

1. When the particle is not hard, such that maximum resistance has been attained before θ reaches π/2 radians, the particle will be sheared by the dislocation. This mechanism is associated with

coherent particles with coherency strain fields. With a lower resistance offered by the particle, θ in figure 2.1 tends to zero.

2. When the particle is so hard, such that F exceeds 2T, then dislocations can bypass the particle either by Orowan looping or cross-slip and the particle will remain intact.

   Orowan mathematically related the increase in yield strength brought by a dislocation with a burger vector b in a metal matrix with shear modulus G and interparticle spacing L[7]:

$$\Delta\tau_y = Gb/L \qquad \ldots\text{Exp. 2.4}$$

The two scenarios of interaction are represented in figure 2.3. When the interaction is by Orowan looping, a dislocation loop is left behind around the particle. These loops can further add strength by creating a strain field themselves thereby hurdling more dislocations.

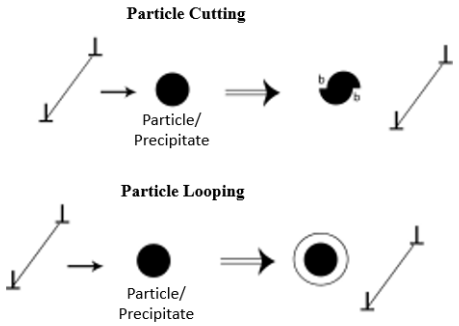

Figure 2.3. *A dislocation interacting with a shearable particle (top) and unshearable particle (bottom).*

When the dislocations interact with the particles in a particle-cutting scenario, the strengthening mechanism operating behind might not be one but several. The mechanisms are briefly presented below:

1. Coherency hardening: Precipitates precipitating from super-saturated matrices are usually coherent and the small atomic volume difference between precipitates and the matrix results in coherency strain. The stress field created as a result of this strain can thwart dislocation motion.
2. Modulus strengthening: As a result of difference in shear modulus between the precipitates and the matrix, the dislocation line tension alters as it shears through the precipitate.
3. Chemical strengthening: As the dislocation shears through the precipitate, new precipitate/matrix interfaces are created and this needs energy

One more important effect associated with interaction of dislocation with coherency strains is the when the dislocation bends to lie in low energy positions as shown in figure 2.4. The distortion of dislocation can make it difficult to theoretically calculation of contributions from different mechanisms.

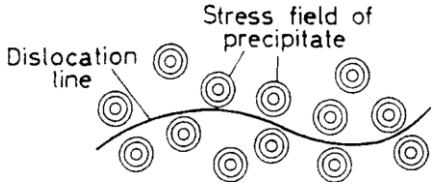

Figure 2.4. *A distorted dislocation line as a result of interaction with various stress fields in the alloy.*[7]

2.4 Effect of alloying elements present in A205

2.4.1 Effect of Copper

Copper(Cu) as an alloying element contributes to the strength by two mechanisms – solid solution strengthening and precipitation/age-hardening that is taken advantage of by solution heat treatment. Figure 2.5 shows the Al-Cu phase diagram. It could be seen for compositions with less than 5.7% copper that, at elevated temperatures, copper forms a solid solution with aluminium while at lower temperatures, the solubility decreases forming the second phase of binary eutectic $CuAl_2$. By solution heat treatment and aging, $CuAl_2$ can be precipitated out as small particles in the metal matrix bringing precipitation hardening into picture. However, since this transformation happens at a low temperature, the thermodynamics and kinetics compensate making the transformation happen in four distinct stages.

Figure 2.6 shows the four distinct stages involved in the precipitation of $CuAl_2$ from the super-saturated matrix. In the first stage(Figure 2.6b), disk-shaped GP zones nucleate homogeneously in the supersaturated solid solution. The disk faces are perfectly coherent with almost no coherency strain but the edges are coherent with a large coherency strain. The GP zones grow to form θ'' precipitates(Figure 2.6c) and has similar coherency conditions with the matrix as GP zones. Precipitates called θ' precipitate at dislocations and consume θ'' as they grow(Figure 2.6d). The disc faces of these θ' precipitates are still coherent but the edges become incoherent. Finally as the system gets close to the equilibrium stage, θ' because of the elastic strains around it generate a complex dislocation network. This stage marks the loss of coherency of θ' precipitates, thereby forming θ phase[8](Figure 2.6e). The $CuAl_2$ now formed is completely incoherent with the matrix making it grow as rounded rather than

disk-shaped particles[3]. In the whole process of precipitation, GP zones and θ'' disks generate stresses that thwart dislocation movement. This process is called coherency stress hardening. Precipitation hardening effect brought by θ' precipitates is dependent on their interaction scenario with the dislocations. The evolution of hardness over time typically looks like Figure 2.7. The early stage of hardening can be attributed to GP zone formation and θ'' formation adds to the hardening effect. The maximum hardness is when θ' co-exists with θ''. On overaging, θ' coarsening reducing the hardness[8]. Precipitation heat treatment is generally performed at low-temperature and long-times depending on the optimum precipitate size and distribution. In general, choosing a higher aging temperature allows for peak strength to be achieved early than aging at a lower temperature. But the number density of precipitates will be lesser allowing more dislocation to slip away. This reasons out why choosing a higher aging temperature results in a lower peak strength[2].

Depending on the properties required, the heat treatment cycles that involve a solutionizing step and an aging step has to be tailored appropriately. For the A205 alloy of interest, a T7 heat treatment has been set by specification. The T7 heat treatment involves solutionizing and slightly overaging the material. This means that the $CuAl_2$ precipitates are aged past the peak hardness. The advantages of T7 heat treatment are improved resistance to stress corrosion cracking, and an improved ductility. On the other hand, there is a compensation on tensile and yield strength[2].

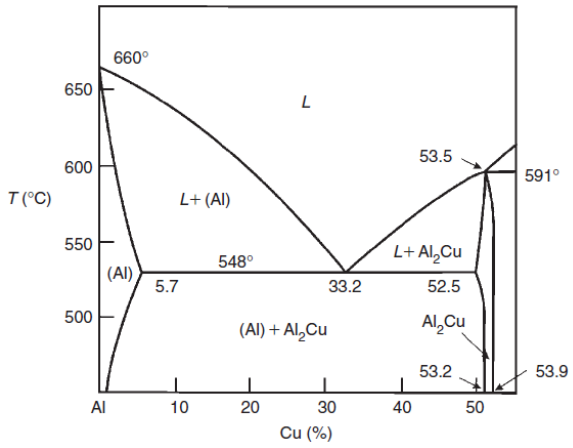

Figure 2.5. *Al-Cu phase diagram*[4]

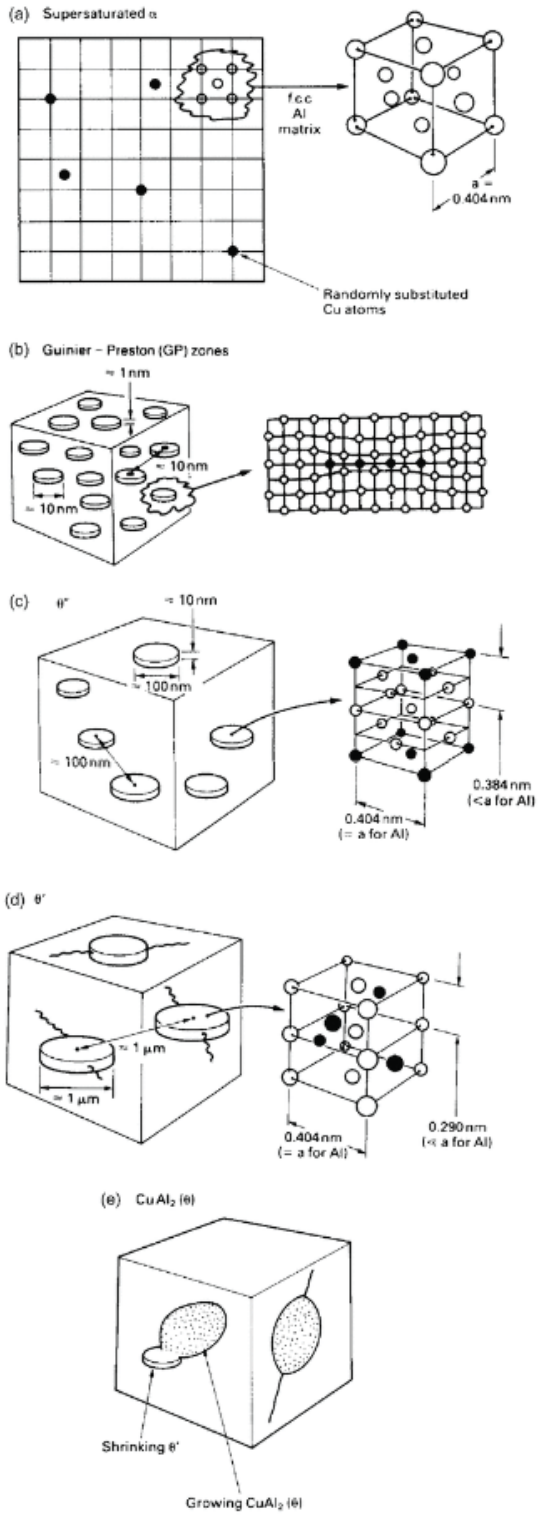

Figure 2.6. *Precipitation of $CuAl_2$ out of supersaturated α matrix through various transition stages - Formation of (a) Cu clusters in the supersaturated α matrix (b) GP zones (c) θ'' precipitates (d) θ' precipitates (e) θ phase.* [3]

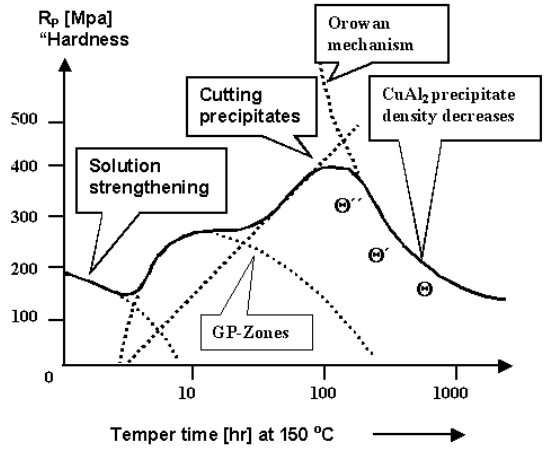

Figure 2.7. *Evolution of strength during aging in an Al-4%Cu alloy*[9]

2.4.2 Effect of Magnesium

In small quantities, magnesium(Mg) has been found to be effective in strengthening aluminum by solid solution strengthening. Atomic size mismatch is one important parameter that defines the solid solution strengthening effect. With Mg, the atomic size mismatch relative to aluminium is as high as 11.7% allowing it to enhance the strength of aluminium by 30-40 MPa for 1 atomic weight percent. Although the phase diagram(figure 2.8) suggests that the solubility of Mg in Al at room temperature is only 1.8 wt% after which Al_8Mg_5 forms, FCC structure of Al can be forced to withhold up to 5.5 wt% of Mg dissolved in a non-equilibrium state. This is made possible by heating the alloy to a homogenous solution state at around 450°C and cooling it quickly so that the dissolved Mg atoms do not have the driving force to precipitate out as Al_8Mg_5 but stays supersaturated in the matrix[3]. They have a low thermal stability and they do not possess good castability. On the bright side, it improves the corrosion resistance of the alloy. Al-Mg alloys are preferred to be wrought and not often cast[4].

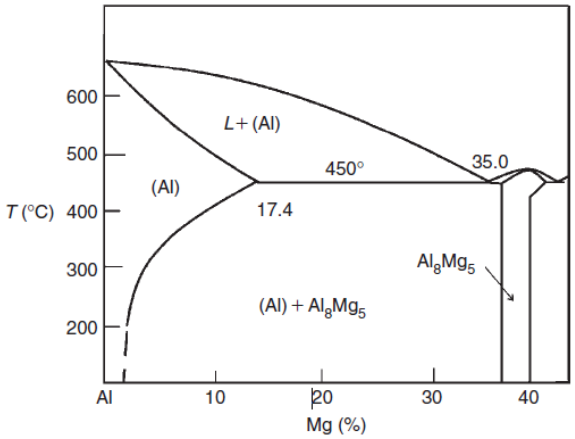

Figure 2.8. *Al-Mg phase diagram*[4]

2.4.2.1 Effect of Mg in Al-Cu alloys

Precipitation strengthening being widely attractive with aluminium alloys, Al-Cu-Mg systems has attracted a lot of research. Magnesium increases the peak strength attainable by aging Al-Cu alloys and just about 0.5% of Mg effectively alters the aging characteristics of the alloy[2]. They also show an improved fatigue damage resistance making it employable in the aerospace industry[10]. It is believed that, Mg and Cu solute atoms form co-clusters on {111} planes of the matrix and the interaction of these co-clusters with vacancies may intensify the aging process. The formation of clusters has also been attributed to increased fatigue strength[11]. At elevated temperatures like the θ' precipitates in Al-Cu alloys, there is a transition phase S'(Al_2CuMg) that forms which are coherent on {021} plane of the matrix. Overaging leads to a loss of coherency forming S phase. This has not been observed with small additions of Mg, the determining factor being the Cu:Mg ratio[12]. Liu et al has reported that depending on the Cu:Mg ratio, the fraction of precipitating phases θ' or S can be affected[13]. A plausible reduction if precipitation kinetics of θ' by presence of S phase has also been proposed.

2.4.3 Effect of Silicon and Iron

Aluminium-Silicon(Si) systems are known for their castability. Although solubility of silicon in aluminium varies with temperature, they are not prone to precipitation strengthening. They are made heat treatable by addition of Cu or Mg. A classic example in aerospace industry being A357 is an Al-Si-Mg system. The Al-Si eutectic that defines the property of the alloy is what is attractive in Al-Si systems[14]. In A205, only small amounts of silicon and iron are present(<0.1%). Fe is usually deliberately added in die-cast alloys to enable easy ejection of the cast part from the mould. Si and Fe in this case might as well be considered as impurities. In equilibrium, literature suggest formation of two phases – $FeSiAl_8$(appear as Chinese script) and $FeSiAl_5$(appear as thin platelets that in section appear as long needles [15].

The presence of iron can be rather significant as an additive or impurity when present over 0.5%. The effect of excessive fraction of iron is nullified by tying it up with Si forming αFeSi. Else, Fe would reduce the amount of Cu available for strengthening by forming Cu_2FeAl_7[2].

2.4.4 Ancillary additions

Most alloys in industries have "ancillary additions" in the order of 10^{-2}-10^{-1}%. These additions are usually transition and rare earth metals such as Mn, Ti, Cr, V, Ni, Fe, Ce, Sc and occasionally Be, Cd and B. These elements usually form eutectic or peritectic phase diagrams with aluminium. Mn is a

widespread ancillary addition in amounts from 0.1% to 1%[4]. In the topic of interest, Ag acts as an important ancillary addition that significantly improves the mechanical response of the alloy at elevated temperatures.

2.4.4.1 Effect of silver on Al-Cu-Mg alloys

Silver is an important addition in A205. Effect of silver as an ancillary addition on Al-Cu-Mg alloy has been arguable, although it has been apparent that Ag improved the mechanical response of the alloy at elevated temperatures[16-18]. Julian et al has suggested that, in binary Al-Cu alloys, the improved properties are due to reduced coarsening of θ' precipitates due to Ag atoms migrating to precipitate-matrix interface[19]. A201 is an Al-Cu-Mg-Ag alloy which has been proved to have a very good mechanical strength between room temperature and 200ºC among the cast Al alloys[15]. These added properties are attributed to the precipitation of $CuAl_2$ as Ω on {111} matrix planes instead of θ' on {100} planes. Aluminium having an FCC structure are strengthened more by having obstacles to dislocation motion on the {111} plane rather than {100} planes. Ω precipitates has also shown better coarsening resistance compared to θ'. Chemically, Ω precipitates have a composition close to $CuAl_2$. Knowles and Stobbs pointed out that Ω has a face-centered orthorhombic structure[20]. By using a 3D atom probe field ion microscope, Reich et al published experimental evidence suggesting the formation of co-clusters of Ag and Mg aligned on {111} planes of the matrix promoting Ω precipitation[21]. Hutchinson et al has studied the coarsening characteristics of Ω precipitates at different temperatures[22]. It was published that, on prolonged exposure at 200ºC for 100 h, the precipitates' thickness did not noticeably coarsen above 5.5 nm (average). At 250ºC, it increased to 25-30 nm after 1000 h while the rate of coarsening turned rapid at 300ºC. Figure 2.9 shows a TEM image of θ' and Ω precipitates in a precipitation hardened Al–4Cu–0.3Mg–0.4Ag (weight %) alloy after solutionizing and aging for 10 h at 250ºC[22]. J Forde has extensively investigated the effect of prolonged elevated temperature exposures on mechanical properties of A201 alloy[23]. He has reported a notable decrease in yield strength and an increase in elongation after exposing T7 treated A201 at 205ºC for 1000 hours. The reason has been attributed to Ostwald ripening of Ω precipitates. Gazizov et al has estimated that, by precipitating $CuAl_2$ as Ω precipitates instead of θ' precipitates could improve the yield strength by a factor of ~2.8 to ~3.4[24].

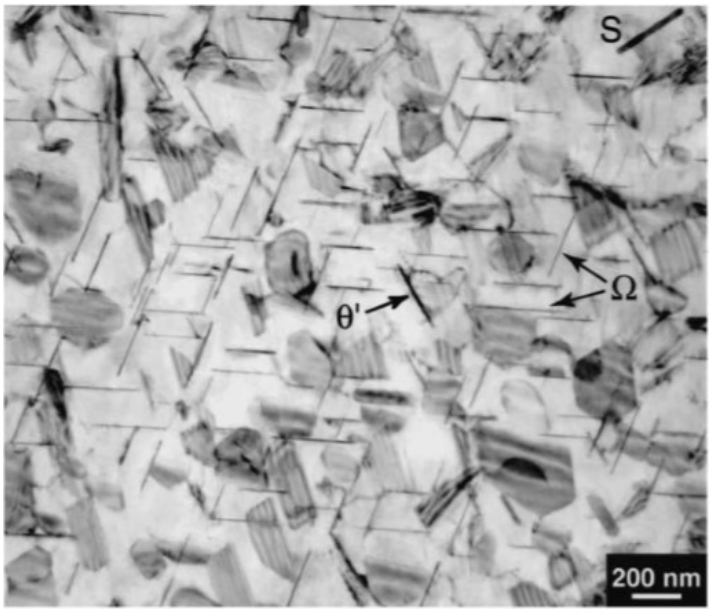

Figure 2.9. *Bright field TEM image of θ' and Ω precipitates in an Al–4Cu–0.3Mg–0.4Ag (wt. %) alloy after solutionizing and aging at 250°C for 10 h.*[22]

2.5 Aluminium/TiB_2 Metal Matrix Composites

With aluminium metal matrix composites(MMCs) becoming the trend in last few decades, researchers tended to improve the strength of aluminium with ceramic particle reinforcements [25,26]. Among various reinforcement particles such as SiC, Al_2O_3, B_4C, TiB_2, ZrB_2 etc, TiB_2 has been profoundly found to be effective in strengthening Al alloys[27]. The widely used process for in-situ formation of TiB_2 by casting uses a salt-melt reaction between K_2TiF_6 and KBF_4 and Al melt[23,28,29]:

$$2\,KBF_4 + 3\,Al \rightarrow 2\,KAlF_4 + AlB_2 \quad \text{…Eqn. 2.1}$$

$$3\,K_2TiF_6 + 13\,Al \rightarrow 3\,KAlF_4 + K_3AlF_6 + 3\,Al_3Ti \quad \text{…Eqn. 2.2}$$

$$AlB_2 + Al_3Ti \rightarrow 4\,Al + TiB_2 \quad \text{…Eqn. 2.3}$$

2.5.1 Solidification of Aluminium/TiB_2 MMCs

Depending on the characteristics of the melt and reinforcement particles, the particles are either engulfed or pushed away during solidification. Particle engulfment would lead to a uniform distribution of particles, while if they are being pushed away, the particles would segregate to regions that solidified in the end – typically, grain boundaries or inter-dendritic regions. The velocity at which the

solidification front propagates in the melt mainly decides if the reinforcement particles are engulfed or pushed[30,31]. While that applies for reinforcement particles, Ti and B have been widely used as grain refiners. TiB_2 shows a high coherency with aluminium facilitating heterogeneous nucleation along their {0001} faces with aluminium alloy as a result of reduced interfacial energy. Schaffer et al has extensively studied the orientation relationships between engulfed TiB_2 particles and the matrix in Al alloys[31,32]. There are studies that suggest that, TiB_2 rather than being the grain nucleant acts as a grain refiner by mitigating grain growth. As the solidification progresses, the reducing liquid fraction takes up more and more particles which increase its viscosity considerably. This combined with the diffusion layer mechanism, forces the feeding to switch from inter-dendritic liquid feeding(as in conventional alloys) to mass and bulk feeding. Because of the elimination of inter-dendritic feeding, solute segregation(Cu in A201) has been brought down significantly. It was also observed that, $CuAl_2$ phase solidifying over the TiB_2 particles are more dispersed than in A201 alloy without TiB_2[33]. The reinforcement particles would act as grain refiners only with excess titanium; otherwise, the particles would switch to be reinforcing instead of grain refining. J Forde has studied the effect of composition of free titanium in A205 alloy to prove that free titanium effectively helps with grain refining[23]. The grain refinement brought by free Ti could be attributed to the peritectic reaction that occurs at 0.15wt% Ti forming Al_3Ti(Figure 2.10). Davis et al[34] has reported convincing evidence that, at hyperperitectic levels of free Ti, Al_3Ti acts as grain nucleant rather than TiB_2. J Forde's work on A205 is in agreement with the conclusion that Al_3Ti acts as the grain nucleant rather than TiB_2[23]. Logically, the grain refining action brought by TiB_2 as a diffusion barrier is effective only when the particles are pushed to the boundary.

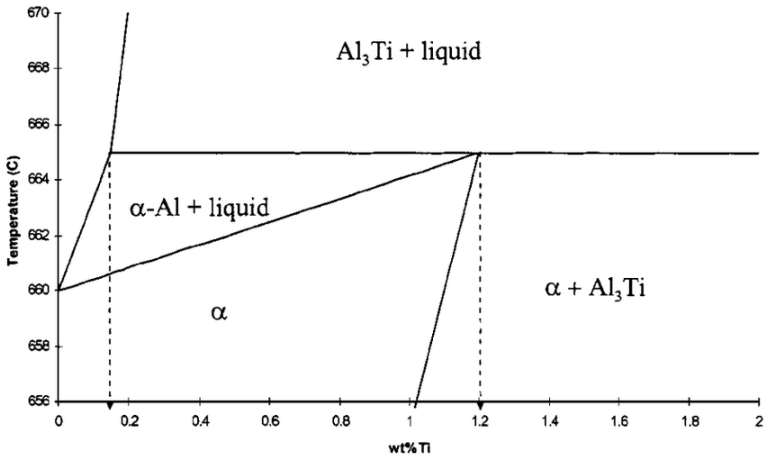

Figure 2.10. *Al-Ti phase diagram.*

One major issue with salt melt route is agglomeration of particles which could have a harmful effect on the mechanical properties of the alloy. To improve the distribution of the particles, methods involving agitation of the melt such as ultrasonic vibration of the melt during casting have been proposed[35]. The reinforcement particles when used to strengthen heat-treatable Al alloys could affect the precipitation kinetics during aging of the matrix. Due to plastic deformation around the particles due to factors like mismatch in coefficient of thermal expansion(CTE) between the matrix and TiB_2[36], there is a significant increase in dislocation density around the particles. When there are strengthening precipitates precipitating on dislocations, this inhomogeneous distribution of dislocation densities could result in inhomogeneous precipitate distribution which could affect the mechanical properties of the composite.

2.5.2 Casting defects in Aluminium/TiB_2 MMCs

One major issue with cast Al/TiB_2 composites is preventing casting defects. Butler pointed out the difficulties involved in successful removal of KF-AlF_3 (cryolite) flux layer in cast Al/TiB_2 composites. These flux inclusions could further react with other alloying element, especially Mg, forming K-rich and Mg-rich oxides. Butler's work on TiB_2 reinforced A201 casting has suggested that the salt-melt route involving formation K-rich and Mg-rich oxides negatively affects the ductility and ultimate tensile strength of the alloy[33]. This implies the reason to have a good control over processing parameters. Oxides and other non-metallic inclusions have been a major problem in aluminium castings. Ellingham diagram in figure 2.11 shows that aluminium and magnesium have a higher tendency to oxidize. Care has to be taken to not trap the oxides formed over the melt to be trapped within. Turbulence in the liquid melt breaks the oxide films creating new layers of oxides. In the turbulent liquid, the oxide tends to fold, usually trapping bubbles or liquid flux and get entrained in the alloy as it solidifies. The oxide films can be as thin as 20 nm making them hard to be characterized[37]. Ghomy et al has suggested a link between particle clustering and oxide entrapment, as TiB_2 particles tend to stick to the oxides[14]. When pore or oxides are present with clustered particles, the negative effect could be amplified. Porosities and non-metallic inclusions as a result of bad processing can be extremely harmful as they could easily act as crack initiators, especially when present close to the surface and drastically bring down the fatigue life[23]. In conventional cast aluminium alloys, upto 50% reduction in fatigue life has been noticed with presence of just 1 vol% of porosity[38]. Hot isostatic pressing(HIPing) has always been a good choice to eliminate porosities in cast systems. In A201, Butler's conclusive results show that HIPing helps only with closing porosities that are not connected

to the surface. Butler has showed using double ceramic foam filters(30 ppi) to prevent inclusion entrapment thereby increasing tensile strength and ductility and reducing scatter in the properties[33].

J Forde has suggested the elimination of shrinkage porosities that were present in A201 with A205 development[23]. But cryolite-type defects from processing have been predominantly detrimental in A205 as well.

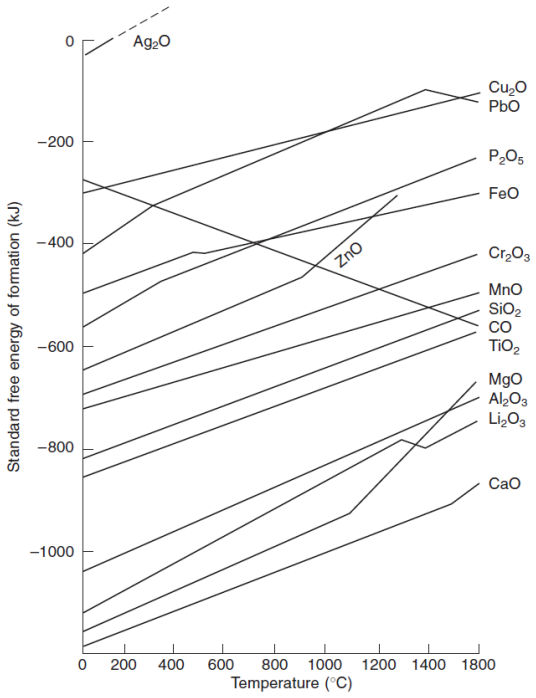

Figure 2.11. *Ellingham diagram for various metallic elements*.[37]

2.5.3 Precipitation heat-treatment in Aluminium/TiB_2 alloys

J Geng et al suggests that the in-situ TiB_2 significantly accelerates the aging process in an Al-Cu-Mg alloy with a smaller Cu:Mg ratio where S' precipitates determines the strengthening effect[39]. This is in close agreement with other studies on accelerated aging with presence of TiB_2[40-43]. In contrast, Butler has suggested that, in A201, no accelerated age hardening was observed at 170ºC with the presence of TiB_2[23]. J Forde's work also did not report any accelerated aging in A205 due to TiB_2. In A205, as with most aging treatments, an increased peak strength has been reported with reduced aging temperatures and increased aging times.

2.5.4 Mechanical properties of Aluminium/TiB_2 alloys

The addition of reinforced particles generally result in increment of yield strength and tensile strength while compensating on ductility[44,45]. The same has been observed in A201 alloy by Butler et al as well[33]. It has been frequently observed that, the strengthening effect brought by reinforcing particles is more profound in low to mid strength aluminium alloys, and not much or sometimes have a negative effect in high strength alloys. This difference in strengthening could be explained by local strains developed around the particles and fracture strength of the particle relative to the yield strength of the matrix[46]. Kapoor et al in agreement with several others suggest that, in heat-treatable aluminium alloys, precipitation by aging plays a bigger role in deciding the mechanical properties than the reinforcing particles[47].

In particle reinforced MMCs, the reinforcing particles take up the load acting on the matrix. Chawla et al has investigated the effect of reinforcement particles on the crack growth mechanisms and mechanical behavior in particle reinforced MMCs[41]. When the stress applied gets closer to the theoretical yield strength of the matrix, the particles begin to carry the load preventing the composite from yielding. The load has to be increased further for the matrix to experience its theoretical yielding stress after which work hardening of the matrix increases stress around the particles. With increasing stress, the particles begin to break or debond from the matrix creating a void. A propagating crack would consider the voids as an effective path to progress. If the particles were trying to reinforce an alloy with an inherently high yield strength(higher than the fracture strength of particles), the particles would already start breaking when the matrix begins to yield[46].

Fatigue property is a critical material property that has to be well-investigated when it comes to aero-engine components. Fatigue fractures happen through two main stages which are crack initiation and propagation. Chawla in his work, discusses how reinforcement particles can potentially nucleate fatigue cracks[41]. In conventional high cycle fatigue tests, the stresses the material will be subjected to are too low and strains operate in the elastic range where Hooke's can be applied. The crack propagation is usually well-split into three regions:

- Region I involves crack front advancement through the weakest path. In this region, the stresses are not too high to crack the particles. In this region crack growth tends to be transgranular and are not always observed to follow crystallographic planes[41]. It has been noticed in cast MMCs that, overaging, as a result of reduced strength reduces crack growth resistance in this region.

- Region II/III can be characterized by an increased crack growth rate. The crack growth rate at this region depends, to a significant extent, on the size of plastic zone created ahead of the crack tip. With the presence of reinforcement particle clusters in grain boundaries, the resistance to crack growth in this region in MMCs in negatively amplified. The fractured surface in A205 as reported by J Forde exhibited cracked TiB_2 particles and microvoid coalescence of the matrix[23].

In LCF regime, the stresses are usually huge depending on the yield strength of the material being tested. LCF tests are either stress-controlled or strain-controlled. All the results on LCF life in this thesis work are from strain-controlled testing. J Forde has investigated the fatigue properties A205 at ambient and elevated temperatures[23]. Not much of a difference was reported on crack propagation mechanisms at room and elevated temperatures. In the overaging case, the reduced LCF life has been attributed to the weaker matrix. It has been suggested that, the LCF life depends on the strength of the matrix. When the matrix is weak, the resistance to crack propagation goes down leading to a poor LCF life. Relative to A201, A205 has shown better LCF life due to the elimination of shrinkage porosities profound in A201[23]. In A205, the most predominant fatigue crack initiators were identified to be potassium-based inclusions[23]. In the overstress regions of fatigue fractographs, ductile regions with microvoid coalescence and brittle zones with broken TiB_2 particles and Al_3Ti particles were observed.

2.6 Property prediction

For over 30 years, CALPHAD(Computer CALculation of PHase Diagrams) has been used by industries to assist in alloy design. Eventually, the approach was extended to model other properties such as atomic mobilities, temperature dependent diffusion coefficients, time dependence of phase transformations, and microstructures[48]. Researchers have constantly tried to develop models that could predict the precipitation characteristics in heat-treatable aluminium alloys. Depending on the alloy chosen, the precipitates could be rod shaped, needle-shaped or plate-shaped. The shape of the precipitate significantly affects the strength calculation[49]. In theory, the precipitation process happens in three stages: nucleation, growth and coarsening. In reality, all three stages happen at the same time. Several phase field models were built to consider gradient thermodynamics and diffused interfaces to improve the quantitative prediction of precipitation characteristics[50]. ThermoCalc has developed PRISMA that could simulate the precipitation characteristics that could consider concurrent nucleation, growth, and coarsening. PRISMA accommodates the overlapping of different stages by calculating the evolution of the probability distribution of the particle number densities, termed as particle size distribution(PSD). According to the user guide, PRISMA adopts the Kampmann-Wagner numerical

method for precipitation calculations[51]. Earlier, the non-spherical precipitates being too complex to model were assumed to be spherical for the purpose of theoretical computations. Also, the dislocation-precipitate interaction becomes complicated to describe mathematically as the shape of the precipitates turn non-spherical. This fact has been huge hurdle for strength prediction. Recently several phase-field models have been built to accommodate the shape and orientation of the precipitates; most appropriate for the current work being Liu et al's model on Al-Cu-Mg alloys and Gazizov et al's model on Al-Cu-Mg-Ag alloys[24,52]. G Liu et al has suggested that, in the case of $CuAl_2$ precipitates, the aspect ratio changes from 10 to 30 as it strengthens and then decreases again towards 10 during over-aging. At the moment, PRISMA does not provide a way to accommodate the change in aspect ratio, although it could approximately deduce it from the elastic properties of the matrix and transformation strain given by the user.

2.6.1 Nucleation calculations by Prisma

For the nucleation calculations, Prisma uses the classic nucleation theory for which the nucleation rate can be mathematically expressed as:

$$J(t) = J_s \exp\left(\frac{-\tau}{t}\right) \quad \text{…Exp.2.5}$$

$$J_s = Z\beta^* N_0 \exp\left(\frac{-\Delta G^*}{kT}\right) \quad \text{…Exp.2.6}$$

where $J(t)$ and J_s are the time-dependent and steady-state nucleation rate respectively, τ is the incubation time to achieve steady state conditions and t is the time, Z is the Zeldovich factor, β^* is the rate at which atoms are attached to critical nucleus, k is Boltzmann's constant and T is absolute temperature, and ΔG^* is the Gibbs energy of formation of a critical nucleus. The factor Z accommodates for probability of precipitates bigger than critical nucleus dissolving back into the matrix.

ΔG^* can be mathematically expressed as:

$$-\Delta G^* = \frac{16\pi\sigma^3}{3\left(\frac{\Delta G_m^{\alpha\to\beta}}{V_m^{\beta}}\right)^2} \quad \text{…Exp.2.7}$$

where $\Delta G_m^{\alpha\to\beta}$ is the chemical driving force for the formation of β precipitate in α matrix and V_m^{β} is the molar volume of β precipitate.

The parameter β^* seems to depend on the critical radius r^*, diffusion coefficient and difference in mole-fraction of solute at the interface and in the matrix. The critical radius depends on molar volume of the precipitate, interfacial energy and $\Delta G_m^{\alpha\to\beta}$. The incubation time to reach steady state nucleation rate is treated as a function of β^* and Z. Introducing an elastic strain energy E_{el} would reduce the chemical driving force in Exp.2.7. therefore affecting the nucleation rate and size. Changing the shape of precipitates affects the kinetics through the elastic strain energy factor. It is to be noted that, the nuclei is always treated as a sphere for nucleation calculations and assumes the input interfacial energy for a spherical coherent nucleus. It makes sense as the dominant factor would be the interfacial energy. Figure 2.12 shows how the different parameters influence the output of nucleation calculations.

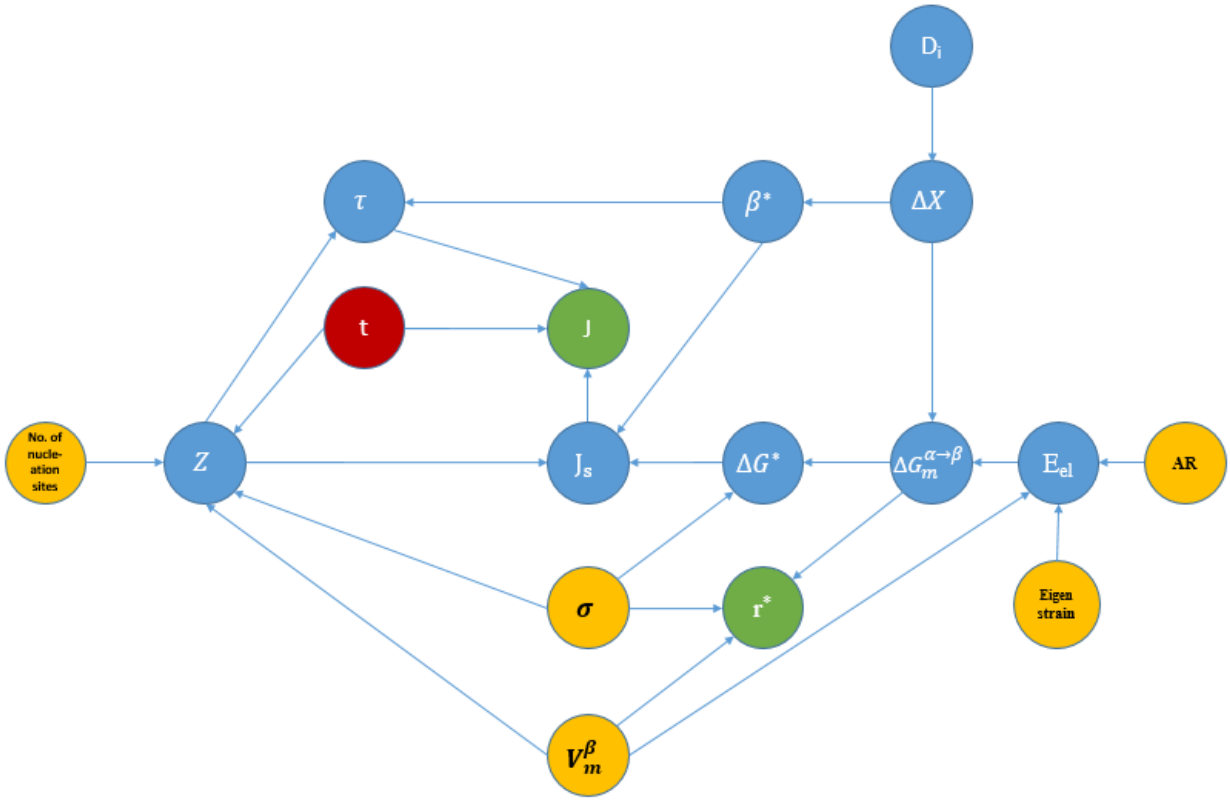

Figure 2.12. *Interplay of parameters to process critical radius r^* and nucleation rate. Blue bubble represents uncontrollable parameters; yellow bubble represents parameters input by the user; red bubble represents completely independent parameters.*

2.6.2 Growth and coarsening calculations by PRISMA

The expression used by PRISMA for defining the growth rate is:

$$v = \frac{2\sigma V_m^{\beta} K}{r}\left(\frac{1}{r^*} - \frac{1}{r}\right) \quad \text{…Exp.2.8}$$

K is a kinetic parameter influenced by the interface composition and mobility of solute. For non-spherical particles, Prisma still uses the equations for spherical particles but with a correction factor for K. The radius obtained as output would be the radius of a sphere which has the same volume as the non-spherical particle. Figure 2.13 shows how the different parameters influence the output of nucleation calculations.

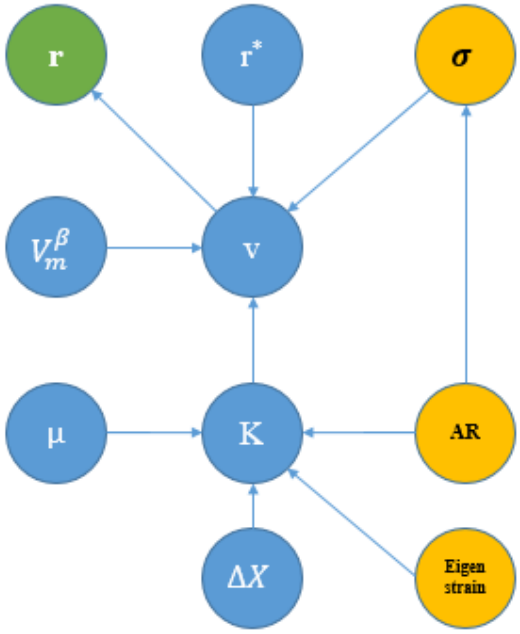

Figure 2.13. *Interplay of parameters to process radius evolution during growth and coarsening. Blue bubble represents uncontrollable parameters; yellow bubble represents parameters input by the user.*

2.6.3 Strength prediction

Strength models that predict the strengthening effect from precipitation characteristics are quite well-explored. A widely accepted equation for increment in critical resolved shear stress(CRSS) is[53]:

$$\tau_p = \xi \frac{Gb}{2\pi L_{cc}} ln \frac{\chi}{r_o} \quad \text{…Exp. 2.9}$$

where L_{cc} is the spacing between obstacts in the slip plane, G is the shear modulus, b is the magnitude of the burgers vector, r_o and χ are the inner and outer cut-off radius for dislocation line tension calculation and ξ is related to the initial dislocation character. As it could be seen from the equation, a finer and more densely distributed precipitation could strengthen more effectively. This expression is applicable only to non-shearable precipitates as it assumes Orowan interaction mechanism at work.

For shearable precipitates, the strengthening mechanisms operating could be interfacial strengthening, coherency strengthening, stacking-fault strengthening, modulus strengthening, and order strengthening. This has been accommodated by an equation of the form[24]:

$$\sigma_p = M * \left(\frac{2}{b\sqrt{\Gamma}}\right) * \left(\frac{1}{L_{cc}}\right) * \left(\frac{F}{2}\right)^{\frac{3}{2}} \quad \text{…Exp. 2.10}$$

where M is the Taylor factor, Γ is the dislocation line tension which can be approximated as $\frac{1}{2}Gb^2$, F represents the resistance of the precipitates to dislocation shearing.

Figure 2.12 shows the general trend that the strength of the alloy follows with respect to the radius of precipitates depending on the type of interaction.

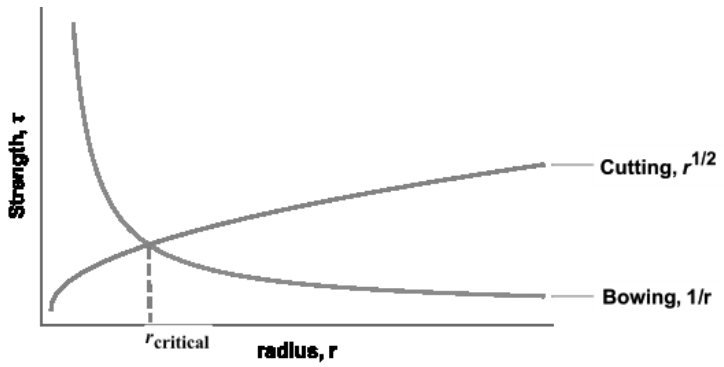

Figure 2.12. *General strengthening trend as a function of radius with respect to dislocation/precipitate interaction mechanism.*[54]

Gazizov et al has proposed a strength prediction model for Al-Cu-Mg-Ag alloys where the predominant strengthening precipitates are considered to be Ω precipitates, and modelled to accommodate its co-existence with θ' precipitates. Ω precipitates have been assumed to be shearable in all aging conditions and the precipitation strengthening effect was proposed as[24]:

$$\sigma_p = M \frac{1.211 d \gamma_i^{3/2}}{t^2} \sqrt{\frac{b f_v}{\Gamma}} \quad \text{…Exp. 2.11}$$

where f_v is the volume fraction of precipitates, d and t are the diameter and thickness of precipitates respectively, γ_i is the interfacial energy. For Ω precipitates forming during aging treatment at 200ºC and 250ºC, the interfacial energies are fitted to be 0.140 J/m^2 and 0.165 J/m^2.

Zhu et al has proposed mathematical equations to calculate the strengthening effect as function of precipitate sizes and modified them according to the shape of obstacles and the planes they are aligned in[53]. For an Al-Cu-Mg alloy in overaged condition, G Liu et al has tried to fit in the equation suggested by Zhu to predict the difference in yield strength after overaging and inherent yield strength as[52]

$$\sigma_p = \frac{H}{r} \ln \frac{0.0158\, r}{r_o} \quad \text{…Exp. 2.12}$$

where H is a constant depending on the saturated volume fraction of the precipitate and r is the dimension of the precipitates and r_o is assumed to be 0.572 nm. It has been shown to match to an appreciable accuracy with experimental values.

Chapter 3

Experimental Methods

3.1 General procedures followed

The casting process and parameters are controlled by the supplier and due to confidentiality, the exact temperatures and other parameters will not be revealed in the thesis. The material specification is dictated by AMS4471. Times and temperatures that are confidential are replaced with alphabets with appropriate subscripts.

3.1.1 Heat treatment

The T7 heat treatment of cast A205 involved step-solutionizing through four different temperatures, taking s_4 hours in total. The solutionizing heat-treatment cycle was selected to prevent incipient melting while ensuring complete dissolution of $CuAl_2$. According to the T7 heat-treatment specification, aging was carried out at 170^{o}C for a_4 hours to have a slight overaging.

3.1.2 Optical microscopy

3.1.2.1 Metallography

All specimens for metallography were prepared by procedures recommended by Struers. Table 3.1 shows the method, equipment and consumables used for sample preparation. Three different etchants as recommended by ASM handbook[2] were tried in efforts to reveal the features of interest. The best etchant that seemed to work was Keller's reagent. Both immersion and swabbing were tried and immersion etching was chosen as it worked better. The immersion time was optimized to 20 s to have an over-etched surface. Since many microstructural features were revealed just after polishing, images were captured before and after etching.

Table 3.1. Metallographic sample preparation procedure followed

Sample preparation step	**Equipment**	**Consumables**	**Parameters**
Sectioning	Secotom-50	10S15	Cutting feed: 0.35 to 0.90 mm/s
Mounting	Citopress-30	Polyfast	Struers' program
Grinding and polishing	Tegramin-30	500 grit SiC paper	Struers' program
		9 micron diamond abrasives; MD Largo disc	
		3 micron diamond abrasives; DiaMol disc	
		Colloidal silica; MDChem pad	
Etching	-	Keller's reagent (2 mL HF(48%), 3 mL HCl(conc), 5 mL HNO_3(conc), 190 mL water).	20 seconds – Immersion and rinsing in water.

Some of the cast structures were not globular and either rosette shaped or dendrite shaped. Figure 3.1 shows the typical shapes of grains after solidification and the way they are classified. The grains are named dendritic or rosette depending on how they have tried to branch out from the nucleation point during solidification. Dendritic structures are very common in castings and are primary characterized by primary and secondary arm spacings. In rosette structures there are no elongated branches as in dendrites but short protrusions in the solidified grains. The globular structure shows no solidification branches and solidified grains take simple geometric shapes close to spherical. Since there had to be a base ground to compare, planimetric method according to ASTM standard E1382 was used for grain size measurement of all specimens.

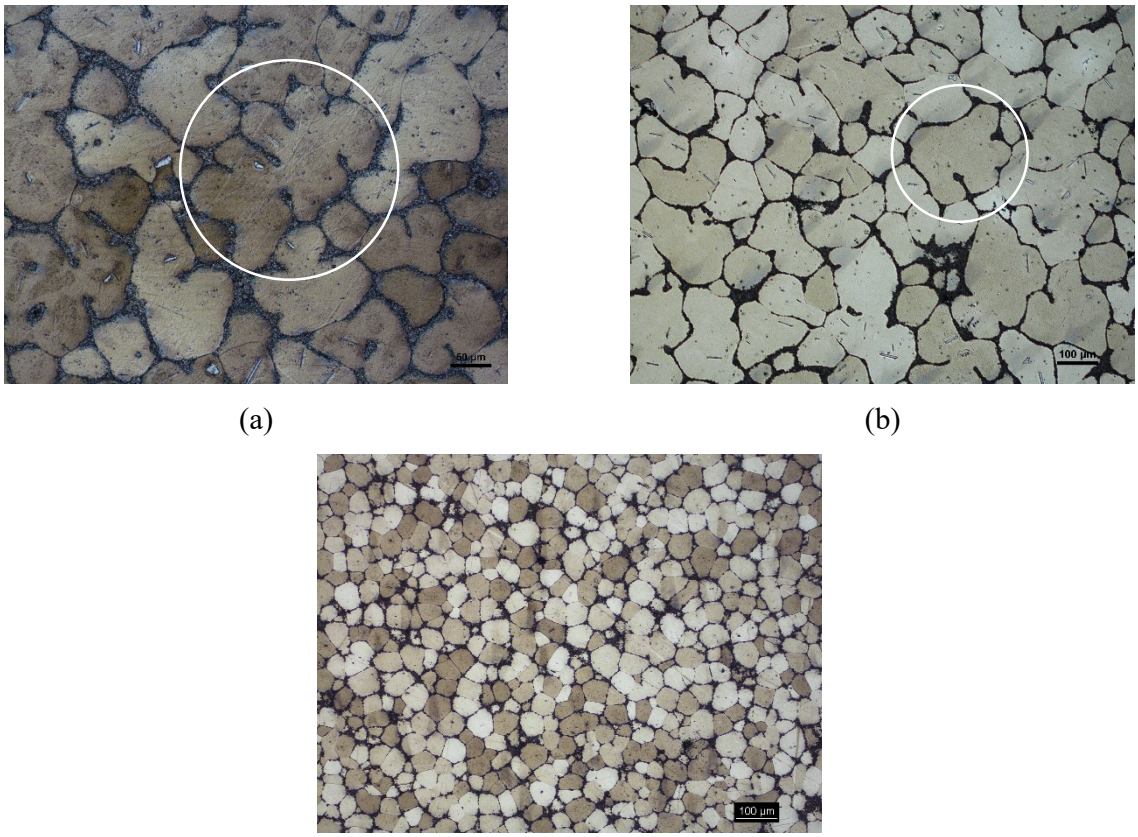

(a) (b)

(c)

Figure 3.1. *Grain morphologies in A205 – (a) Dendritic shape(circled); (b) Rosette shape(circled); (c) Globular shape*

3.1.2.2 Fractography

Fractured LCF-tested specimens were advantageously chosen and observed under VHX 6000 by Keyence – an optical stereo-microscope. Depending on the morphology of crack initiators observed, specimens were chosen for further SEM and EDS analyses to characterize the crack initiators.

3.1.3 Scanning Electron Microscopy and Energy Dispersive Spectroscopy(EDS)

Specimens were not mounted for fractography. SEM with EDS analysis was performed with Hitachi S3700N at Swecast(RISE), Jönköping. For imaging $CuAl_2$ precipitates, a more sophisticated SEM with a Field Emission Gun(FEG) was used for a better resolution. The samples selected for precipitate imaging were mounted and polished in the same way as for optical microscopy.

3.1.4 Hardness testing

The same specimens used for optical microscopy were used for hardness testing. Microvicker's was chosen as hardness testing method. All hardness values were measured according to ASTM E384. Hardness tester was calibrated for the selected load every day before measurements. The load and dwell time for all the tests were 300 g and 10 s respectively. All the hardness values in the hardness evolution investigation were normalized by dividing the data by the maximum hardness.

3.1.5 Mechanical Testing

All mechanical tests were outsourced and completed before the thesis work started. The fractured specimens and results from the tests were readily available for investigation.

3.1.5.1 Tensile testing

All room temperature tensile tests were performed in accordance with ASTM E8M-11 and all elevated temperature tensile tests were done in accordance with ASTM E21-09. The test environment was air. The strain rate was controlled at 0.5% per minute up to yield stress and then stroke controlled at 0.05 mm/mm(gauge length)/minute. All the quantitative tensile properties investigated were normalized by dividing the data by the maximum value.

3.1.5.2 LCF testing

All LCF tests were strain-controlled and done in accordance with ASTM E606-12. The test environment was air. A triangular stress waveform with an R-ratio of 0 at a frequency of 0.5 Hz was used.

3.2 Experiment specific procedures

3.2.1 Heat treatment

As-cast A205 bar was procured from the supplier. Having a grain size number of 10, it had a hardness of 78 HV. A Heraeus high temperature furnace was used for solutionizing and Heraeus-Function Line oven was used for aging. Both the furnaces were calibrated to work correctly. For the aging trials, the as-cast bar was cut into slices approximately 5 mm thick. Solution treatment was done to specification and aged at two different temperatures(205ºC and 170ºC). Specimens at different solutionizing times

very investigated - s_o(as-cast structure) , s_1, s_2, s_3 and s_4(where s_o=0 hours; $s_1 < s_2 < s_3 < s_4$). Specimens picked out of the furnace were quenched in water. During aging, samples were picked out at aging times as shown in table 3.2. Aging times were selected based on J Forde's work on A205[23].

Table 3.2. *Times at which aging specimens were picked out of furnace for investigation*

($a_1 < a_2 < a_3 < a_4$; $b_1 < b_2 < b_3 < b_4$; $b_4 < a_1$)

	Specimen I	**Specimen II**	**Specimen III**	**Specimen IV**
Aging time at 170°C	a_1	a_2	a_3	a_4
Aging time at 205°C	b_1	b_2	b_3	b_4

The supplier recommended a relaxation of 6 hours after solutionizing. Two batches of specimens were solutionized and aged – one with relaxation after solutionizing and the other without relaxation. This was done to find the effect of relaxation on hardness of the alloy during aging. A small piece of the sample sizing about 1 cm x 1 cm was sectioned for metallography and hardness testing.

3.2.2 Prolonged thermal exposure

T7 heat treated treated A205 was subjected to prolonged thermal exposures at 150°C and 200°C for 100 and 1000 hours. The exposure was performed on fully machined specimens by Westmoreland Mechanical Testing & Research(US)[55]. The starting material had a grain size number of 3 with a hardness of 160 HV. They were tensile tested at different testing temperatures(Room temperature, 200°C and 250°C). One set of specimens with elevated temperature exposures were tested at 100°C and 150°C additionally. The aim of this experiment was to find out how the mechanical response was at elevated temperatures which are close to and higher that the temperatures at which the alloy will be operating.

3.2.3 LCF properties

There were three batches of LCF tested specimens investigated and will be called Batch A, Batch B and Batch C in the thesis work. The three batches were solutionized and aged to different times. Table 3.3 shows the microstructures and grain sizes of the three batches of specimens – A, B and C. The difference in grain size was possibly achieved by controlling the mould temperature, although there was no information available on processing parameters. The differences in microstructure and aging

times resulted in different hardness within each batch. Figure 3.2 shows the hardness of specimens from different batches solutionized and aged to different times. The points are color-coded depending on the aging time. By treating the batches independently, effect of hardness on fatigue life was investigated.

Batch C specimens were additionally tested at three different temperatures – 20ºC, 100ºC and 150ºC to find if the fatigue properties of the completely T7 heat-treated material changed at elevated temperatures positively or negatively. The test results on the fatigue life can be found in GKN Aerospace's internal documents[56-58].

The whole test campaign was built with two aims:

1. Investigating the effect of testing temperature on fatigue life
2. Investigating the effect of aging time at 170ºC on fatigue life

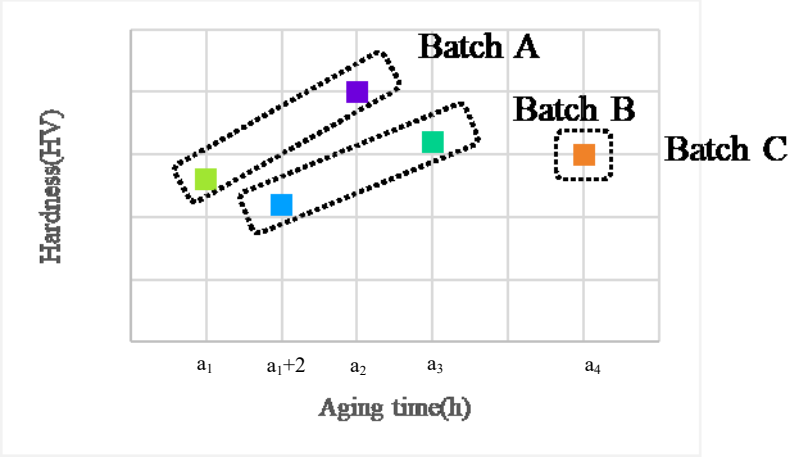

Figure 3.2. *Hardness of Batches – A, B and C aged to different times.[Y-axis was removed for confidentiality purposes]*

Table 3.3. *Microstructure, Grain size and Heat-treatment conditions of Batches-A,B and C.*

Batch	**Microstructure**	**Grain size number**	**Heat treatment condition**
A		6.5	Solutionized; Aged to a_1 h and a_2 h
B	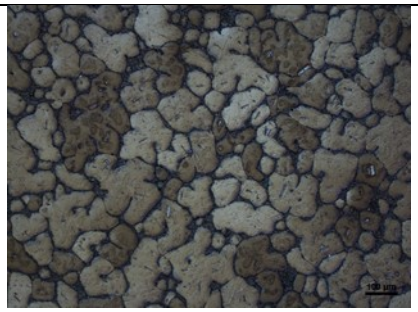	4	Solutionized; Aged to a_1+2 h and a_3 h
C	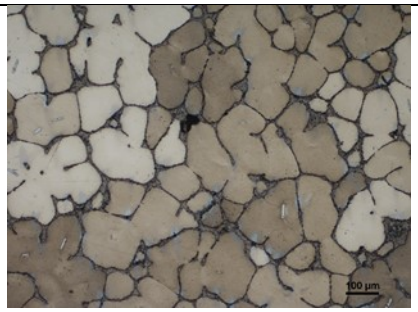	2.5	Solutionized; Aged to a_4 h(complete T7 treatment)

3.2.4 Property prediction

The main requirements to use a strength model to predict the aging effect were diameter, thickness and volume fraction of precipitates. The precipitation parameters were planned to be derived from the precipitation simulation tool ThermoCalc – Prisma. For precipitation simulation, the initial plan was to use the precipitate sizes experimentally obtained to calibrate Prisma parameters. But unfortunately, the resolution of SEM did not suffice for measuring the dimension of precipitates. So, five well-resolved particles were chosen from the images and this was considered for mean-dimension calculations to calibrate the model. This eliminates the possibility of using any strength models. For simulation with Prisma, databases TCAL6 and MOBAL5 were uses.

The property prediction were required to serve two objectives:

1. Finding the magnitude of reduction in yield strength after prolonged thermal exposures at elevated temperatures up to 200ºC

2. Aging behavior optimization to choose right aging parameters to shorten aging times

For the first objective a more simplistic tool using a LM-Parameter is proposed to fit the experimental results. In other words, it was to reverse engineer the decreasing trend of yield strength with exposure times from experimental strength values.

For the second objective, a tool from literature was found and then validated with the results experimentally available.

Chapter 4

Results and Discussion

4.1 Heat treatment

4.1.1 Microstructure of starting material

Figure 4.1 shows the microstructure of starting material in the as-cast state. Etching with Keller's reagent revealed a phase in the grain boundaries(pinkish in colour) and this could be the eutectic $CuAl_2$ formed during solidification[1]. The Al_3Ti particles were long and each particle seemed to have nucleated several grains. The morphology of Al_3Ti particles are probably dictated by the chemistry of the alloy and the manufacturing technique[59]. With a grain size number of 10, it had a hardness of 78 HV.

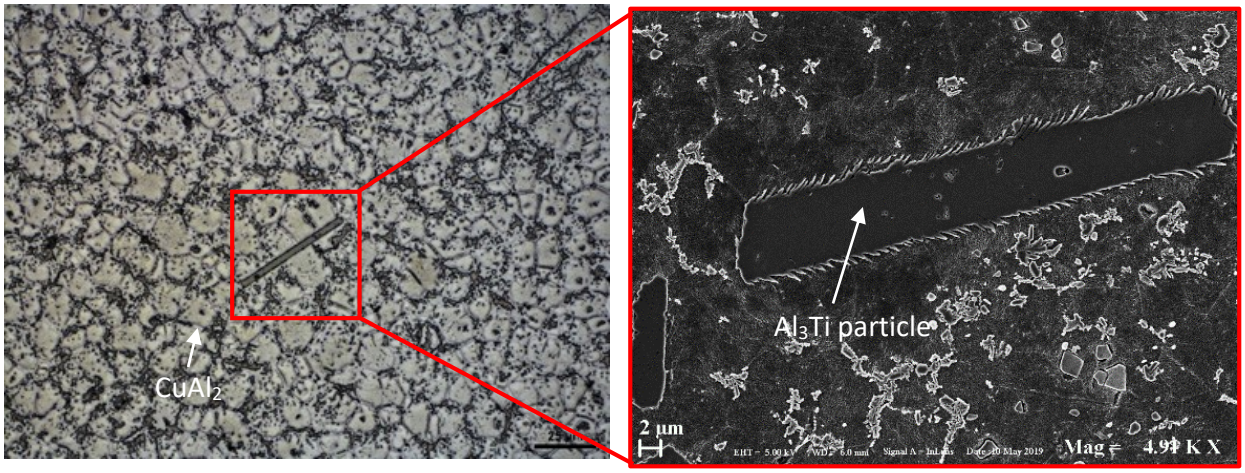

(a) (b)

Figure 4.1. (a) *Microstructure of as-cast A205 with eutectic-$CuAl_2$ phase at the grain boundaries formed during solidification(Etchant:Keller's) (b) Magnified SEM image of an Al_3Ti particle found in the as-cast structure.*

4.1.2 Solution treatment

Figure 4.2 shows the change in hardness over solutionizing time. There was a significant hardening effect in the first s_1 hours after which, the hardness reached a plateau. The increase in hardness can be attributed to the hardening effect of Cu that is dissolving into the matrix. The reason behind saturation in hardness is not conclusive at the moment, but could be due to complete dissolution of $CuAl_2$. To second the statement the microstructure after solutionizing, as shown in figure 4.3b showed no signs of $CuAl_2$, and only TiB_2 particles at the grain boundaries as shown by the SEM image in figure 4.3c. Further EDS-analyses in the grains at different solutionizing stages are required to prove the hypothesis.

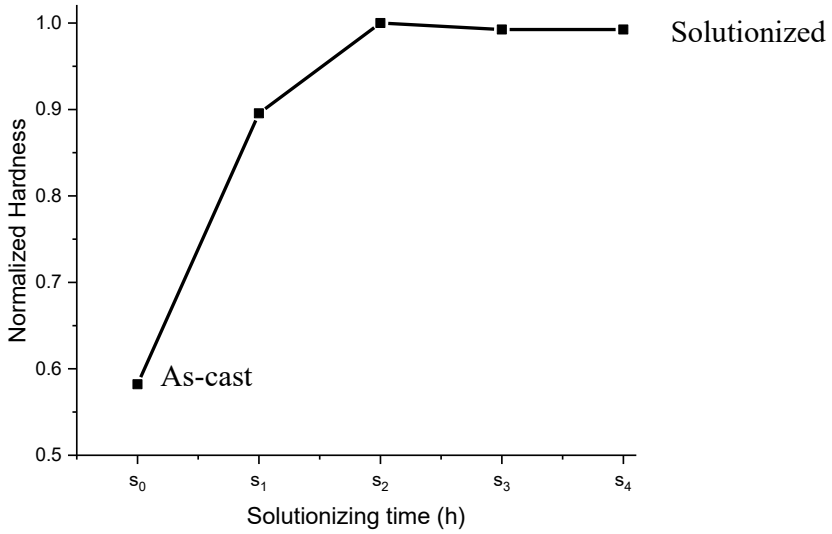

Figure 4.2. *Hardness evolution during solution treatment from the as-cast state to solutionized state after s_4 hours*

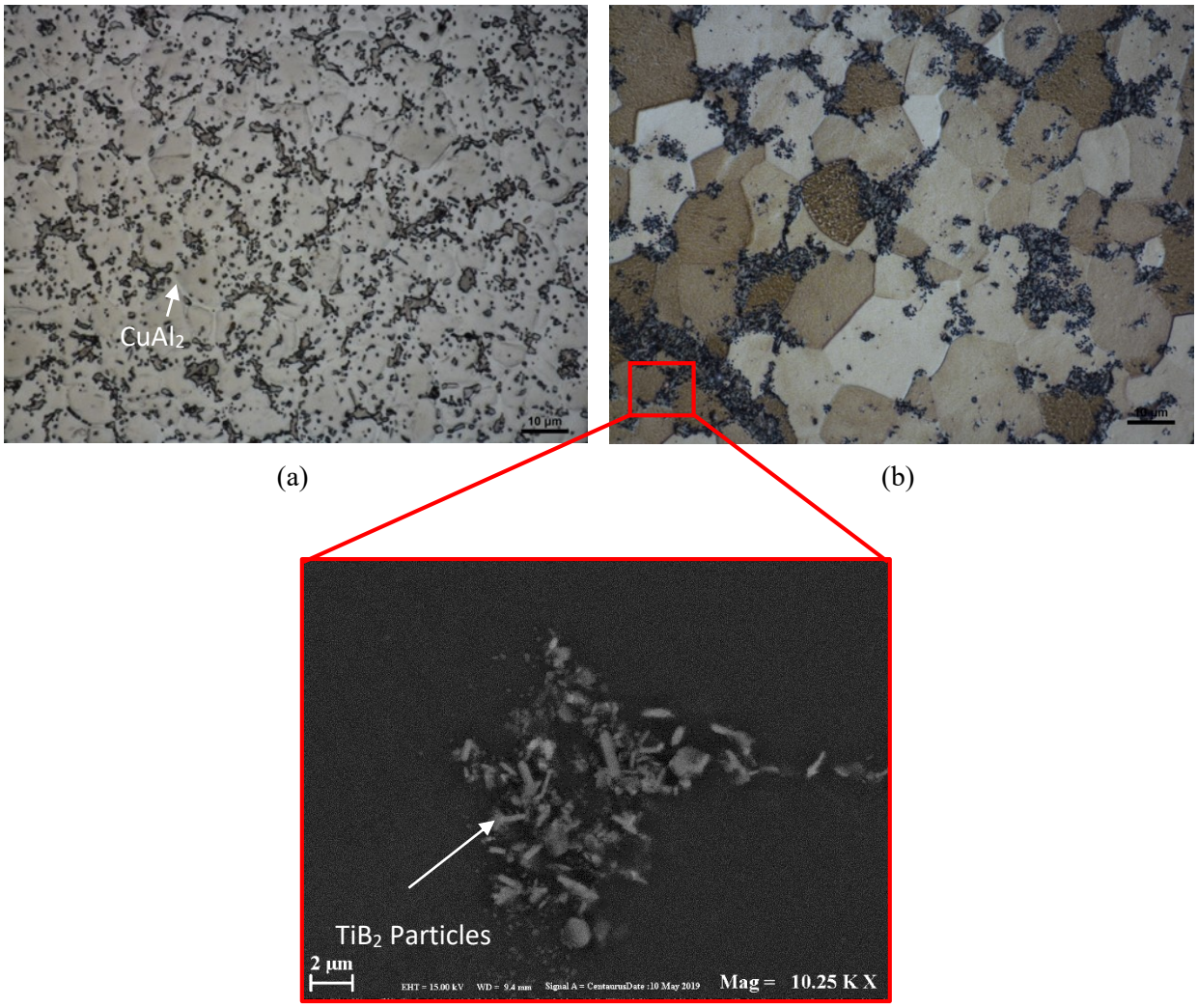

Figure 4.3. *Microstructures – (a) Microstructure(1000x) of as-cast A205 with $CuAl_2$ at grain boundaries before solution treatment; (b) Microstructure(1000x) of solution treated A205 with no signs of $CuAl_2$ at grain boundaries; (c) SEM image of TiB_2 particles in the grain boundaries of solution treated A205.*

4.1.3 Aging

Figure 4.4 shows the hardness evolution from aging at 170ºC and 205ºC, with and without relaxation. Relaxation of 6 hours after solution treatment improved the hardness slightly irrespective of the aging temperatures chosen. While the aging behavior did not switch to overaging regime even after a_4 hours of aging at 170ºC, A205 started overaging just after b_1 hours of aging at 205ºC. Quantitatively, b_1 is about 15 times lesser than a_4. Assuming that A205 has reached a point close to peak hardness at 170ºC after a_4 hours, the time required to reach peak hardness can be brought down from a_4 hours(or more) to b_1 hours by increasing the aging temperature from 170ºC to 205ºC; although, increasing the aging temperature brings down the peak hardness attainable. The accelerated aging behavior at 205ºC can be due to the accelerated coarsening of $CuAl_2$ precipitates[22]. Increased aging temperature can result in coarser θ' precipitates with increased distance between precipitates, or in other words, brings the number density of reinforcing precipitates down. But on the other hand, the precipitation and growth kinetics of θ' and Ω have been found to be different[20]. Theoretically, the number density of Ω precipitates depend on the Ag-Mg co-clusters and therefore the effect of aging temperature on nucleation and growth of Ω precipitates should be different. To investigate the effect, advanced characterization techniques with a high resolution such as TEM that can resolve the fine $CuAl_2$ precipitates with thicknesses less than 5 nm are required[22]. With optical microscopy, no noticeable changes in microstructure were observed. Regardless, the difference in hardness from increasing the aging temperature was not significantly huge.

As a characteristic of 2xx.0 cast alloys, A205 also showed a reduction in grain contrast for the same etching conditions with increased aging times[2], as seen in figure 4.5. This can be a sign of precipitation growth and coarsening.

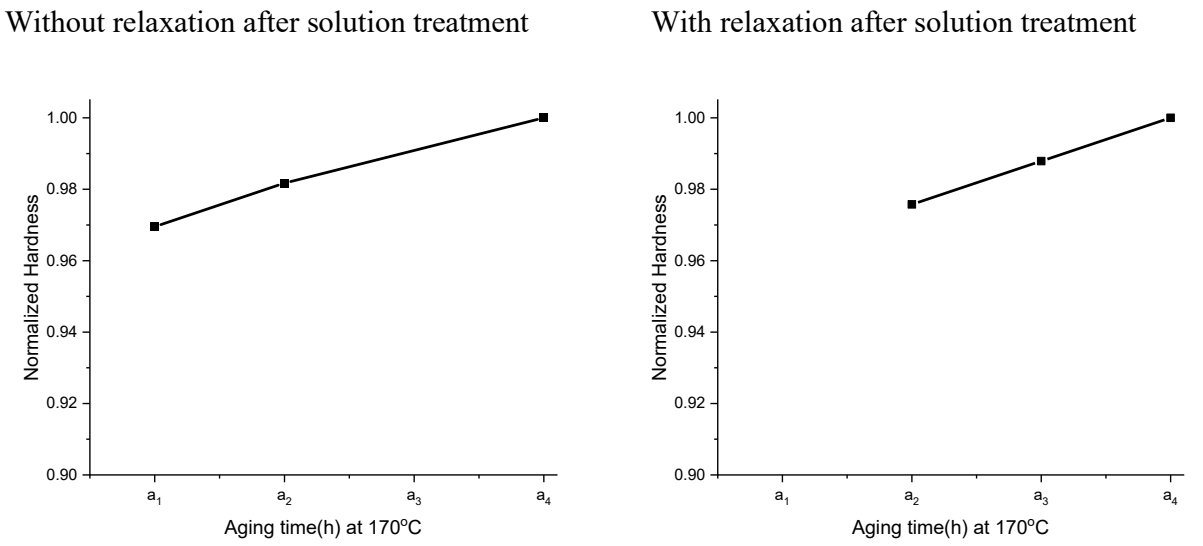

(a)

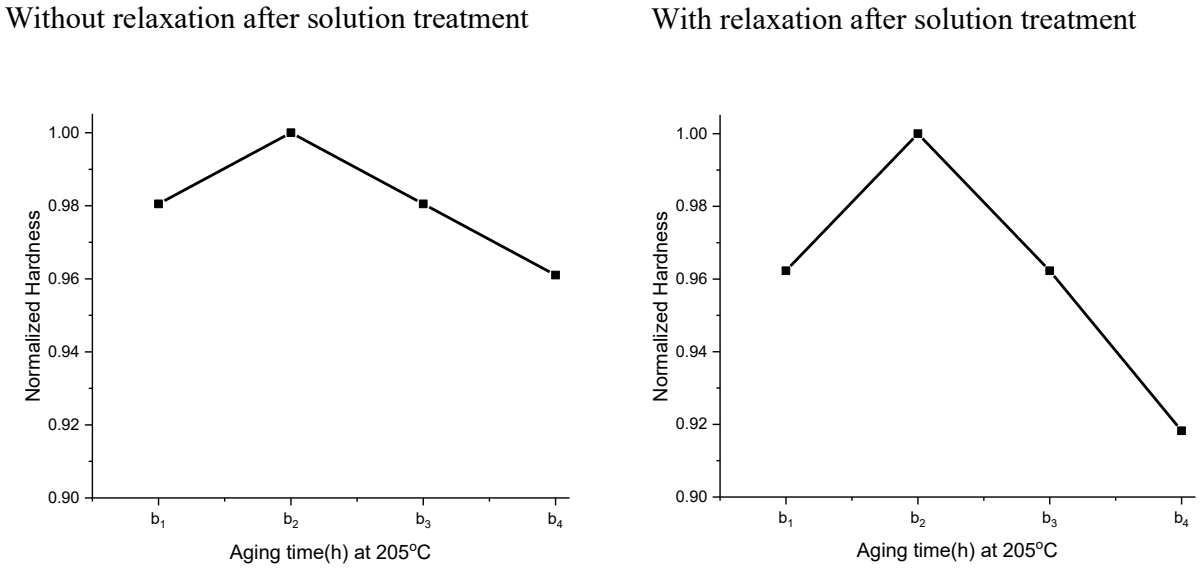

(b)

Figure 4.4. *Hardness evolution from aging with(solid line) and without relaxation(dotted line) after solution treatment at (a) 170°C – showing a rising trend even after a_4 hours (b) 205°C – showing a peak hardness at b_1 hours and then switching to an overaging regime.*

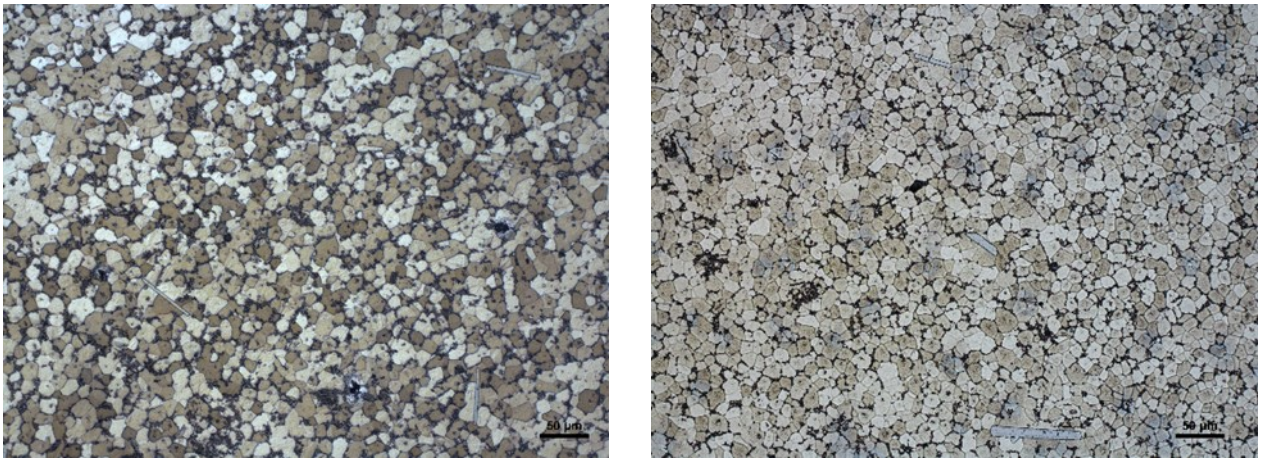

(a) (b)

Figure 4.5. *Differing grain contrast in microstructures (a) before and (b) after aging.*

4.2 Tensile properties of T7 heat-treated A205

4.2.1 Microstructure of starting material

Figure 4.6 shows a microstructure of T7-heat treated A205 which was used for this experiment. Many grains have taken a rosette structure instead of a globular structure which is a characteristic of A205[23]. The microstructure showed a variety of Al_3Ti morphologies as shown in figure 4.7. Sometimes, the Al_3Ti particles took a really bulky structure and Section 4.2.5 discusses how these abnormally bulky particles has catalyzed crack propagation.

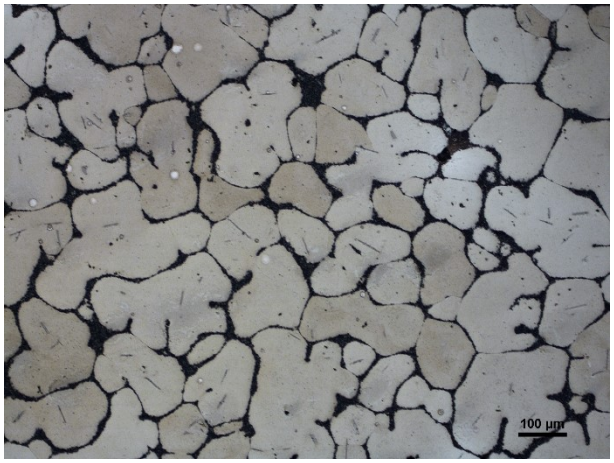

Figure 4.6. *Microstructure of T7 heat treated A205 (Magnification: 100x)*.

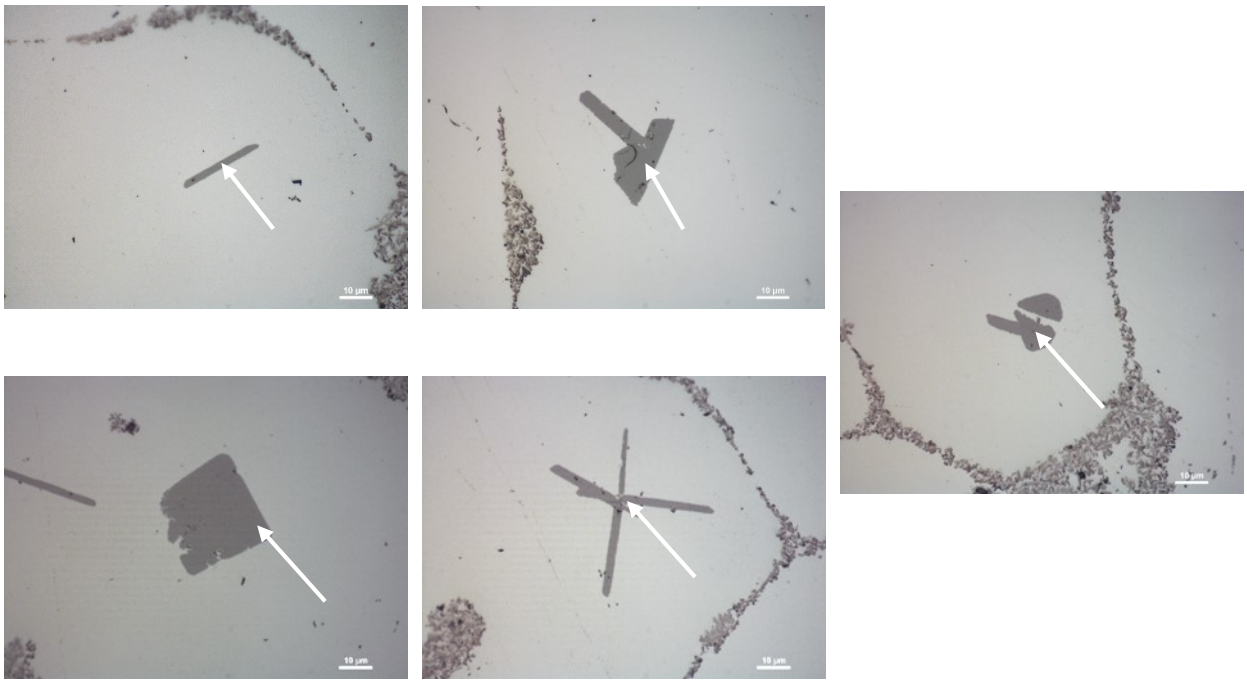

Figure 4.7. *Different Al_3Ti particle morphologies(indicated by white arrows) as observed under an optical microscope in T7 treated A205 (Magnification: 1000x)*

4.2.2 Effect of prolonged thermal exposure

4.2.2.1 Thermal exposure at 150°C

Figure 4.8 shows the change in tensile properties as result of prolonged thermal exposure at 150°C. In 1000 hours, both the ultimate tensile strength(UTS) and the yield strength(YS) dropped. The elongation did not change significantly over exposure time. The decrease in yield strength and ultimate tensile strength can be attributed to coarsening of $CuAl_2$ precipitates during thermal exposure. Coarsening of $CuAl_2$ precipitates, logically accompanies a reduction in their number density leading to reduced obstacles for dislocation motion. FEG-SEM analysis qualitatively confirms the coarsening of $CuAl_2$ precipitates as a result of thermal exposure(Figure 4.9). The $CuAl_2$ precipitates seemed to be arranged orthogonally as they precipitate in specific family of planes. Depending on the matrix planes in which they are precipitated, the precipitates could be classified as θ'($\{100\}_\alpha$ planes) or Ω($\{111\}_\alpha$ planes)[20]. Since the orientation of planes is unknown it is not possible to comment if they are θ' or Ω precipitates[16,18,21,24]. It is highly possible that they co-exist in the matrix[22].

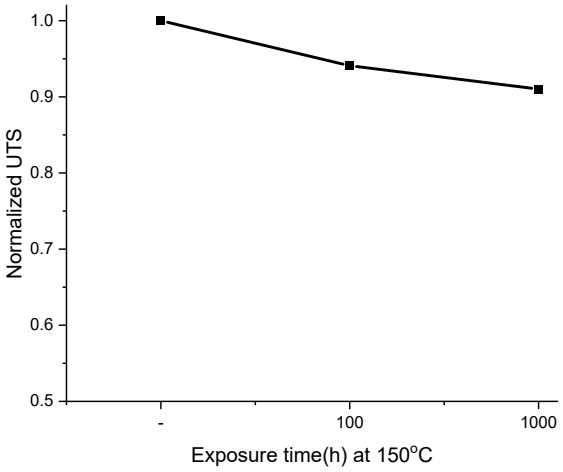

(a)

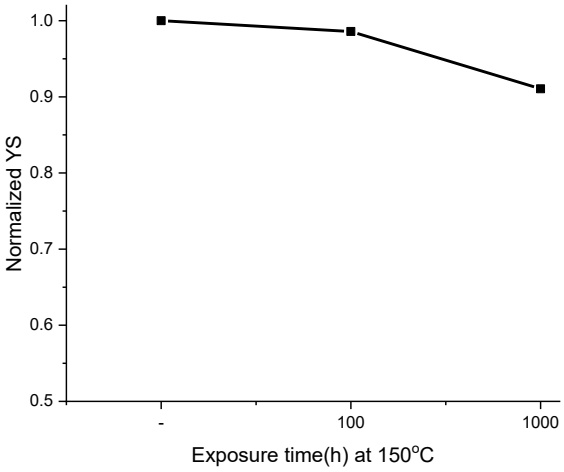

(b)

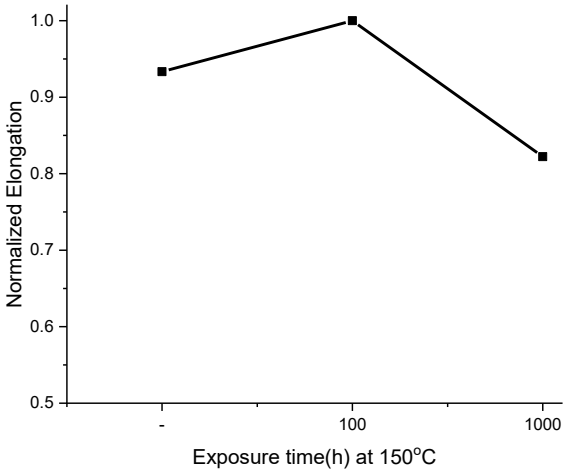

(c)

Figure 4.8. *Effect of thermal exposure at 150°C on tensile properties((a) UTS (b) YS and (c)elongation) of T7 heat treated A205.*

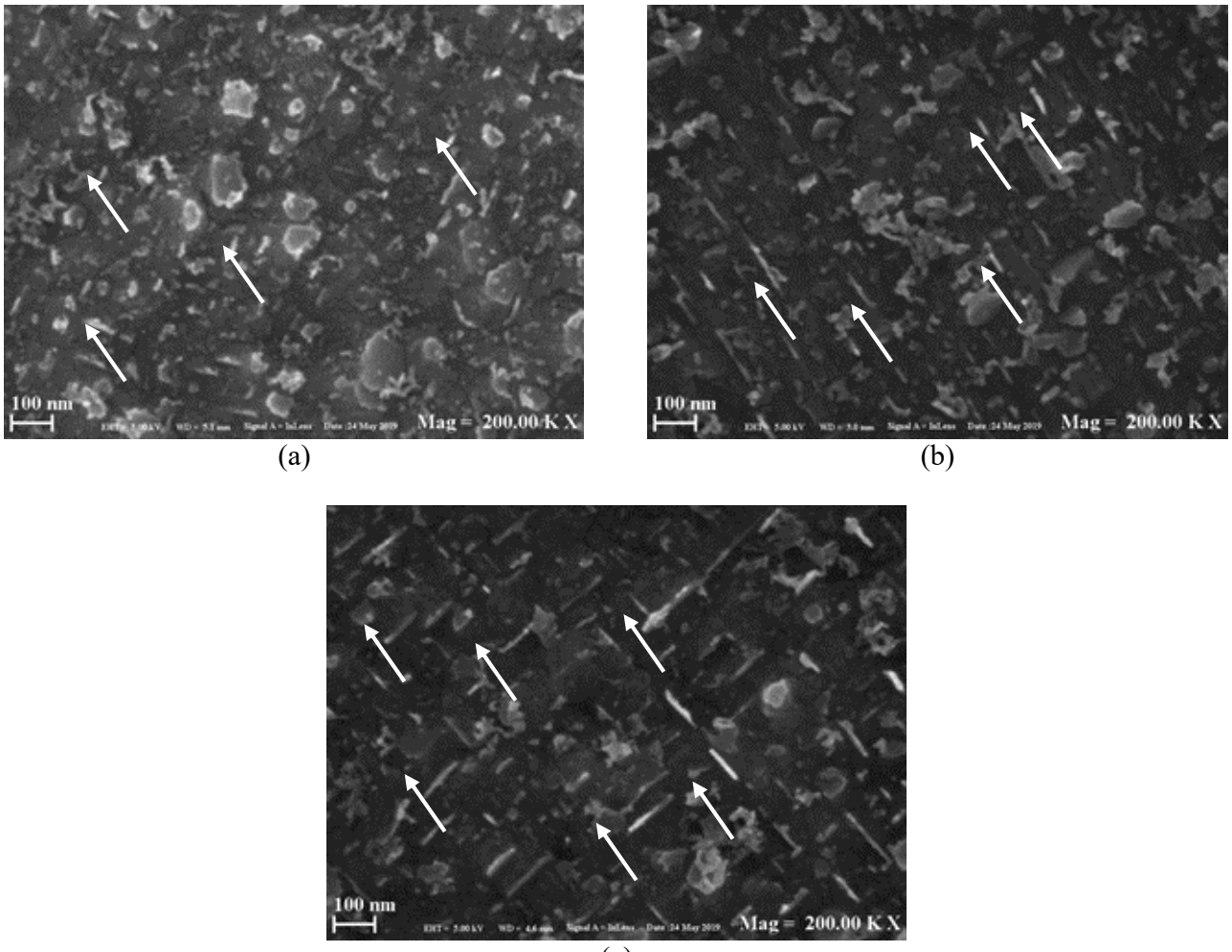

(a) (b)

(c)

Figure 4.9. *$CuAl_2$ precipitates(indicated by white arrows) under a FEG-SEM after T7 heat treatment(a), after 100 hours(b) and 1000 hours(c) of exposure at 150°C.*

4.2.2.1.1 Fractography

Both unexposed and exposed specimens at 150°C showed mixed regions of intergranular crack propagation and microvoid coalescence, as shown in figure 4.10. It is possible that, TiB_2 particles present in the grain boundaries have helped propagate the crack resulting in intergranular crack propagation zones. This fact reinforces the reason to avoid agglomeration of TiB_2 particles which has been constantly proved to be detrimental to the resultant mechanical properties[33]. The fractographs show no conclusive proof as to what nucleated the microvoids. It can be speculated to be due to the individual or combined effect of TiB_2 particles and $CuAl_2$ precipitates.

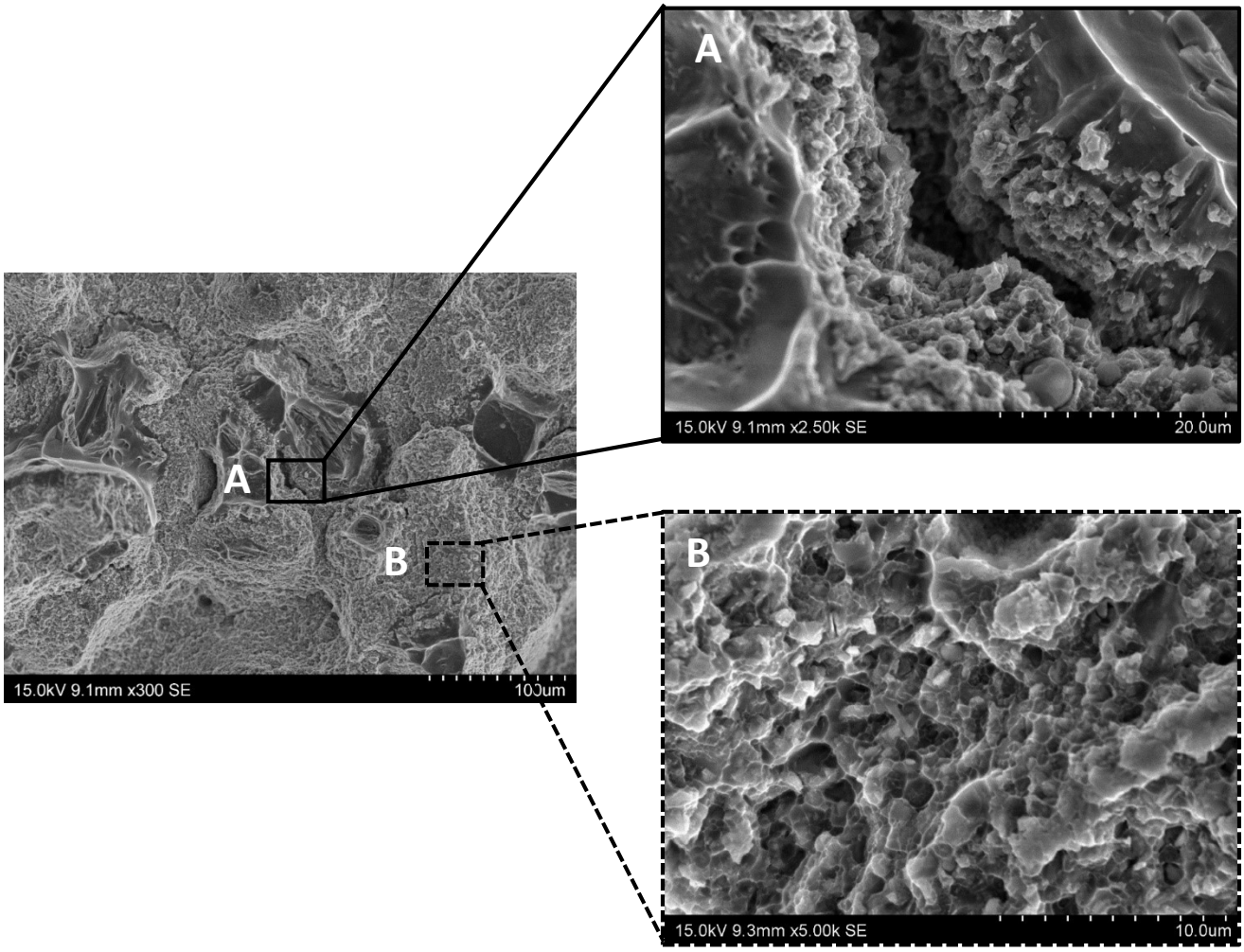

Figure 4.10. *Fractography – T7 heat treated A205 irrespective of thermal exposure times at 150°C. Region A – Inter-granular cracking as the crack propagates through grain boundaries; Region B – Microvoid coalescence due to voids nucleated by brittle particles in the matrix.*

4.2.2.2 Thermal exposure at 200°C

Figure 4.11 shows the change in tensile properties as result of prolonged thermal exposure at 200°C. Relative to exposing at 150°C, the decrease in ultimate tensile strength and yield strength was more significant. The elongation increased significantly over 1000 hours of exposure. The reason behind the changes can be attributed to the same reason of precipitate coarsening as for exposure at 150°C. The reduction in number density presents lesser obstacles to dislocations causing the drop in ultimate tensile strength and yield strength. It is interesting to note that there is an increasing trend in the work hardening effect over exposure time, marked by the difference in ultimate tensile strength and yield strength. The dislocation density was probably not affected significantly by prolonged thermal exposure, leading to a noticeable increase in work hardening effect even after phenomenal coarsening of precipitates. FEG-SEM analysis qualitatively confirms the coarsening of $CuAl_2$ precipitates as a result of thermal exposure(Figure 4.12).

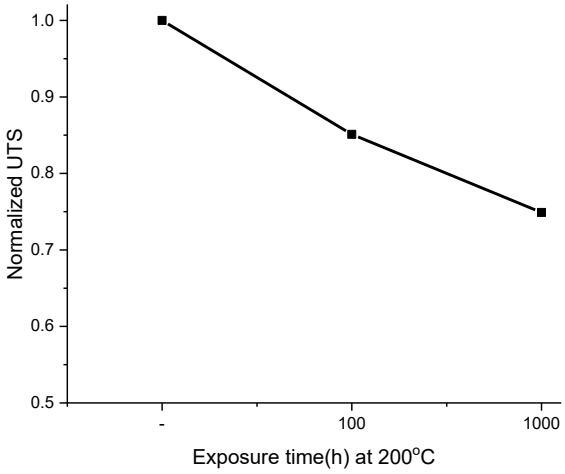

(a)

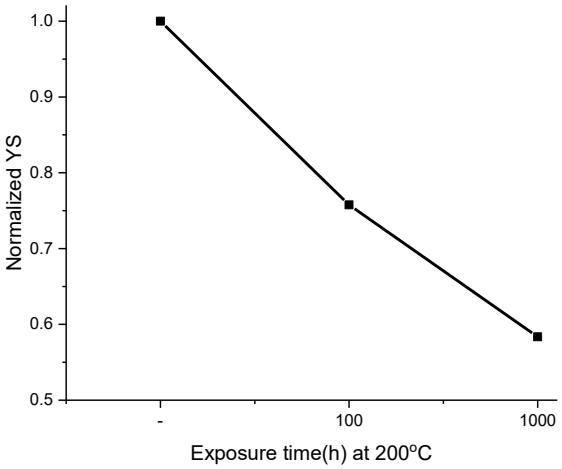

(b)

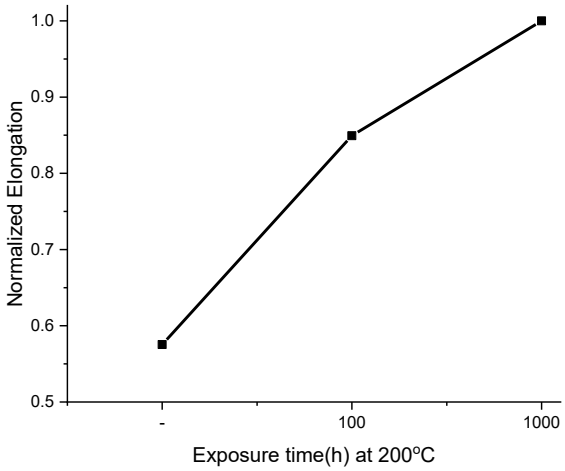

(c)

Figure 4.11. *Effect of thermal exposure at 200°C on tensile properties((a) UTS (b) YS and (c)elongation) of T7 heat treated A205.*

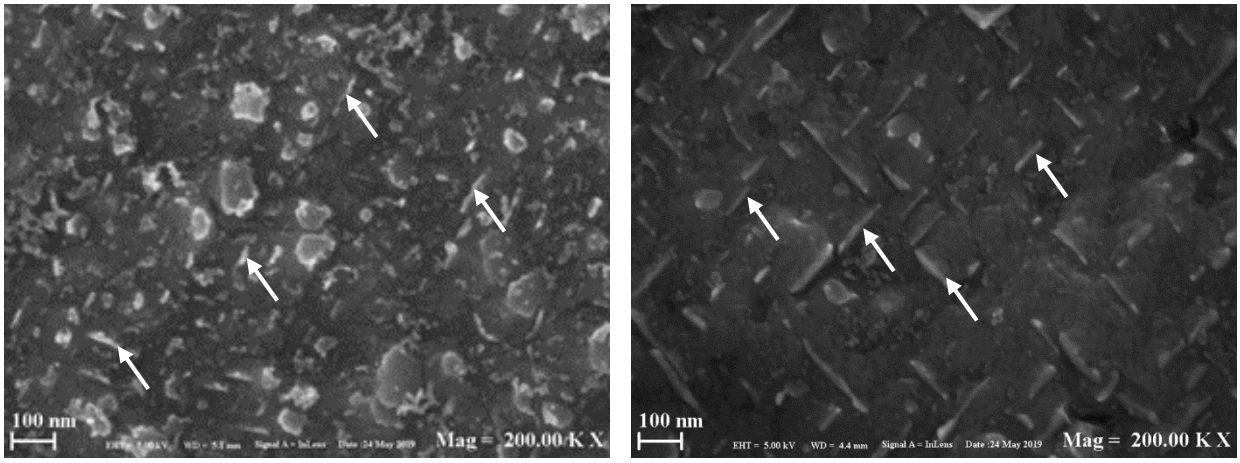

(a) (b)

Figure 4.12. *$CuAl_2$ precipitates(white plates) under a FEG-SEM after T7 heat treatment(a) and after 1000 hours(b) of exposure at 200ºC.*

4.2.2.2.1 Fractography

The crack propagation mechanism did not change from prolonged thermal exposure at 200ºC. Fractography showed signs of extensive plastic deformation in the form of longer tear ridges and bigger dimples in the microvoid coalescence zone as shown in figure 4.13.

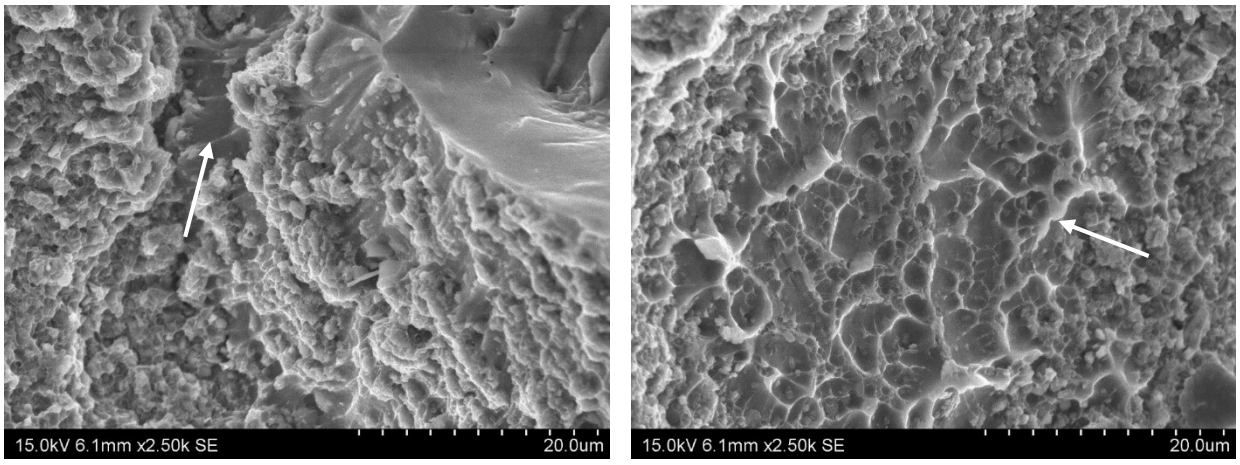

(a) (b)

Figure 4.13. *Fractography – T7 heat treated A205 after 1000 hours thermal exposure times at 200ºC showing signs of extensive plastic deformation - (a) long tear ridges(white arrow); (b) large dimples(white arrow).*

4.2.3 Effect of testing temperatures

A decreasing trend in both yield strength and ultimate tensile strength was observed with increasing testing temperature, as shown in figure 4.14a. But the elongation increased until 150^{o}C and then decreased as shown in figure 4.14b. The decreasing trend in yield strength and ultimate tensile strength can be attributed to the increased mobility of dislocations at elevated temperatures and further activation of cross-slip mechanisms in the material that would not be operating at room temperatures. The reason behind the decrease in elongation could be because of either one or both of the following reasons:

1. The mobility of dislocations increase so much that the annihilation of dislocations become very significant leading to a decrease in dislocation density, thereby limiting the plastic deformation possible. This could explain the shallow dimples specifically seen in specimens fractured at above 150^{o}C as shown in figure 4.15.

2. At elevated temperatures, vacancy diffusion mechanisms becomes active, which helps with void nucleation. As a result of increased and easier nucleation of voids, the plastic strain the matrix can take up before failure reduces. This increased number of voids can explain the fine size of dimples in the microvoid coalescence zone as shown in figure 4.15.

Several other causes could be postulated to reason out the increased number of shallow dimples and finer voids such as the size distribution of precipitates that nucleates voids. However, there is no conclusive proof found as for what has caused the reduction in elongation. Although the same trend was followed by specimens after prolonged thermal exposure at 150^{o}C and 200^{o}C, the peak elongation occurred at a temperature of 200^{o}C rather than at 150^{o}C.

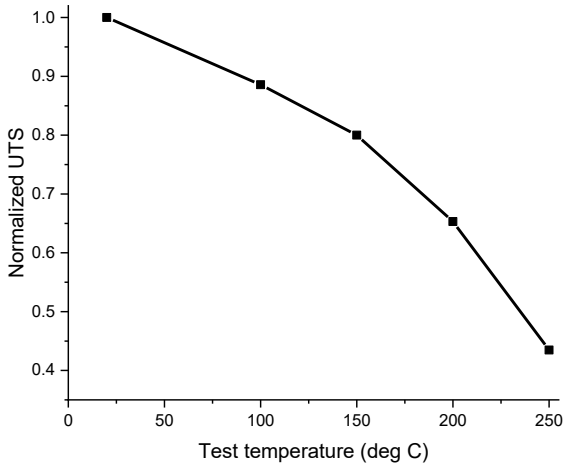

(a)

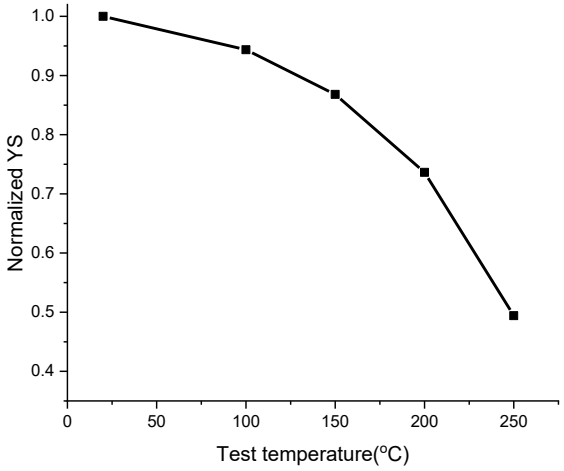

(b)

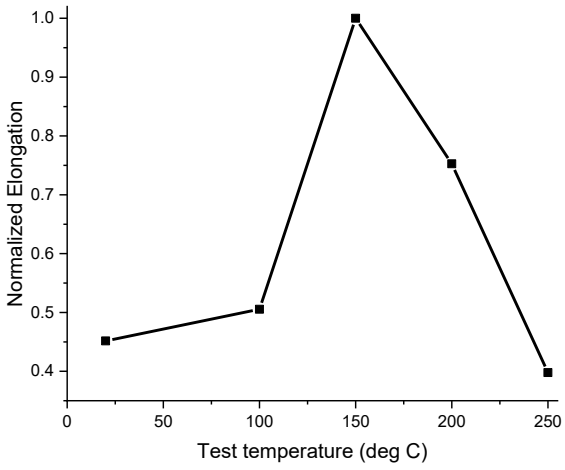

(c)

Figure 4.14. *Effect of testing temperature on tensile properties((a) UTS and YS; (b) Elongation) of T7 heat treated A205.*

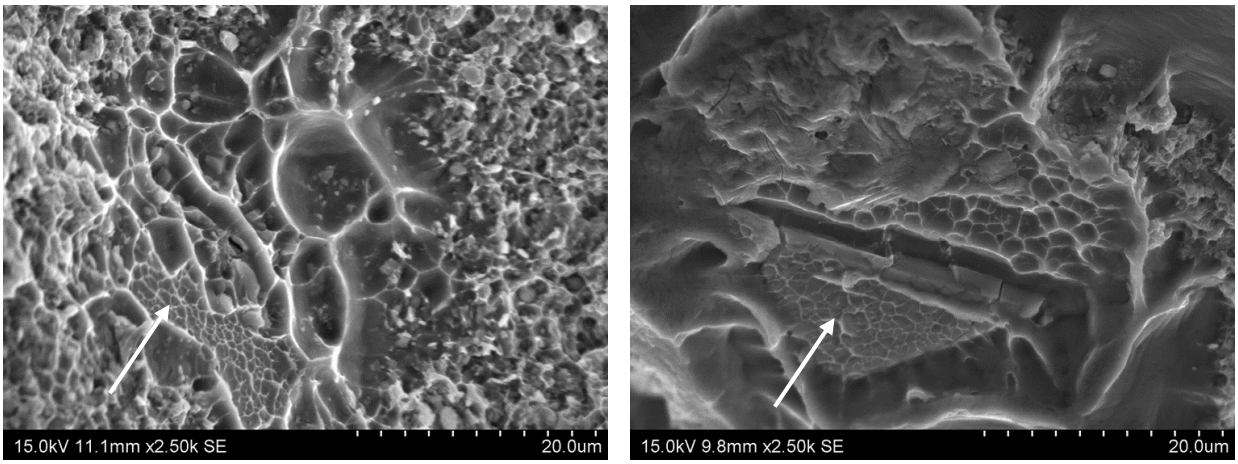

(a) (b)

Figure 4.15. *Shallow dimples(white arrows) characteristic to T7 heat treated A205 specimens tensile tested above 150°C.*

4.2.4 Casting defects in tensile tested specimens

In some cases, the tensile properties at same testing conditions for same thermal histories showed a huge scatter. The scatter was more significantly noticed in the elongation values and not much in yield strength and ultimate tensile strength values. The reason behind this can be attributed to the defects in the material.

1. Porosities

Both shrinkage porosities and probably gas porosities were noticed as shown in figure 4.16. The sizes varied from 100 to 300 microns. J Forde's work on A205 suggests, improper control on cooling rates and TiB_2 distribution can lead to shrinkage porosities[23]. The casting process has to be stringently controlled to prevent both types of porosities.

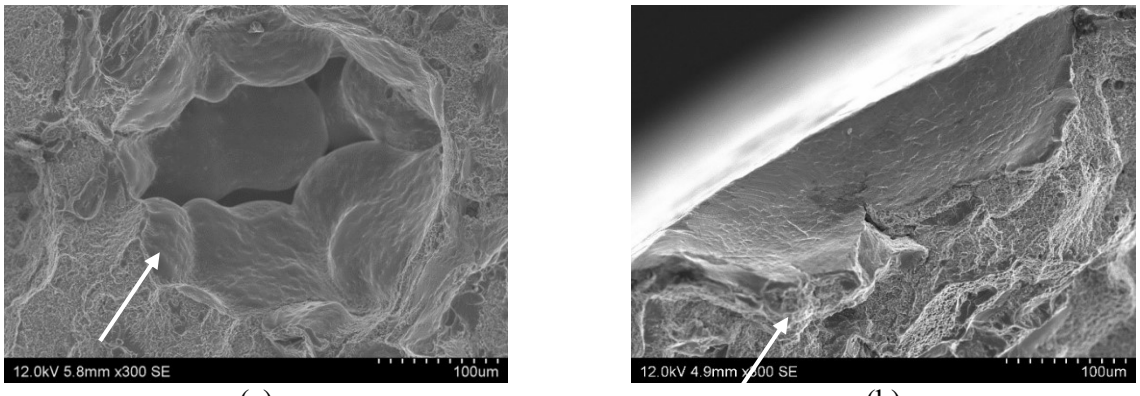

(a) (b)

Figure 4.16. *Porosities in tensile tested material - (a) Shrinkage porosity(white arrow) (b) possible gas porosity(white arrow).*

2. Oxide inclusions

The oxide inclusions appeared in two different morphologies on the fractured surfaces. The bigger oxide inclusions had a striped or a slaggy morphology as shown in figure 4.17a and figure 4.17b respectively. The specimen with the oxide inclusion shown in figure 4.17b showed very poor elongation remarkably lesser than the minimum elongation define by AMS4471. Typically, the oxides appear as a very thin layer and can sometimes go undetected by EDS analysis. This is also why the chemical composition analysis of oxide inclusions by EDS technique does not give stable results. Table 4.1 shows results from EDS analysis on two of the oxides. Throughout the fractured surface, the oxides also appeared as rounded zones as shown in figure 4.18. The reason behind these inclusions can be attributed to poor casting process.

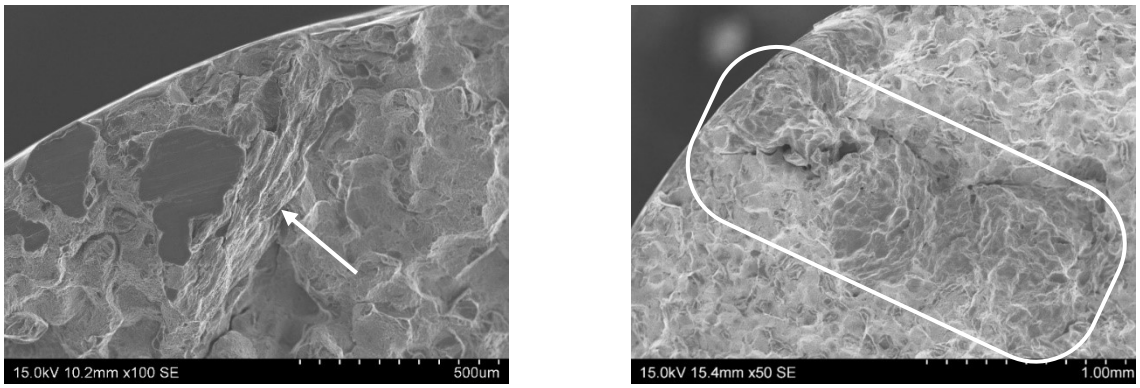

(a) (b)

Figure 4.17. *Oxide inclusions in tensile tested material - (a) striped morphology(white arrow) (b) slaggy morphology(white box).*

Table 4.1. *EDS analysis on two oxides*

Element	**O**	**Cu**	**Al**	**Ti**
Weight%	5.95	3.07	47.49	43.49
	2.51	10.2	76.9	10.32

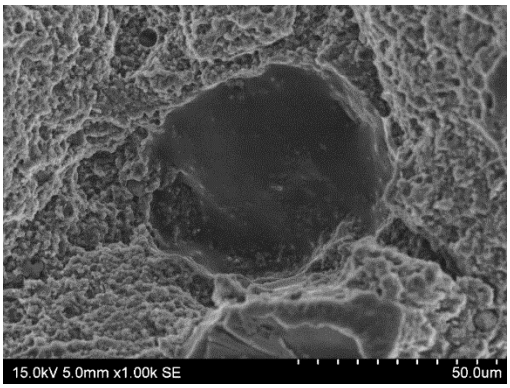

Figure 4.18. *Typical morphology of rounded oxide zones found on fractured surfaces*.

3. Cryolite inclusions

Cryolite inclusions are very common in TiB_2 reinforced Al cast alloys. Generally, cryolite based inclusion looked spherical and they appeared in sizes between 10 and 50 microns on the fractured surfaces as shown in figure 4.19. Being rich in K and F, as shown in table 4.2, they are present as a result of entrapment during the casting process. Their presence as observed in TiB_2 reinforced A201[33] and A205[23] has been known to be detrimental to mechanical properties. They also seem to have a poor bonding with the matrix.

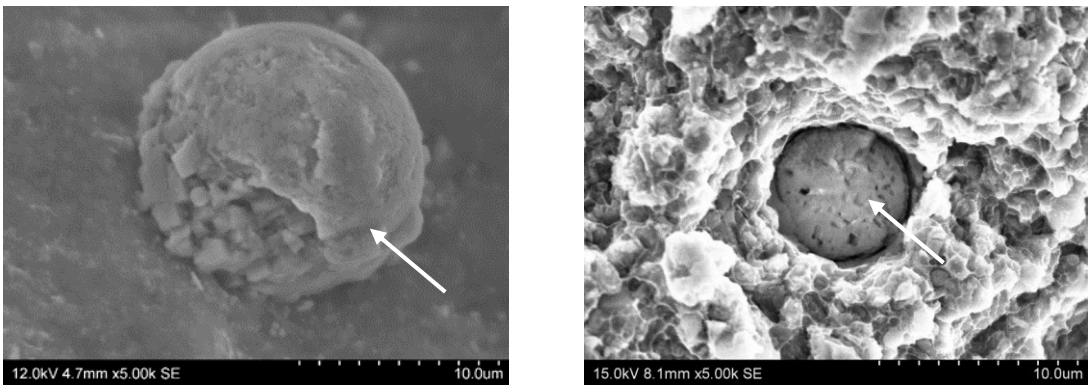

(a) (b)

Figure 4.19. *Cryolite inclusion in tensile tested material - (a) Inclusion on an oxide zone (b) Inclusion embedded in the matrix.*

Table 4.2. *EDS analysis on a cryolite inclusion*

Element	**F**	**Mg**	**Al**	**K**	**Ti**
Weight%	20.01	15.56	12.95	47.51	3.97

4.2.5 Al_3Ti on crack propagation

Irrespective of the testing conditions, bulky Al_3Ti particles have effectively assisted crack propagation. Al_3Ti particles being brittle and embedded in a relatively soft matrix, with increasing stresses as the matrix begins to yield, stress created by strain field around Al_3Ti particles increases leading to their failure even before the crack reaches them. The broken Al_3Ti particles act as voids that the crack propagates through revealing the broken Al_3Ti particles on the fractured surface(figure 4.20). Figure 4.20b shows how a part of material was scooped through as the crack propagated through broken Al_3Ti particle. Figure 4.21 shows a simple schematic as to how the bulky particles catalyse the crack propagation by void nucleation. Although the same theory can apply to TiB_2 particles, the effect can be imagined to be less significant as the particles are very small(approx. 1 micron) compared to Al_3Ti particles(10 to 100 microns). The region around Al_3Ti particles are always smooth characterized with tear ridges. This could mean that, the region is deprived of any brittle particles and this region is possibly just the plastic α-aluminium matrix. Although the exact processing method is unknown, the distribution and volume fraction of Al_3Ti depends on the amount of free titanium in the alloy. A hyper-peritectic Al-Ti composition is chosen deliberately to have free titanium forming Al_3Ti in the melt. Literature suggest that, the morphology of Al_3Ti can be controlled by introducing an agitation of the melt. For example, Jin Qin et al has investigated the effect of ultrasonic vibration on in-situ formation of Al_3Ti[59]. The ultrasonic vibration seems to break the Al_3Ti into small particles resulting in a finer distribution. On the contrary, it is plausible that, building turbulence in the melt can provide more ways for entrapment of oxides formed on the surface of the melt. Therefore, the casting process needs careful optimization of process parameters.

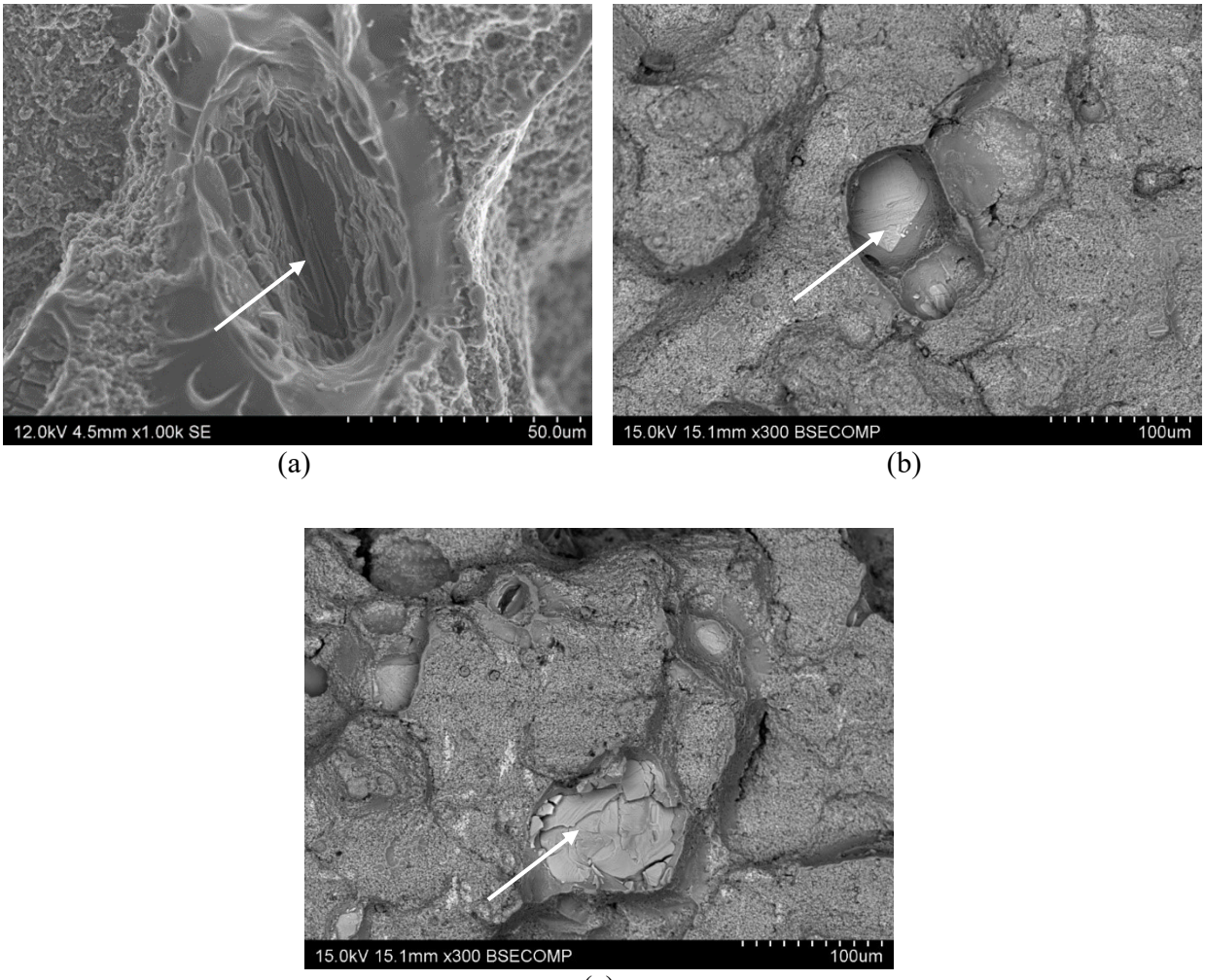

(a) (b)

(c)

Figure 4.20. *Bulky Al_3Ti particles as seen on tensile tested A205 specimens((a)Al_3Ti particle in SE mode(white arrow); (b and c) Al_3Ti particle in BSE mode(white arrows)).*

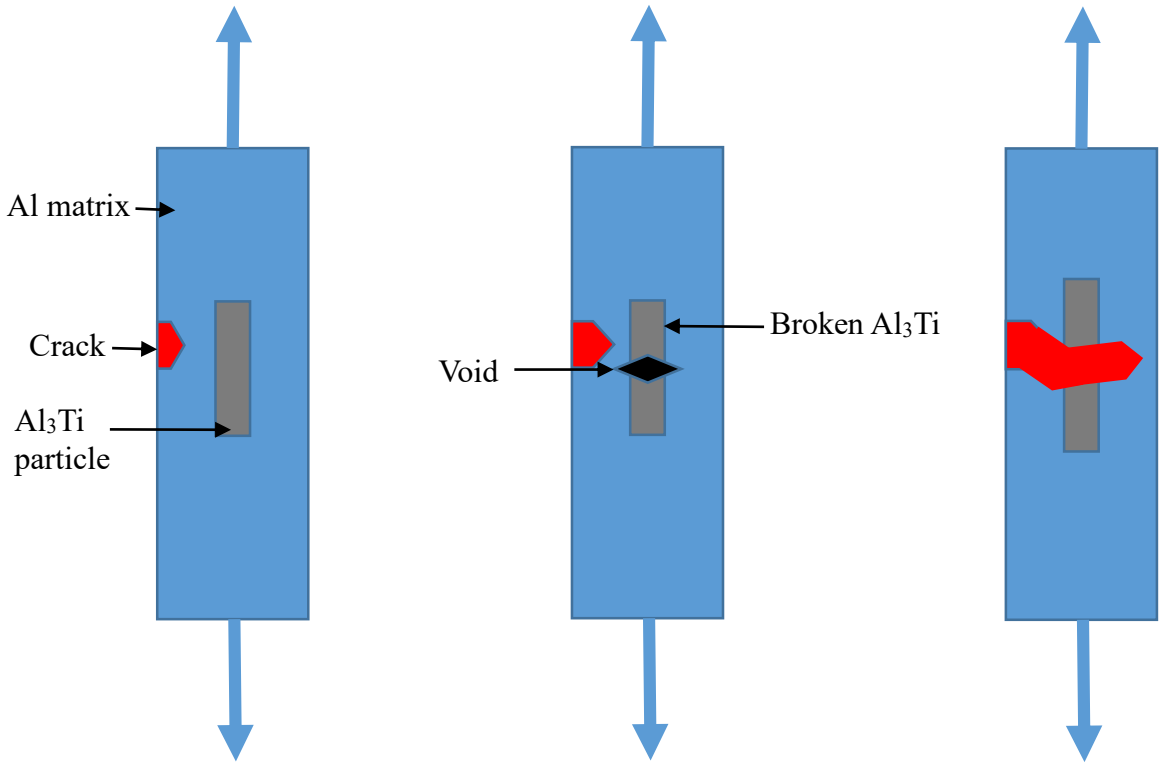

Figure 4.21. *Schematic diagram – Bulky Al_3Ti particles assisting crack propagation(left to right). (a)A brittle bulky Al_3Ti particle embedded in the matrix with an approaching crack front. As the stress applied increases, (b)the brittle particle breaks nucleating a void as big as the cross section of the particle which (c)assists the crack front to advance or allows for easier void coalescence.*

4.3 Low cycle fatigue(LCF) properties

The three batches of specimens investigated as mentioned in Section 3.2.3 were named Batch A, Batch B and Batch C.

4.3.1 Effect of testing temperature

Batch C specimens were tested at room temperature and elevated temperatures. With increasing strain ranges the fatigue life went down, as the magnitude of cyclic stresses acting on the material increases with strain range. Figure 4.21 shows that there is no inferable effect of testing temperature on fatigue life. If there was an inferable correlation between the testing temperature and fatigue life, there would be a segregation of points corresponding to different testing temperatures. Therefore, it would not make a difference if all the data points from testing at different testing temperatures were treated the same. In reality as the increased mobility of dislocations at elevated temperatures increases the ductility and reduces the yield strength, a difference in fatigue life at room temperature and elevated temperatures was expected.

4.3.2 Effect of Hardness/Aging time

Figure 4.23 shows the effect of aging times on fatigue life in different batches of specimens analyzed. The data points are colored according to the aging time. There was no pattern observed to determine the effect of aging time or hardness of the material on the fatigue life. In reality, the LCF life depends on the hardness of the matrix more than the microstructural aspects such as the grain size, as it would be harder for the crack to propagate through a harder material when controlled crack growth regime is followed. This is due to reduced size of plastic zones created at the tip of growing crack front as the hardness of the matrix increases[23,41]. When the matrix is very soft, as in the overaged conditions, the plastic zone at the propagating crack tip will be huge as well thereby accelerates the crack propagation.

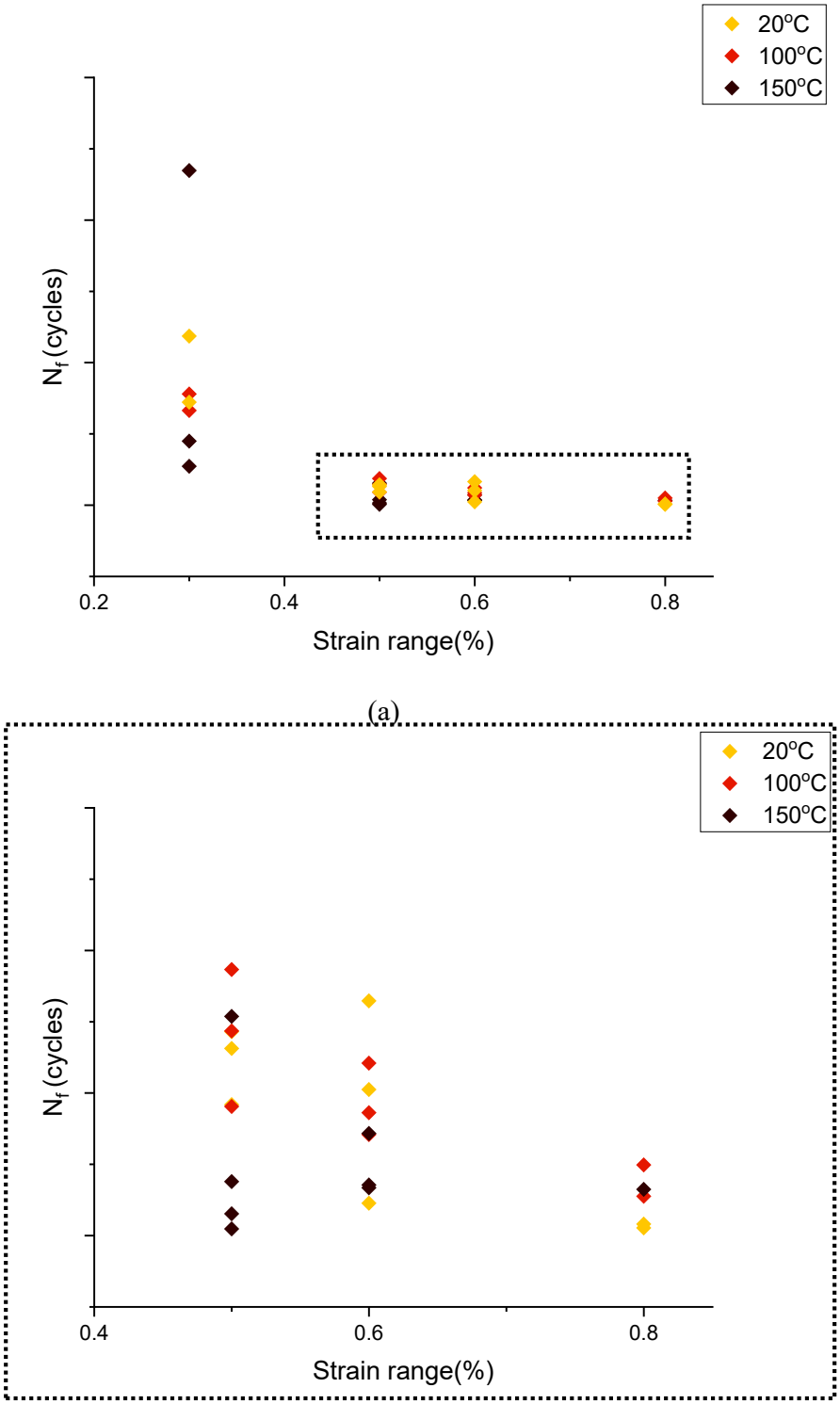

Figure 4.22. *LCF life(N_f) of T7 heat treated A205(Batch C) tested at different temperatures(coloured as shown in legend). The clustered data points in (a) corresponding to test strain ranges above 0.3% are expanded in (b)[Y-axis has been removed for confidentiality purposes]*

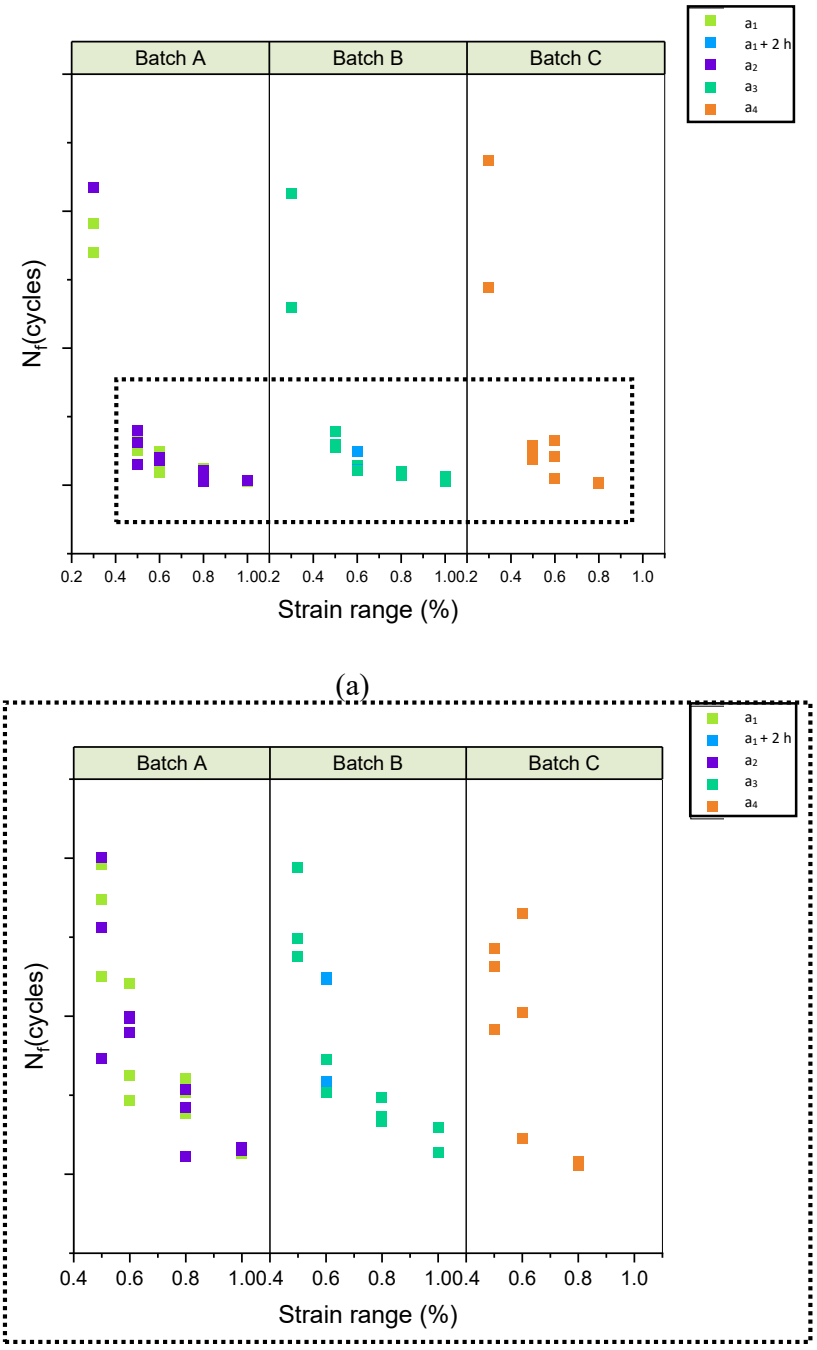

Figure 4.23. *LCF life(N_f) of Batches – A, B and C of A205 tested at different strain ranges after different aging times(coloured as shown in legend). The clustered data points in (a) corresponding to test strain ranges above 0.3% are expanded in (b) [Y-axis has been removed for confidentiality purposes]*

4.3.3 Fractography

Irrespective of testing and heat treatment conditions of A205, fractography of all the specimens analyzed showed the three typical fatigue failure zones as shown in figure 4.24.

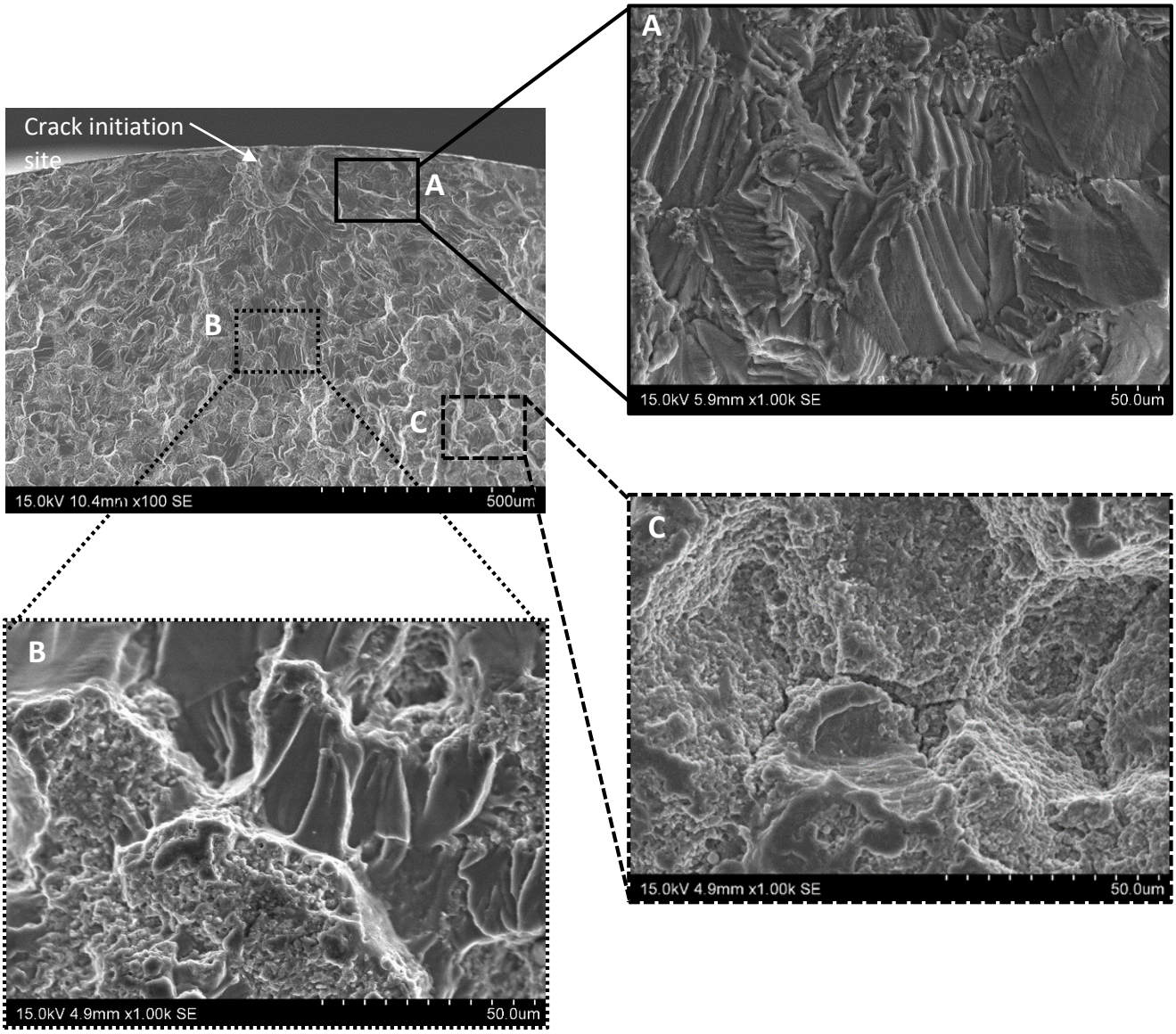

Figure 4.24. *Typical fractured surface of LCF tested A205 specimen with clear crack initiation site and different crack propagation zones. Region A - Transgranular faceted crack growth close to initiation; Region B - Mixed faceted crack growth and microvoid coalescence; Region C – Mixded microvoid coalescence and intergranular cracking.*

1. Crack initiation

The initiator was always an oxide inclusion or a porosity. The crack initiator was always on the surface of the specimen or slightly under the surface. Figure 4.25 shows the typical crack initiators present in the material. Literature suggests that, the number of cycles for fatigue crack initiation goes down with the presence of defects. In a cast A356 alloy, a critical defect size(25-50 microns) was identified below which the defect would not initiate a crack[60]. Even if A205 was assumed to have critical defect size close to that of A356, the initiating defects present in the specimens were significantly bigger. Table 4.3 shows the size ranges of defects identified.

Table 4.3. *Types of fatigue crack initiator(defect) and size ranges in which they appeared on fractured surfaces*

Initiator	**Size range (microns)**
Oxide inclusion	100-1000
Porosity	100-300

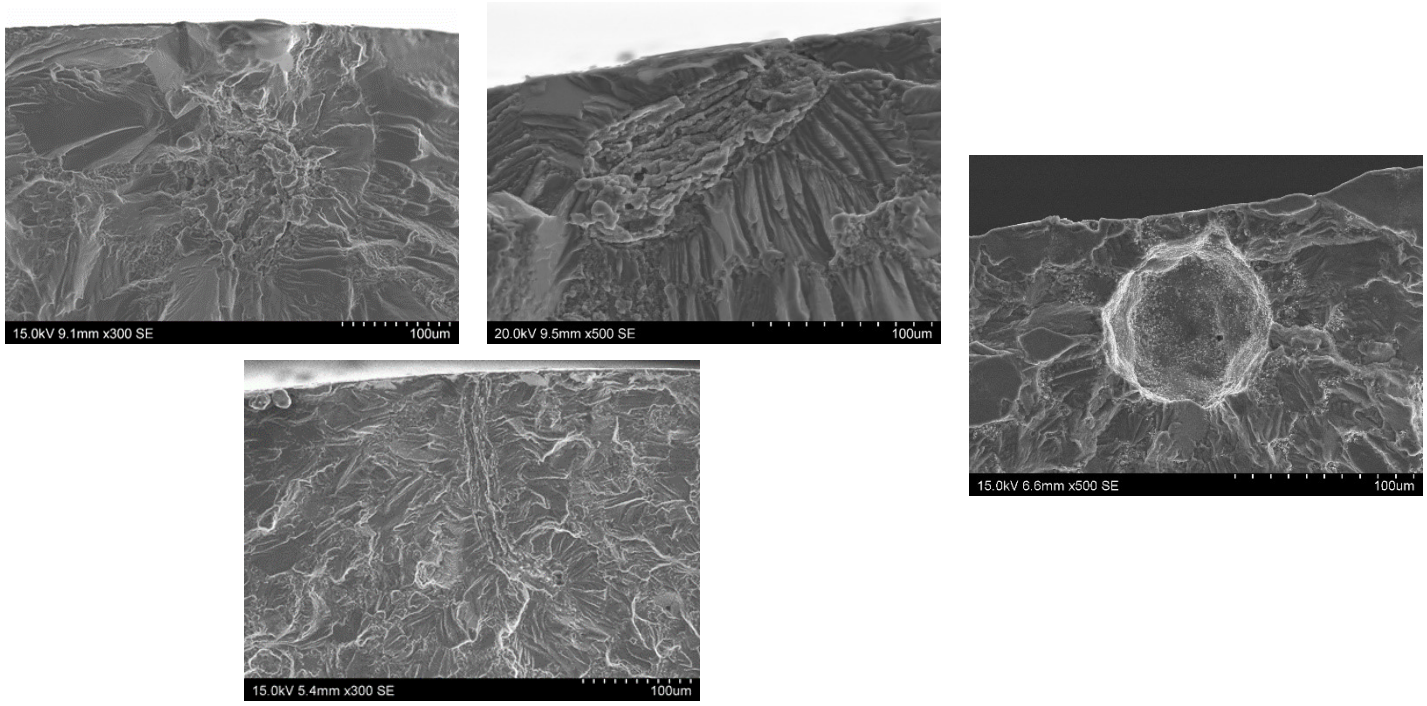

(a) (b)

Figure 4.25. *Typical crack initiators - (a) Oxide inclusions in LCF (b) Porosity.*

2. Controlled-crack growth zone

The controlled crack growth region where the crack propagation was trans-granular was relatively very small compared to the overstress region. This region was marked by river marks pointing toward the initiator. There was not much interaction between Al_3Ti particles and the crack. The markedly small size of the region relative to the area of fractured surface insinuates that, the life is defined by the initiator rather than the hardness and other factors that improve crack propagation resistance.

3. Overstress region

This region is characterized by uncontrolled propagation of crack to failure. After crossing the Paris-law regime, the crack propagation switches to overstress regime marked by mechanisms happening at static tensile conditions – inter-granular cracking and microvoid coalescence. In the overstress region, there were iron rich zones which were clearly highlighted by BSE contrast under SEM as shown in figure 4.26. The rod shaped structures seen at higher magnifications could be Cu_2FeAl_7 intermetallic precipitates that supposed take blade-shaped morphology[61]. This could affect the mechanical properties in two ways – 1. Consumes Cu available for precipitation strengthening 2. Being brittle, brings the strength of the material down by allowing the crack to propagate easily.

Although not noticed in many specimens, there was a gradual transition between the controlled crack growth zone and over-stress region as shown in Figure 4.24(Region B). Figure 4.24 shows crack propagation mechanisms changing from the initiation site on the surface.

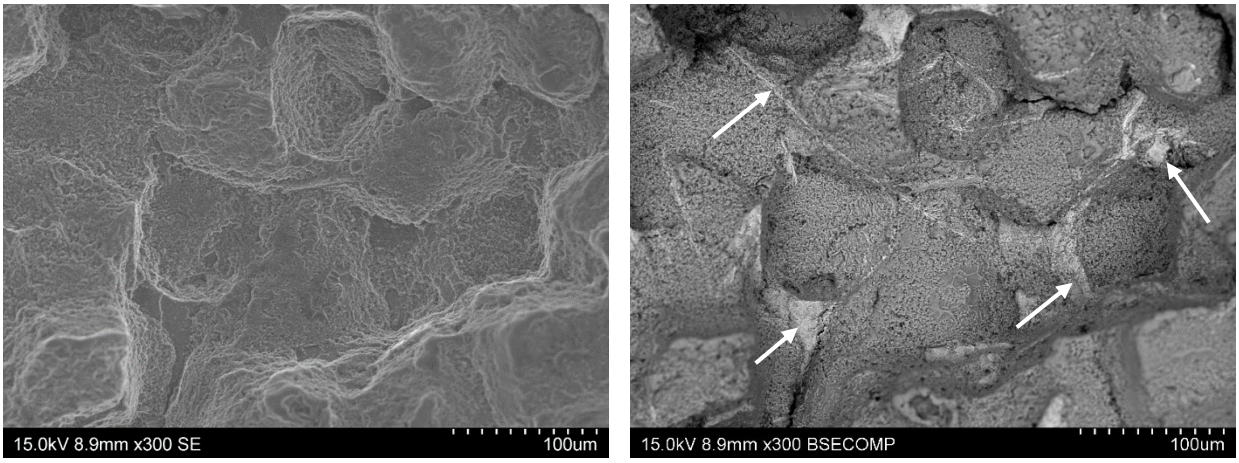

(a)

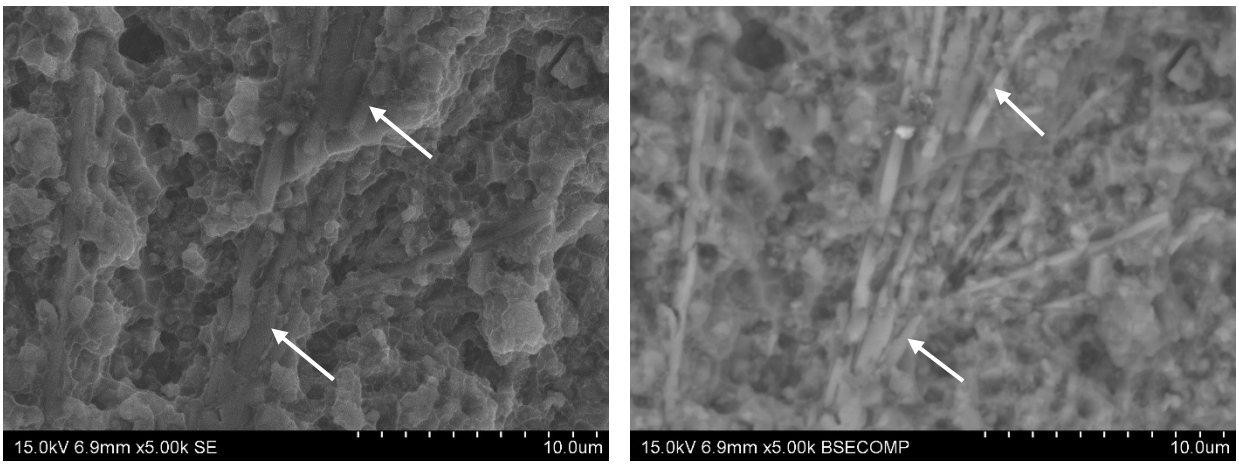

(b)

Figure 4.26. *Fractographs showing Fe-rich zones in LCF tested specimens – (a) SE(left) and BSE(right) image of overstress region at 300x(white arrows); (b) SE(left) and BSE(right) image of overstress region at 5000x showing Fe-rich intermetallic rods(white arrows).*

4.3.4 Effect of crack initiator on fatigue life

An inevitable relationship between the defect size and fatigue life was expected. As seen from figure 4.25 the oxide inclusions took several morphologies while the porosities were usually spherical. It is plausible that, there are probably many other factors that decide the number of cycles for crack initiation. To restrict the investigation time and keeping the correlation simple, two parameters were selected with the defect size – position and type of the defect for understanding the fatigue failure mechanism.

4.3.4.1 Effect of defect size and defect position

Figure 4.27 shows the fatigue life of the material irrespective of the processing conditions and microstructure as a plot against the size of the defect that initiated the crack. The plots were made for different strain ranges to eliminate the effect of strain range. In most cases, a decreasing trend in fatigue life was noticed with an increase in defect size. On the other hand, in many cases, the fatigue life was slightly better when the crack initiating defect was present under the surface rather than at the surface. For example, with batch-B specimens tested at 0.8% strain range, as indicated by an arrow in figure 4.27, the specimen with a bigger defect and present under the surface has shown a slightly better life than the specimen with a smaller defect under the surface.

4.3.4.2 Effect of defect size and defect type

On plotting the same plot as in the previous case but coloring the data-points depending on the type of defect, no inferable correlation could be made between the type of the defect and the fatigue life as shown in figure 4.28.

It can be inferred that, the defect size plays a more significant role than the other characteristics considered. In an ideal scenario, the defects have to be completely controlled if the fatigue life has to be improved. HIP-ing and melt filtration techniques are some procedures that can be looked into, to control the defects.

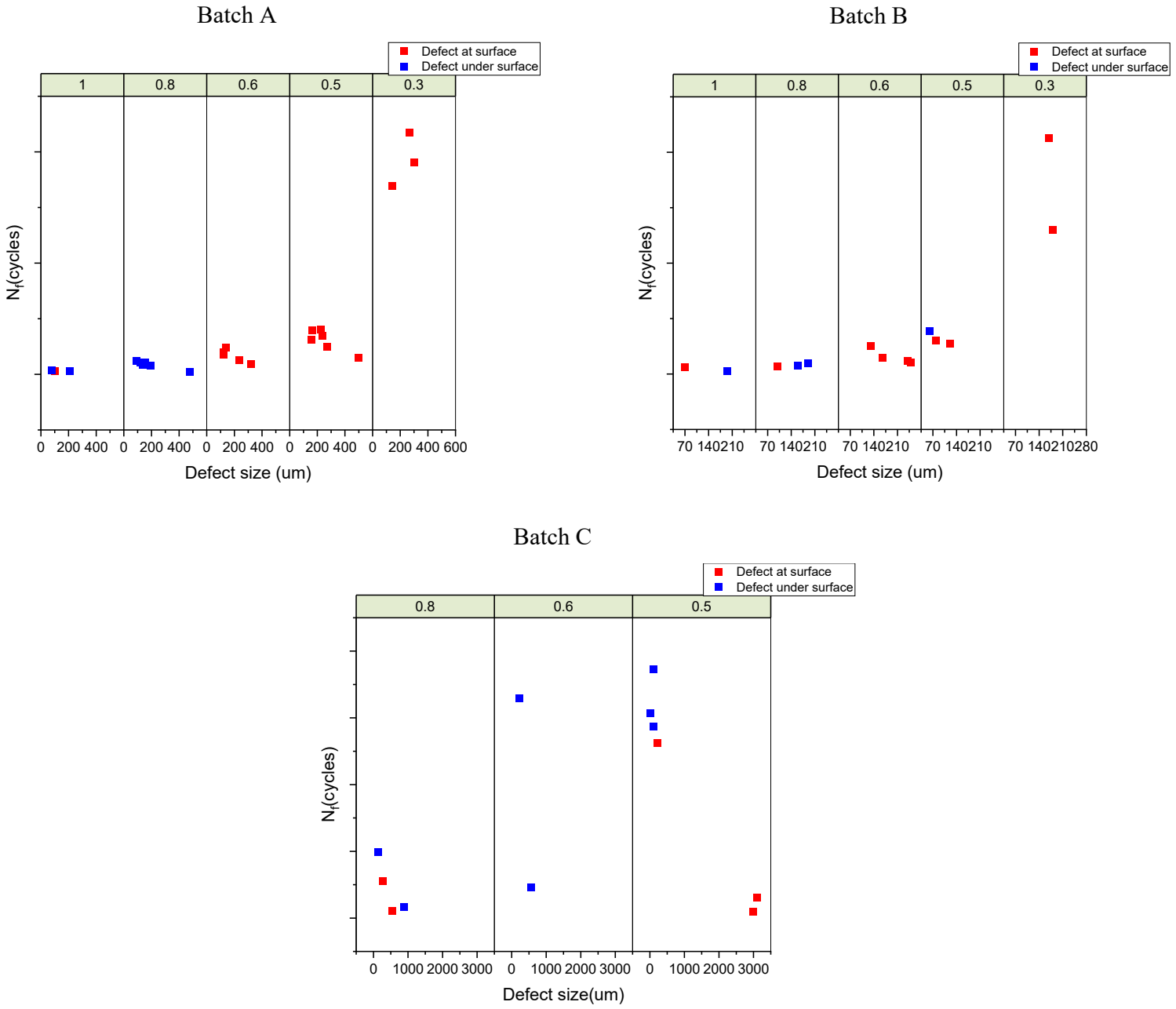

Figure 4.27. S*ize and position(coloured as shown in legend) of defect that initiated fatigue crack vs LCF life. The columns indicate the strain ranges at which the LCF tests were done. [Y-axis has been removed for confidentiality purposes]*

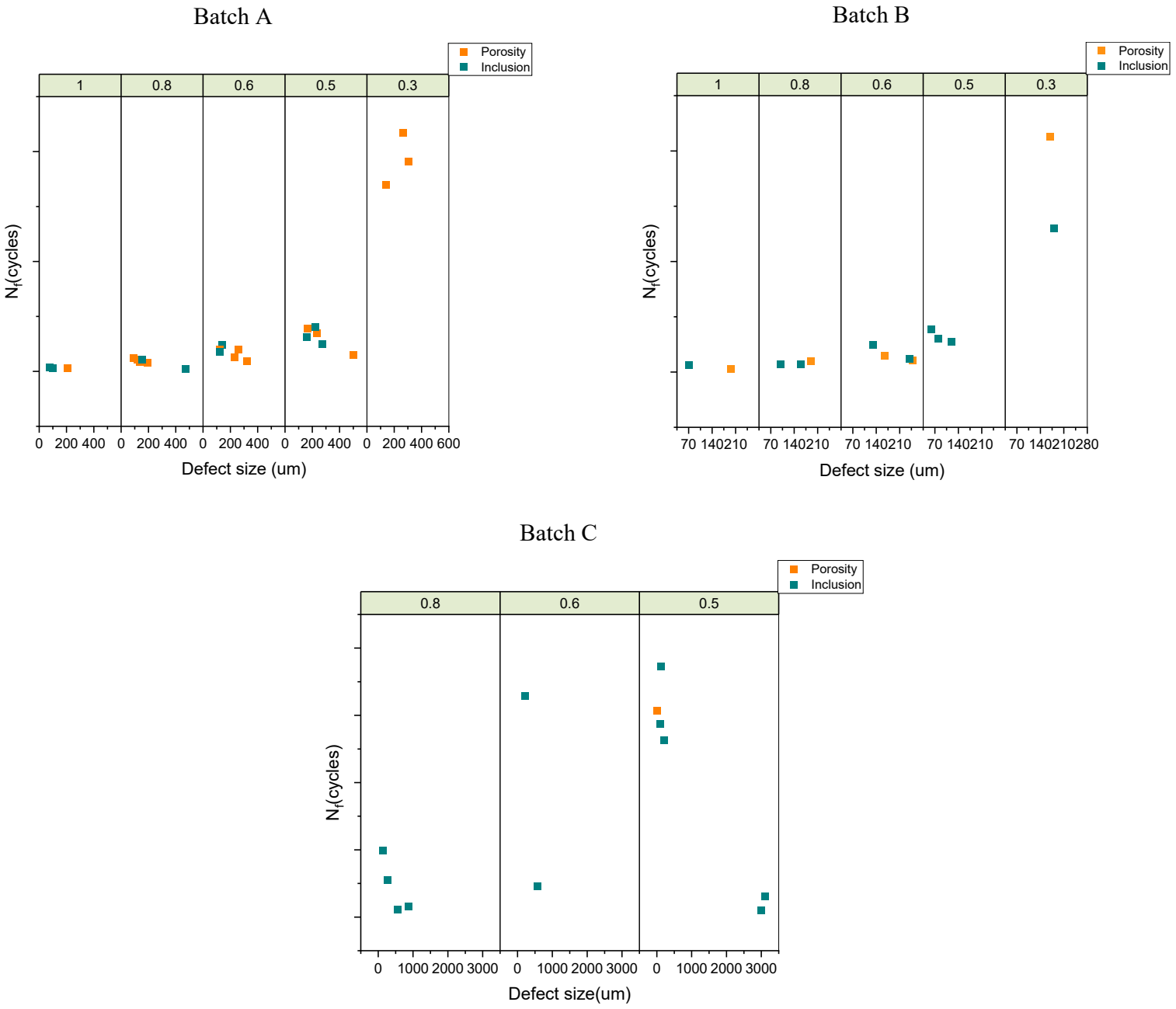

Figure 4.28. S*ize and type(coloured as shown in legend) of defect that initiated fatigue crack vs LCF life(N_f). The columns indicate the strain ranges at which the LCF tests were done. [Y-axis has been removed for confidentiality purposes]*

4.4 Property prediction

4.4.1 ThermoCalc for A205

ThermoCalc's equilibrium calculator is used to have an idea of stable phases possibly present in the material under equilibrium conditions at a range of temperatures. Therefore it could be used to ascertain if the right solutionizing temperature is used, for example. For precipitation simulation, Prisma – a ThermoCalc module was used.

4.4.1.1 Equilibrium calculations with ThermoCalc

Before the strength prediction, the applicability of ThermoCalc for equilibrium calculations were studied**.** The composition of A205 as per AMS4471 was given as input except Fe and Si which are assumed to be impurities for simulation. It is to be noted that Ti and B are input as free elements. So, the results would not be a direct correlation of the salt-melt reaction. Equilibrium calculator was used to predict the phases forming when the alloy solidifies and the result is shown in figure 4.29.

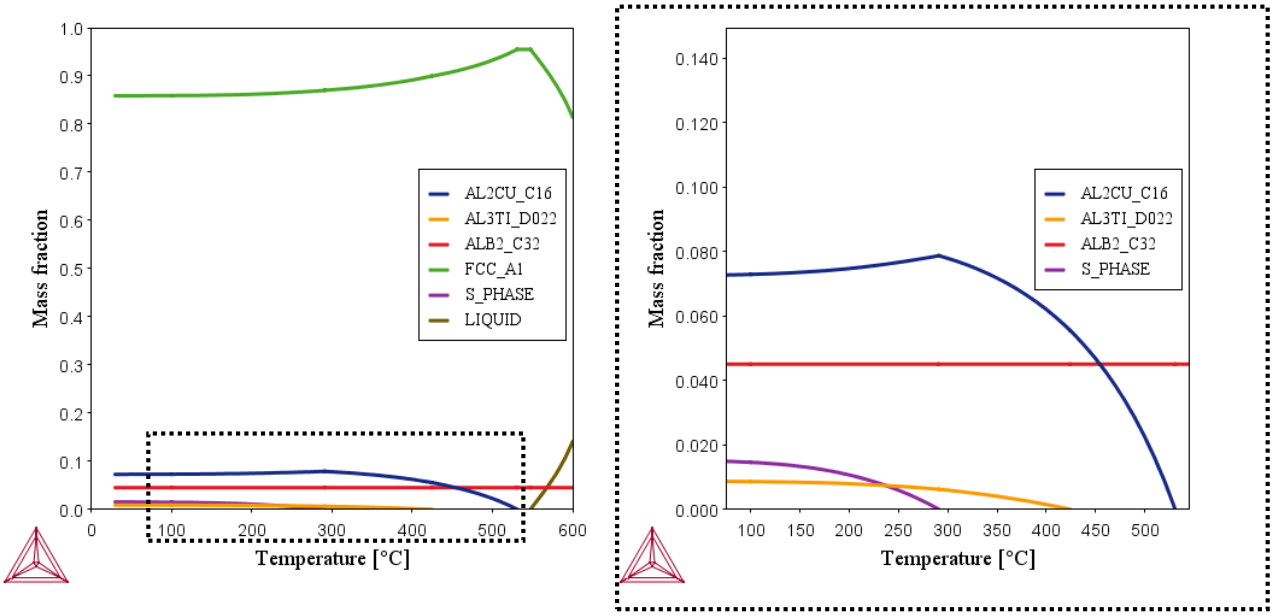

Figure 4.29. *Equilibrium diagram generated by ThermoCalc-2019a for A205 between 30°C and 600°C(left)*; *Expanded scale showing the dissolution of $CuAl_2$ phase at solutionizing temperatures(right).*

The different phases that ThermoCalc predicted to form were correlated as:

1. FCC_A1 : Primary aluminium phase with FCC structure
2. AL2CU_C16: Al_2Cu forming in as cast structure
3. AL3TI_D022: Accommodates the Al_3Ti phase that forms from the salt-melt reaction
4. ALB2_C32: Accommodates the TiB_2 particles
5. S_PHASE: Al_2CuMg intermetallic phase

ThermoCalc compares the input composition with existing databases and uses the parameters of alloys in database to calculate free energies for formation of a particular phase. One has to be aware of what phases can exist and suppress them in the software appropriately for optimum results. As for A205, Al-Cu-Mg-Ag database does not exist[62]. Therefore, it is probable that, the thermodynamic parameters used by ThermoCalc are very approximate.

From theoretical calculations 4.5 wt% of TiB_2 should be formed for the input composition, as rightly predicted by ThermoCalc(figure 4.30a). On contrary, ThermoCalc predicts complete dissolution of Al_3Ti phase at solutionizing temperatures(figure 4.30b). But this is in contradiction with experimental results, as Al_3Ti was still observed after solutionizing(figure 4.31). Al_3Ti forms in the melt from the reaction between precursor salts and molten aluminium. But this reaction cannot be considered by ThermoCalc as it currently calculates the fraction of Al_3Ti from the amount of free titanium in the melt. This could be a possible reason behind the discrepancy. Also, the processing conditions as followed by the manufacturer are quite obscure at the moment making it hard to derive a conclusion.

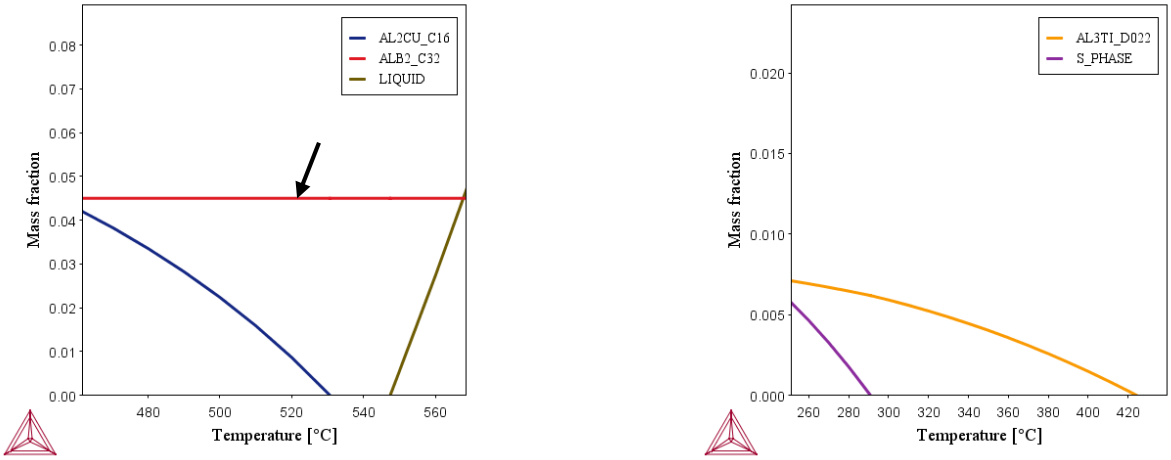

Figure 4.30. *Equilibrium diagram showing (a) amount of TiB_2 formed(arrow) (b) dissolution of Al_3Ti phase.*

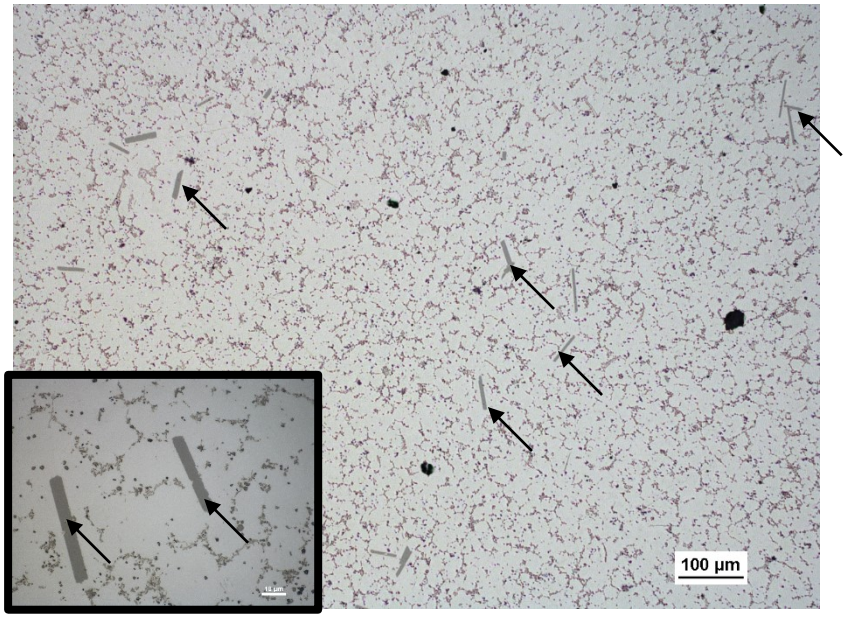

Figure 4.31. *Microstructure of A205(Batch A) showing the presence of Al_3Ti(black arrows) after solution treatment and water-quenching.*

On the other hand, JMatPro, for a close composition but without silver seems to predict the fraction of Al_3Ti more accurately as shown in figure 4.32. The result is from simulation work done on A205 by GKN Aerospace earlier.

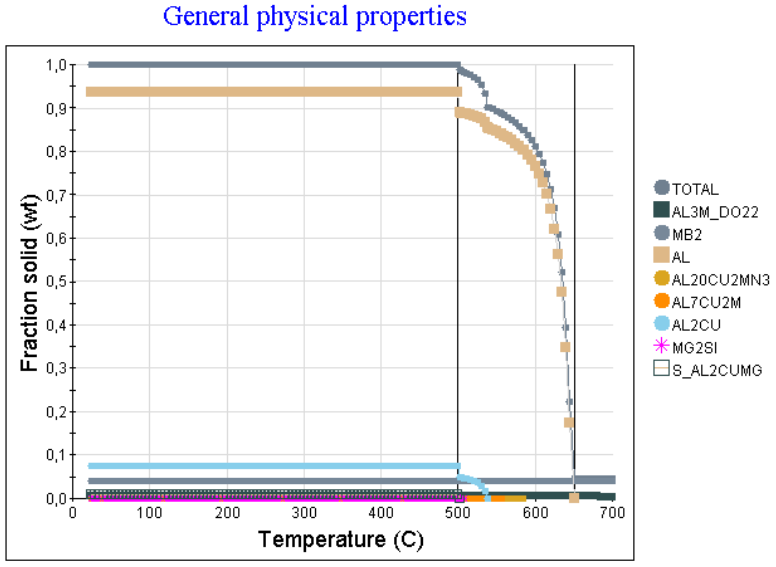

Figure 4.32. *Equilibrium weight fractions of phases from JMatPro as predicted for A205 composition without silver showing a stable Al_3Ti phase even above melting temperatures.*

4.4.1.2 Precipitation characteristics – ThermoCalc PRISMA

For the sake of simulation, the θ' and Ω phases are not distinguished and every precipitate is assumed to be θ'. It is understood that θ' evolves through trasient phases – GP zones and θ''. For a better understanding, TTT curves as predicted by JMatPro is shown for the GP zones and incoherent $CuAl_2$ phase(θ) are shown in figure 4.33. The TTT curves for θ' should lie between the two curves. The property model calculator of ThermoCalc was used to investigate how the software treats the transient zones. Reliable values available in literature for interfacial energies of θ' are 0.235 J/m^2 and 0.615 J/m^2 for the coherent and incoherent surfaces respectively. Table 4.4 shows that none of the phases associate with $CuAl_2$ has an interfacial energy close to this. It should be noted that the interfacial energies can differ a lot based on the method used for calculation[63]. Additionally, Prisma does not accommodate the anisotropy in interfacial energy. Theoretically, the difference could be accommodated by controlling the transformation strain energy in different directions.

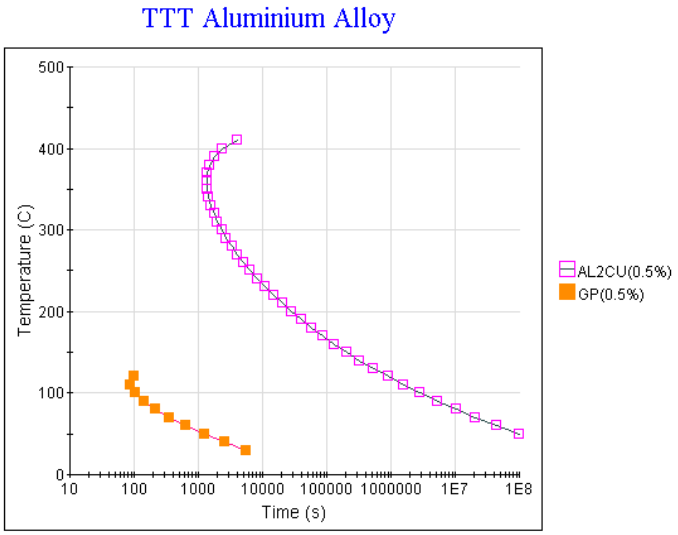

Figure 4.33. *TTT curves for GP zones and $CuAl_2$ phases as predicted by JMatPro in A205 with silver.*

Table 4.4. *Interfacial energies of all $CuAl_2$ precipitation phases in TCAL6-ThermoCalc database.*

	θ''	θ'	Ω	θ
ThermoCalc's database	0.029 J/m^2	0.045 J/m^2	0.07 J/m^2	0.11 J/m^2

4.4.1.2.1 Need for calibrating Prisma

In an ideal case, the database should rightly take all the parameters necessary for precipitation calculations. If all the input parameters are set default, Prisma predicts a diameter less than 5 nm after a_4 hours of aging at 170°C. It cannot be true as from the experimental results and literature[22]. Therefore, a complete refitting and optimization of database parameters are required to properly use Prisma for any precipitation calculations. Some efforts were put in to optimize the model by trial-and-error as explained in the next section.

4.4.1.2.2 Calibrating Prisma

In order to calibrate the model, the important input parameters for a particular chemical composition that affected the precipitation characteristics were identified as:

1. Number of nucleation sites
2. Interfacial energy
3. Type of precipitate (θ' or Ω)
4. Morphology of precipitate(+aspect ratio for non-sherical precipitates)
5. Molar volume of matrix and precipitates
6. Transformation strains
7. Elastic properties of matrix

After several correspondances with ThermoCalc, it was understood that, most of the above parameters were to be fixed arbitrarily and optimized so that, they fit well with the experimental results. Even if a particular set of parameters seemed to work well for certain conditions, it might not work at other thermal conditions.

Insipite of the major drawbacks stated, to make the best out of Prisma, the precipitates were imaged to calibrate Prisma by fixing most of the parameters as default and optimizing only the aspect ratio and number of nucleation sites. The specimens used for precipitate analysis were the ones thermally exposed at 150°C and 200°C for 100 hours and 1000 hours. The resolution of FEG-SEM which falls at around 10 nm was not enough to resolve the precipitates especially, the thickness of the precipitates. For calculation, the coarsest of the resolved precipitates that were chosen for size analysis. Literature suggests that, the aspect ratio decreases in overaging conditions[52]. The trend followed by dimensions

of the coarsest precipitates are shown in figure 4.34. An increase in aspect ratio was noted with exposure times. The coarse precipitates selected for dimensional analysis might not be representative of all the precipitates in the matrix.

For the purpose of calibration, the thickness was neglected and only the diameter of the precipitates was considered. By fixing the aspect ratio and number of nucleation sites arbitrarily as 10 and 1E21 /m^3, a reasonable but significantly off values were predicted by Prisma as shown in figure 4.35.

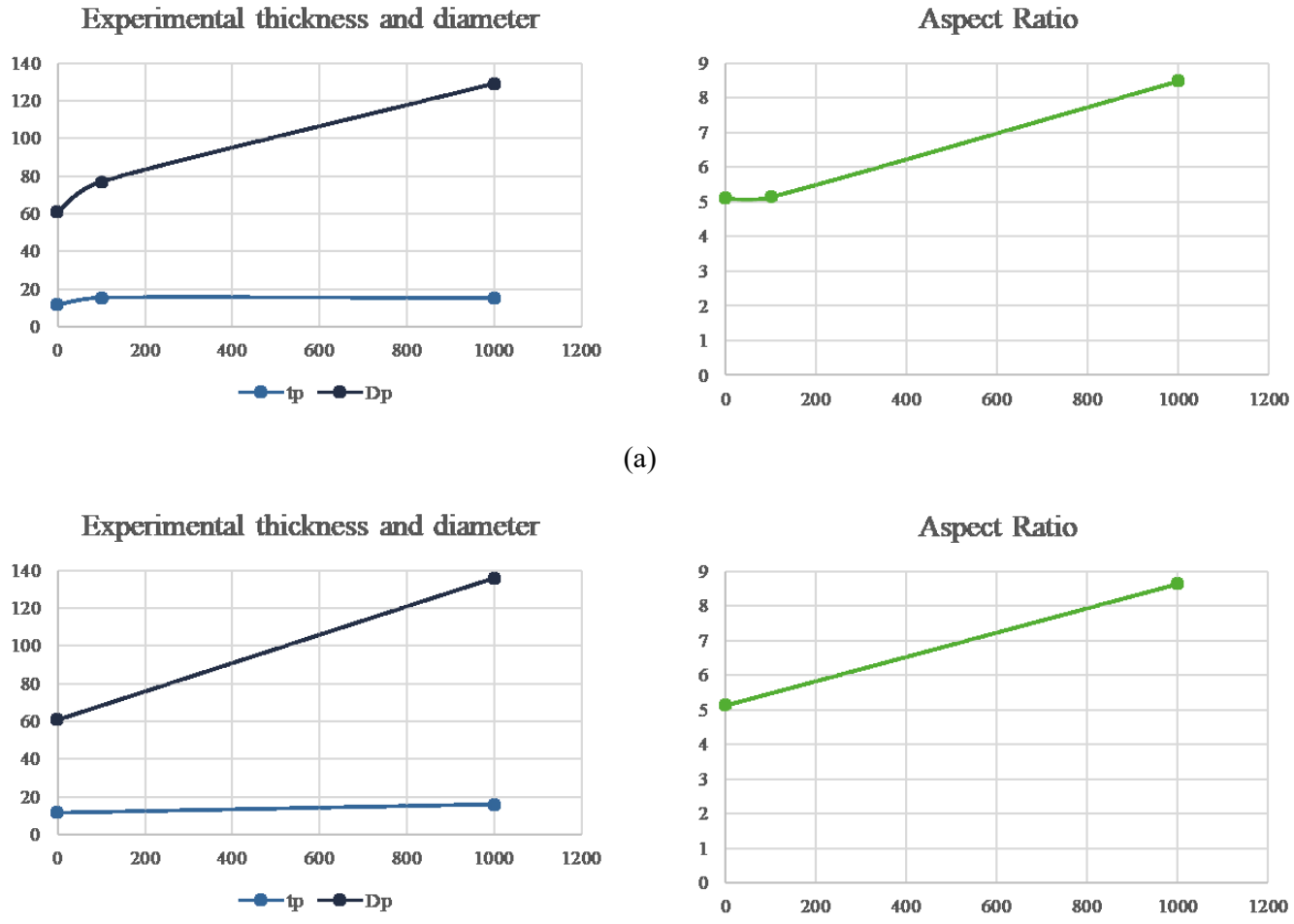

Figure 4.34. *Evoution of mean diameter, thickness and aspect ratio during thermal exposure of T7 Heat treated A205(as measured on coarsest particles) at (a)150°C and (b)200°C.*

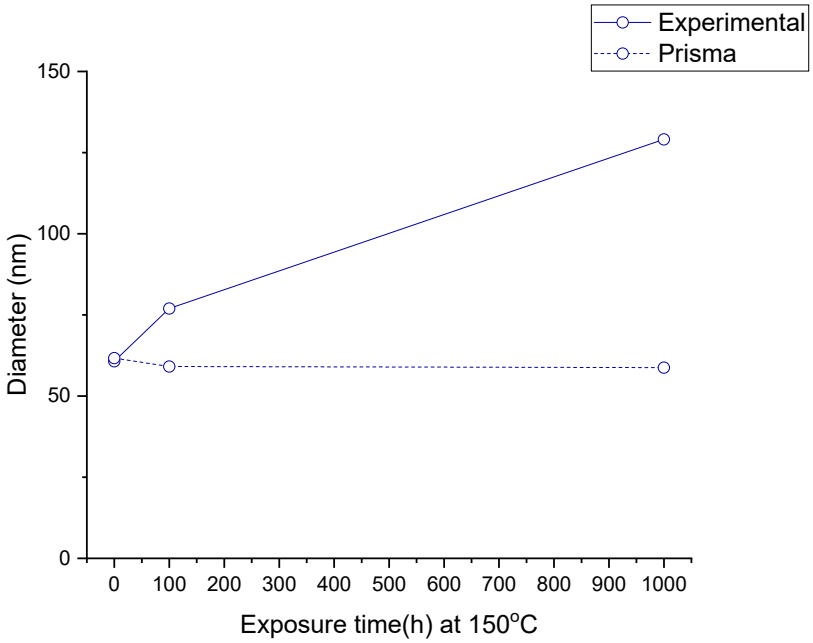

(a)

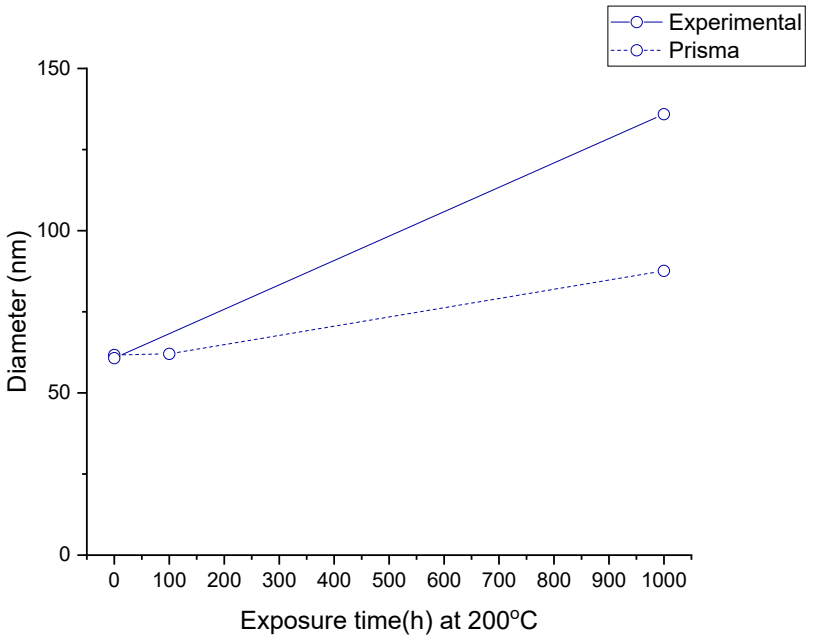

(b)

Figure 4.35. *Predicted $CuAl_2$ precipitate diameter by fixing AR as 10 and number of nucleation sites as 1E21 /m^3 compared against experimental(coarsest) diameter in T7 heat treated A205 during prolonged thermal exposure at (a)150°C and (b)200°C.*

4.4.2 Larson-Miller Parameter

Since Prisma, at the moment, fails to predict the precipitation characteristics after aging and extended thermal exposures, it renders the strength models identified for strengthening Al-Cu-Mg alloys unusable[49,53]. There was a need to find another functional tool for strength prediction. The LM-parameter relates the temperature and time into a single entity as:

$$P = T(C + \log t) \quad \text{…Exp. 4.1}$$

where T is the temperature in Kelvin, C is a constant and t is time in hours.

The parameter is widely used for creep-rupture analysis as the time required for creep-rupture for every temperature and stress are sanely impossible to experiment[64]. The LM-parameter serves as a valuable tool to extrapolate the creep-rupture time for a stress and a temperature while keeping the amount of experiments reasonably limited. While there are a few other high temperature to extrapolate high-temperature properties, LM-parameter is the most simple yet functional[65]. In aluminium alloys, the parameter has been widely used for creep analysis but not much for yield strength prediction[66,67]. As the expression would suggest, the partameter varies linearly as a function of temperature but exponentially with time. In other words, the temperature has a huge influence on the LM-parameter than time. Generally, C varies from 13 to 27 for aluminium alloys and in most cases it is approximated to 20.

For strength-prediction after thermal exposure, a similar model used by Samuel et al for thermal aging of steels[68]. The yield strength could be related to the LM-Paramter as a polynomial function:

$$\sigma_y = a_0 + a_1 P + a_2 P^2 + \cdots \quad \text{…Exp. 4.2}$$

where σ_y is the yield strength in MPa and P is defined by Exp. 4.1. To reduce complexity, the polynomial can be approximated to the second degree. In order to calculate the coefficients in the polynomial, the experimental yield strength values were used with LM-Parameters calculated from the four thermal exposure conditions – 150ºC and 200ºC for 100 h and 1000 h. The coefficients for a close fit with the experiment values were calculated as *-2250*, *0.6236* and *-4E-5* for a_o, a_1 *and* a_2 respectively. The experimental and fitted curve for the variation in yield strength to LM-Parameter are shown in figure 4.36.

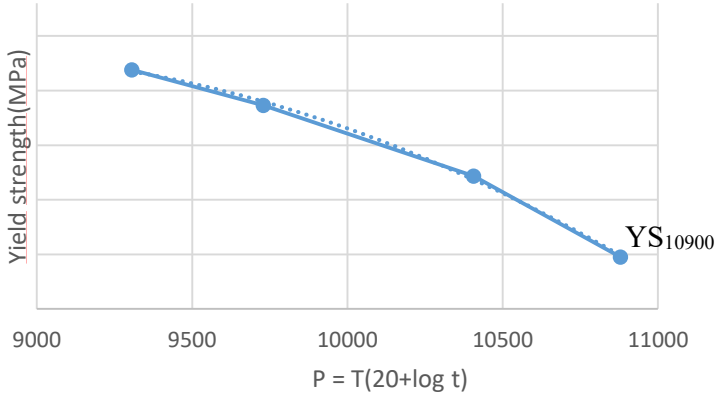

Figure 4.36. *Yield strength vs LM parameter (Solid – Experimental; Dotted – Polynomial fit) [Y-axis has been removed for confidentiality purposes]*

Since the polynomial function is fit with experimental values from two different temperatures, the fitted equation should logically accommodate the overaging effect on the yield strength from coarsening of precipitates during thermal exposure. It is both evident and logical that, the coarsening is more aggressive at 200°C than at 150°C. Even though the difference in temperature is just 50 K, the parameter is fit so that the time that would take to produce an equivalent change in yield strength is exponentially high. For example, it takes 1000 hours at 200°C(P=10900) for the yield strength to decrease to YS_{10900} MPa(in figure 4.36). For the yield strength to decrease to YS_{10900} MPa from thermally exposing at 150°C, it would take 515,000 hours. This makes sense because, there is no significant coarsening of $CuAl_2$ happening at 150°C.

Literature suggests that, the Ω-$CuAl_2$ precipitates coarsen more aggressively when the exposure temperature crosses 250°C. Therefore, this polynomial fit might not be applicable to predict the yield strength when exposure temperatures are higher than 250°C. Since the potential operating temperatures will be less than 200°C, the proposed tool can be very functional. It could be used to extrapolate the time required for the yield strength to cross a cut-off value at a particular operating temperature below which it will be considered failed. It might be interesting to have more data-points to validate the accuracy of the polynomial function.

It should be noted that, the precipitate nucleation, growth and coarsening characteristics can change with the processing conditions that dictates the microstructural features. Before one can implement this tool for yield strength prediction, the processing conditions and microstructure should be standardized and the coefficients in Exp. 4.2 should be optimized.

4.4.3 Aging optimization tool

As per specifications, T7 heat treatment of cast A205 involves solution treatment followed by quenching and aging at 170°C for a_4 hours(the nomenclature representing the aging times is mentioned in Section 3.2.1). The aim of T7 heat treatment is to slightly overage the material which increases the ductility and resistance to stress corrosion cracking. The aging time can be brought down by increasing the aging temperature with a small compensation on peak hardness reached. This fact is also proved experimentally for A205 as reported in Section 4.1.3 of this chapter. If the small reduction in hardness can be accommodated, then a huge amount of time can be saved on aging by optimizing the temperature. For an approximate estimation of time(t_2) required at an aging temperature(T_2) to attain an equivalent hardness attained at someother aging time(t_1) for a temperature(T_1), a general equation has been identified from literature[2]:

$$t_2 = \frac{t_1}{\exp\left(\frac{32562}{T_1+460} - \frac{32562}{T_2+460}\right)} \quad \text{…Exp. 4.3}$$

where times are in hours and temperatures are in Farenheit.

To validate this mathematical tool, the existing results from Section 4.1.3 were used. To find the time from aging at 205°C to have a hardness equivalent to the hardness from a_4 hours of aging at 170°C, the tool was used to find that, it takes a bit less than b_1 hours which seems to be fairly right as the hardness is approaching close to the peak hardness. On reversing the calculation by using b_1 hours at 205°C which is the point at which the peak hardness is reached, the tool predicts a few hours more than a_4 hours to be the time to reach peak hardness from aging at 170°C.

While it is very attractive to reduce the aging time, there might be a significant effect on stress corrosion cracking resistance. Therefore, several investigations are to be done in order to properly optimize the aging conditions.

Chapter 5

Conclusions

A general understanding on the effect of T7 heat-treatment as-cast A205 was acquired. The solutionizing step increases the hardness of the material in the first 10 hours but then reaches a plateau. The reason behind the increase in hardness has been attributed to the solid solution strengthening effect of Cu that is entering the matrix during solutionizing. The reason behind saturation in hardness after 10 hours is not conclusive. But it is speculated to be due to complete dissolution of $CuAl_2$ into the matrix. The relaxation step between solutionizing and aging seems to improve the hardening effect from precipitation treatment (aging) but, the improvement is not significant. The aging temperature influences the hardening behavior. By increasing the aging temperature from 170ºC to 205ºC, the peak hardness was reached at a much earlier time(time reduced by approximately 15 times). There was a slight compensation on the peak hardness reached. Through appropriate tests, the aging conditions can be optimized to reduce the time of heat treatment.

The effect of prolonged elevated temperature exposures at 150ºC and 200ºC on tensile properties of T7-heat treated A205 was investigated. Exposing at 200ºC has been found to be more detrimental to the strength than exposing at 150ºC. The reason behind the weakening has been attributed to the coarsening of precipitates. The effect of testing temperatures on tensile properties was also investigated. The yield strength and ultimate tensile strength drops continuously with increasing testing temperatures while the elongation varies in a low-to-high-to-low fashion with increasing testing temperatures. Bulky Al_3Ti particles have catalyzed fracture and there is positively some room for improvement by controlling the morphology and distribution of these particles. Several defects were identified to introduce huge scatters in the tensile properties.

The effect of hardness on LCF properties of A205 at different aging conditions and the effect of testing temperature on T7 heat treated A205 were investigated. Neither the hardness nor the testing temperature had any influence on the fatigue life. This indifference was attributed to the presence of defects – mostly porosities or oxide inclusions, at or close to the surface of the specimens and have always initiated the fatigue crack. The defect characteristics were correlated with the fatigue life. The position of the defect seemed to have some influence over the fatigue life but the type of defect did not seem to play any

significant role in defining the life. Hot isostatic pressing(HIP-ing) and melt filtration techniques could be interesting procedures to look into for mitigating the occurrence of identified defects.

The applicability of ThermoCalc's Equilibrium calculator and Prisma module for precipitation simulation has been studied. ThermoCalc needs a lot of work before it can be applied for A205 both for equilibrium calculations and precipitation simulation. The role of input parameters that affect the computational equations behind the precipitation simulation was understood. It was also identified that more powerful imaging techniques with better resolution such as TEM are required to image the precipitates properly in order to calibrate Prisma accurately. Regardless, the reliability of Prisma for precipitation simulation in A205 is questionable.

By using the experimental results two mathematical tools have been identified and proposed for A205. Larson-Miller Parameter seems to fit well into a polynomial equation that could be used to interpolate yield strength after prolonged thermal exposures at temperatures less than 200^{o}C. Another tool to optimize aging times at different aging temperature also seems to agree well with the experimental results.

Bibliography

1 Gayle, F. W. & Goodway, M. Precipitation hardening in the first aerospace aluminum alloy: the Wright flyer crankcase. *Science* **266**, 1015-1017 (1994).

2 Davis, J. R. *Aluminum and aluminum alloys*. (ASM international, 1993).

3 Jones, D. R. & Ashby, M. F. *Engineering materials 2: an introduction to microstructures, processing and design*. (Elsevier, 2005).

4 Zolotorevsky, V. S., Belov, N. A. & Glazoff, M. V. *Casting aluminum alloys*. Vol. 12 (Elsevier Amsterdam, 2007).

5 Yu, H., Xin, Y., Wang, M. & Liu, Q. Hall-Petch relationship in Mg alloys: A review. *Journal of Materials Science & Technology* **34**, 248-256 (2018).

6 Orowan, E. Fracture and strength of solids. *Reports on progress in physics* **12**, 185 (1949).

7 Gladman, T. Precipitation hardening in metals. *Materials science and technology* **15**, 30-36 (1999).

8 Brooks, C. R. Heat treatment. *Structure and Properties of Nonferrous Alloys*, 120-150 (1982).

9 *The Aluminum (Al) - Copper (Cu) System*, <https://www.tf.uni-kiel.de/matwis/amat/iss/kap_8/advanced/a8_2_2.html> (

10 Williams, J. C. & Starke Jr, E. A. Progress in structural materials for aerospace systems. *Acta Materialia* **51**, 5775-5799 (2003).

11 Bray, G., Glazov, M., Rioja, R., Li, D. & Gangloff, R. Effect of artificial aging on the fatigue crack propagation resistance of 2000 series aluminum alloys. *International Journal of Fatigue* **23**, 265-276 (2001).

12 Association, A. *Aluminum: properties and physical metallurgy*. (ASM international, 1984).

13 Liu, J., Yang, S., Wang, S., Chen, J. & Wu, C. The influence of Cu/Mg atomic ratios on precipitation scenarios and mechanical properties of Al–Cu–Mg alloys. *Journal of Alloys and Compounds* **613**, 139-142 (2014).

14 Taghiabadi, R., Mahmoudi, M., Emamy Ghomy, M. & Campbell, J. Effect of casting techniques on tensile properties of cast aluminium alloy (Al–Si–Mg) and TiB2 containing metal matrix composite. *Materials science and technology* **19**, 497-502 (2003).

15 Hatch, J. E. Aluminium: Properties and Physical Metallurgy, by ASM. *Metals Park, OH*, 135 (1984).

16 Polmear, I. Effects of small additions of silver on aging of some aluminum alloys. *Transactions of the Metallurgical Society of AIME* **230**, 1331-& (1964).

17 Taylor, J., Parker, B. & Polmear, I. Precipitation in AI-Cu-Mg-Ag casting alloy. *Metal Science* **12**, 478-482 (1978).

18 Polmear, I. J. *et al.* in *Materials Science Forum.* 1759-1764 (Trans Tech Publ).

19 Rosalie, J. M. & Bourgeois, L. Silver segregation to θ′(Al2Cu)–Al interfaces in Al–Cu–Ag alloys. *Acta Materialia* **60**, 6033-6041 (2012).

20 Knowles, K. & Stobbs, W. The structure of {111} age-hardening precipitates in Al–Cu–Mg–Ag alloys. *Acta Crystallographica Section B: Structural Science* **44**, 207-227 (1988).

21 Reich, L., Murayama, M. & Hono, K. Evolution of Ω phase in an Al–Cu–Mg–Ag alloy—a three-dimensional atom probe study. *Acta Materialia* **46**, 6053-6062 (1998).

22 Hutchinson, C., Fan, X., Pennycook, S. & Shiflet, G. On the origin of the high coarsening resistance of Ω plates in Al–Cu–Mg–Ag alloys. *Acta materialia* **49**, 2827-2841 (2001).

23 Forde, J. *The elevated temperature performance of cast aluminium alloys and the development of a cast aluminium-copper metal matrix composite*, University of Birmingham, (2015).

24 M. Gazizov, R. K. Precipitation structure and strengthening mechanisms in an Al-Cu-Mg-Ag alloy. *Materials Science and Engineering: A* **702**, 29 - 40, doi:https://doi.org/10.1016/j.msea.2017.06.110 (2017).

25 Abarghouie, S. M. & Reihani, S. S. Aging behavior of a 2024 Al alloy-SiCp composite. *Materials & Design (1980-2015)* **31**, 2368-2374 (2010).

26 Shorowordi, K. M., Laoui, T., Haseeb, A., Celis, J.-P. & Froyen, L. Microstructure and interface characteristics of B4C, SiC and Al2O3 reinforced Al matrix composites: a comparative study. *Journal of Materials Processing Technology* **142**, 738-743 (2003).

27 Lü, L., Lai, M., Su, Y., Teo, H. & Feng, C. In situ TiB2 reinforced Al alloy composites. *Scripta Materialia* **45**, 1017-1023 (2001).

28 Lu, L., Lai, M. & Chen, F. Al-4 wt% Cu composite reinforced with in-situ TiB2 particles. *Acta Materialia* **45**, 4297-4309 (1997).

29 Akbari, M. K., Baharvandi, H. & Shirvanimoghaddam, K. Tensile and fracture behavior of nano/micro TiB2 particle reinforced casting A356 aluminum alloy composites. *Materials & Design (1980-2015)* **66**, 150-161 (2015).

30 Youssef, Y., Dashwood, R. & Lee, P. Effect of clustering on particle pushing and solidification behaviour in TiB2 reinforced aluminium PMMCs. *Composites Part A: Applied Science and Manufacturing* **36**, 747-763 (2005).

31 Schaffer, P. L., Miller, D. N. & Dahle, A. K. Crystallography of engulfed and pushed TiB2 particles in aluminium. *Scripta Materialia* **57**, 1129-1132 (2007).

32 Schaffer, P. L. & Dahle, A. K. Settling behaviour of different grain refiners in aluminium. *Materials Science and Engineering: A* **413**, 373-378 (2005).

33 Butler, S. A. *The development of a reliable high strength aluminium casting alloy*, University of Birmingham, (2000).

34 Davies, I. G., Dennis, J. M. & Hellawell, A. The nucleation of aluminum grains in alloys of aluminum with titanium and boron. *Metallurgical Transactions* **1**, 275-280, doi:10.1007/bf02819272 (1970).

35 Gao, Q. *et al.* Improvement of particles distribution of in-situ 5 vol% TiB2 particulates reinforced Al-4.5 Cu alloy matrix composites with ultrasonic vibration treatment. *Journal of Alloys and Compounds* **692**, 1-9 (2017).

36 Wang, S. & Starink, M. Review of precipitation in Al–Cu–Mg (Li) alloys. *Int. Mater. Rev* **50**, 193-215 (2005).

37 Campbell, J. *Complete casting handbook: metal casting processes, metallurgy, techniques and design*. (Butterworth-Heinemann, 2015).

38 Buffiere, J.-Y., Savelli, S., Jouneau, P.-H., Maire, E. & Fougeres, R. Experimental study of porosity and its relation to fatigue mechanisms of model Al–Si7–Mg0. 3 cast Al alloys. *Materials Science and Engineering: A* **316**, 115-126 (2001).

39 Geng, J. *et al.* Tuning the microstructure features of in-situ nano TiB2/Al-Cu-Mg composites to enhance mechanical properties. *Journal of Alloys and Compounds* **775**, 193-201 (2019).

40 Doel, T. & Bowen, P. Tensile properties of particulate-reinforced metal matrix composites. *Composites Part A: Applied Science and Manufacturing* **27**, 655-665 (1996).

41 Chawla, N. & Shen, Y. L. Mechanical behavior of particle reinforced metal matrix composites. *Advanced engineering materials* **3**, 357-370 (2001).

42 Davis, L., Andres, C. & Allison, J. Microstructure and strengthening of metal matrix composites. *Materials Science and Engineering: A* **249**, 40-45 (1998).

43 Clyne, T. & Withers, P. *An introduction to metal matrix composites*. (Cambridge university press, 1995).

44 Doel, T., Loretto, M. & Bowen, P. Mechanical properties of aluminium-based particulate metal-matrix composites. *Composites* **24**, 270-275 (1993).

45 McDanels, D. L. Analysis of stress-strain, fracture, and ductility behavior of aluminum matrix composites containing discontinuous silicon carbide reinforcement. *Metallurgical transactions A* **16**, 1105-1115 (1985).

46 Lloyd, D. Aspects of fracture in particulate reinforced metal matrix composites. *Acta metallurgica et materialia* **39**, 59-71 (1991).

47 Kapoor, R. & Vecchio, K. S. Deformation behavior and failure mechanisms in particulate reinforced 6061 Al metal-matrix composites. *Materials Science and Engineering: A* **202**, 63-75 (1995).

48 Chen, Q., Wu, K., Sterner, G. & Mason, P. Modeling precipitation kinetics during heat treatment with CALPHAD-based tools. *Journal of materials engineering and performance* **23**, 4193-4196 (2014).

49 Li, Y. *et al.* Precipitation and strengthening modeling for disk-shaped particles in aluminum alloys: size distribution considered. *Materialia* **4**, 431-443 (2018).

50 Liu, H., Bellón, B. & Llorca, J. Multiscale modelling of the morphology and spatial distribution of θ′ precipitates in Al-Cu alloys. *Acta Materialia* **132**, 611-626 (2017).

51 (Thermo-Calc Software AB, 2019).

52 Liu, G., Zhang, G., Ding, X., Sun, J. & Chen, K. Modeling the strengthening response to aging process of heat-treatable aluminum alloys containing plate/disc-or rod/needle-shaped precipitates. *Materials Science and Engineering: A* **344**, 113-124 (2003).

53 Zhu, A. & Starke Jr, E. Strengthening effect of unshearable particles of finite size: a computer experimental study. *Acta materialia* **47**, 3263-3269 (1999).

54 *Precipitation hardening*, <https://en.wikipedia.org/wiki/Precipitation_hardening>

55 GKN Aerospace - Internal document 1

56 GKN Aerospace - Internal document 2

57 GKN Aerospace - Internal document 3

58 GKN Aerospace - Internal document - 4

59 Qin, J. *et al.* Formation of in-situ Al3Ti particles from globular Ti powders and Al alloy melt under ultrasonic vibration. *Journal of Alloys and Compounds* **653**, 32-38 (2015).

60 Wang, Q., Apelian, D. & Lados, D. Fatigue behavior of A356-T6 aluminum cast alloys. Part I. Effect of casting defects. *Journal of light metals* **1**, 73-84 (2001).

61 Tseng, C.-J., Lee, S.-L., Tsai, S.-C. & Cheng, C.-J. Effects of manganese on microstructure and mechanical properties of A206 alloys containing iron. *Journal of Materials Research* **17**, 2243-2250 (2002).

62 (Thermo-Calc Software AB).

63 Hu, S., Baskes, M., Stan, M. & Chen, L. Atomistic calculations of interfacial energies, nucleus shape and size of θ′ precipitates in Al–Cu alloys. *Acta materialia* **54**, 4699-4707 (2006).

64 Dieter, G. E. & Bacon, D. J. *Mechanical metallurgy*. Vol. 3 (McGraw-hill New York, 1986).

65 Pink, E. Physical significance and reliability of Larson–Miller and Manson–Haferd parameters. *Materials science and technology* **10**, 340-346 (1994).

66 Luster, J., Thumann, M. & Baumann, R. Mechanical properties of aluminium alloy 6061–Al2O3 composites. *Materials science and technology* **9**, 853-862 (1993).

67 Kandare, E., Feih, S., Lattimer, B. & Mouritz, A. Larson–Miller failure modeling of aluminum in fire. *Metallurgical and materials transactions A* **41**, 3091-3099 (2010).

68 Samuel, K. & Ray, S. Larson–Miller correlation for the effect of thermal ageing on the yield strength of a cold worked 15Cr–15Ni–Ti modified austenitic stainless steel. *International journal of pressure vessels and piping* **83**, 405-408 (2006).

Appendices

Appendix 1 - Heat treatment trials

This appendix entails the microstructures at different stages of heat treatment as discussed in Section 4.1. Table A1.2 shows the microstructures at different stages of solution treatment. Table A1.3 and table A1.4 shows the microstructures at different times during aging at 170ºC and 205ºC respectively. All the microstructures are stored in: *VOLS10260879\Heat treatment\Microstructures*. Efforts were taken to image the precipitates using an FEG-SEM. The SEM images can be found in: *VOLS10260879\Heat treatment\SEM.*

Table A1.2. *Microstructures at various times during Solution treatment(Etchant: Keller's reagent)*

Time	**s_0 hours(As-cast)**	**s_1 hours**
Microstructure (1000x)	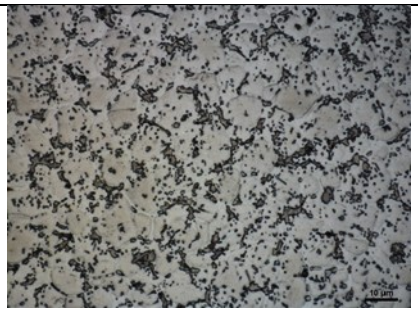	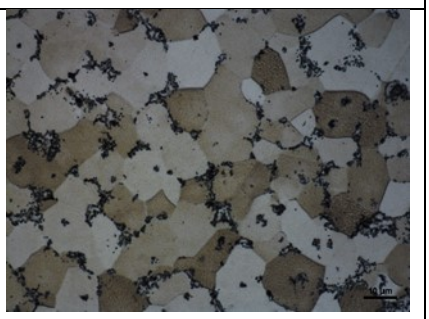
Time	**s_2 hours**	**s_3 hours**
Microstructure (1000x)	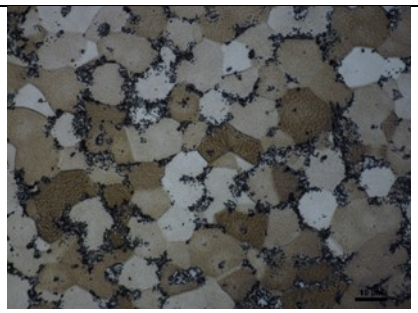	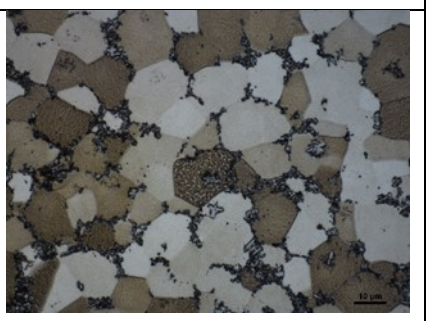
Time	**s_4 hours(End of Solution treatment)**	
Microstructure (1000x)	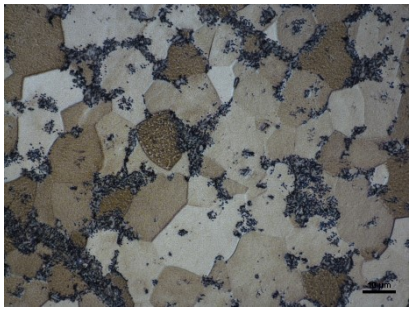	

Table A1.3. *Microstructures at different aging times at 170°C*

Time	**a_1 hours**	**a_2 hours**	Without relaxation(6 h)
Microstructure (1000x)	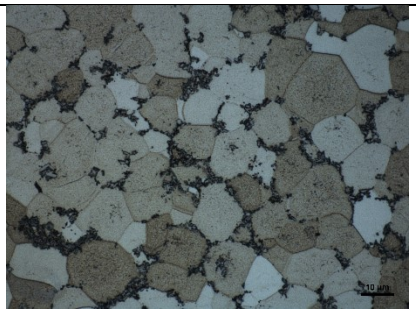		
Time	**a_3 hours**	**a_4 hours**	
Microstructure (1000x)	-	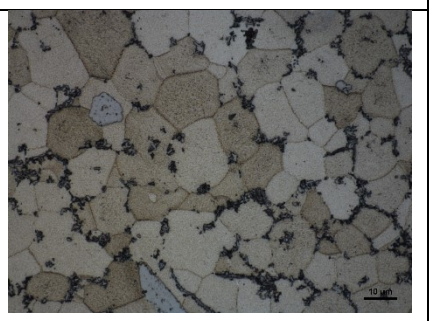	
Time	**a_1 hours**	**a_2 hours**	With relaxation(6 h)
Microstructure (1000x)	-	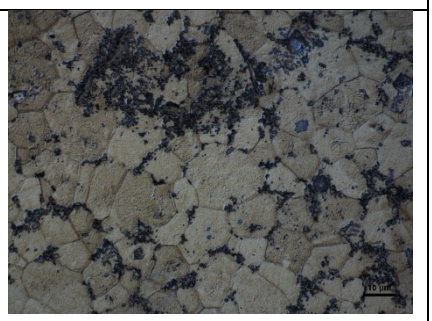	
Time	**a_3 hours**	**a_4 hours**	
Microstructure (1000x)	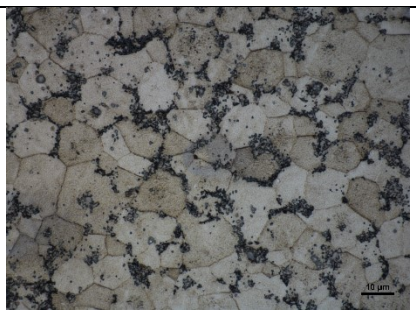	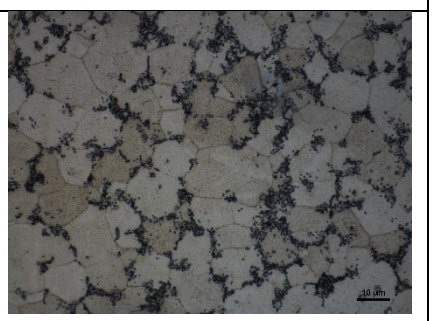	

Table A1.4. Microstructures at different aging times at 205°C

Time	**b_1 hours**	**b_2 hour**	Without relaxation(6 h)
Microstructure (1000x)	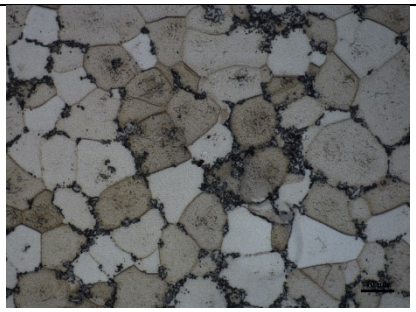	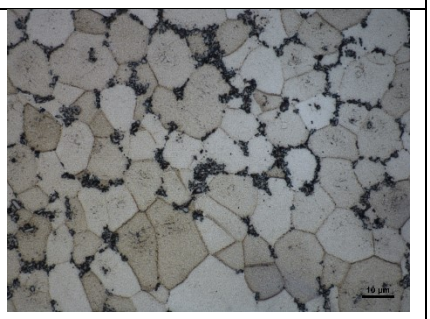	
Time	**b_3 hours**	**b_4 hours**	
Microstructure (1000x)	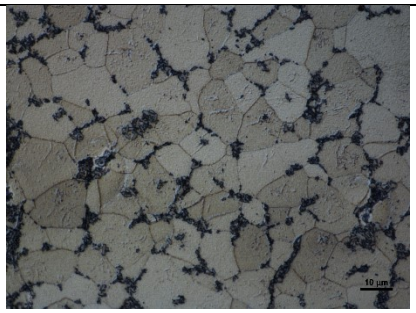	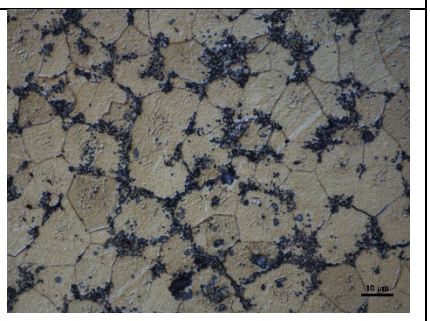	
Time	**b_1 hours**	**b_2 hour**	With relaxation(6 h)
Microstructure (1000x)	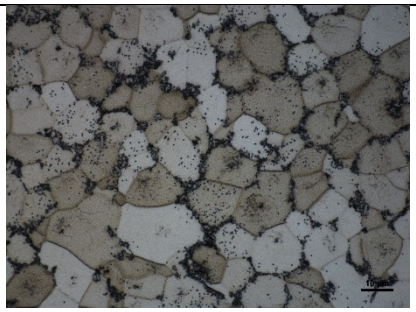	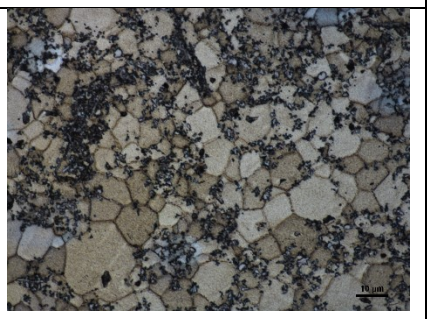	
Time	**b_3 hours**	**b_4 hours**	
Microstructure (1000x)	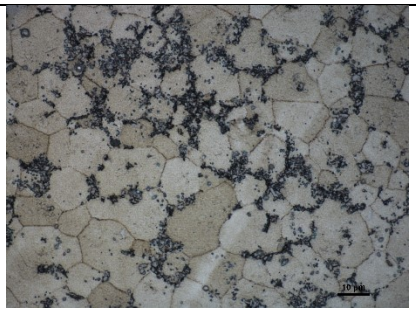	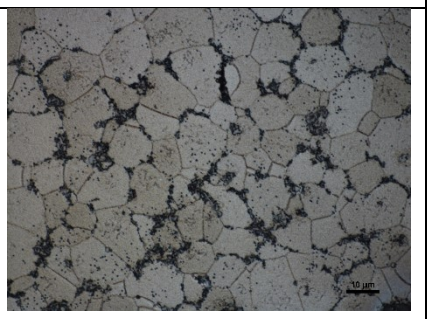	

Appendix 2 – Prolonged Thermal Exposure

This appendix entails the microstructures of T7 heat treated A205 before and after prolonged thermal exposures at 150ºC and 200ºC as discussed in Section 4.2.

Table A2.1. *Microstructures(100x) before and after 100 hours and 1000 hours of thermal exposure at 150ºC and 200ºC*

Time	**T7 heat-treated A205**	
Microstructure (100x)	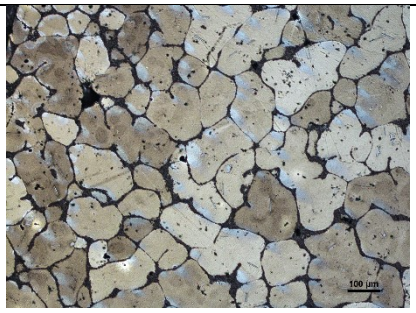	
Exposure time at 150ºC	**100 hours**	**1000 hours**
Microstructure (100x)	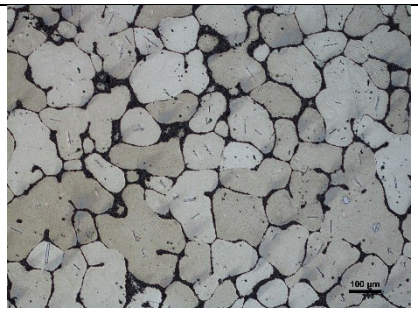	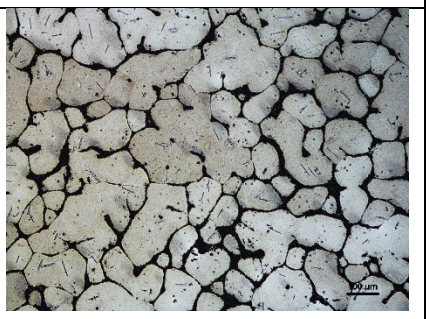
Exposure time at 200ºC	**100 hours**	**1000 hours**
Microstructure (100x)	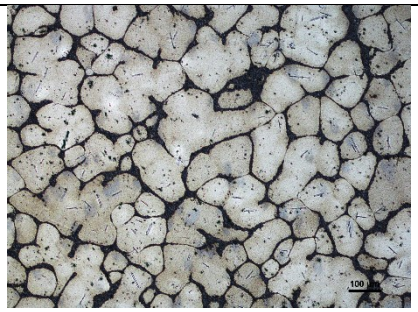	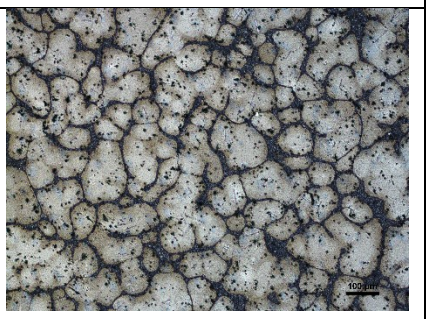

Table A2.2. *Microstructures(1000x) before and after 100 hours and 1000 hours of thermal exposure at 150°C and 200°C*

Time	**T7 heat-treated A205**	
Microstructure (100x)		
Exposure time at 150°C	**100 hours**	**1000 hours**
Microstructure (100x)	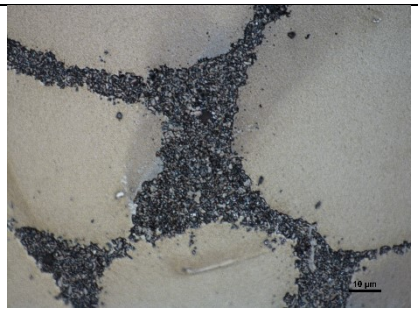	
Exposure time at 200°C	**100 hours**	**1000 hours**
Microstructure (100x)		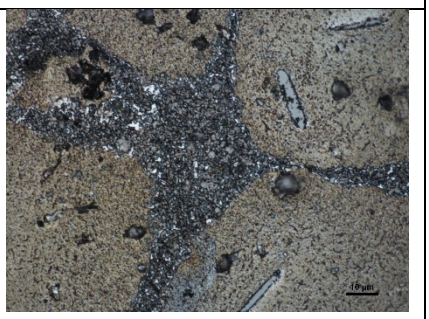

All the microstructures captured are stored in: *VOLS10260879\Tensile properties\Microstructures*

The small white phases seen in high magnification in the grain boundaries are suspected to be the Fe-rich intermetallic phase. As discussed in Appendix 4, the iron-content in these specimens was quite high. Tensile tests were done on specimens with and without silver. Although the mechanical properties with the presence of silver were significantly better, no conclusive proof could be provided by fractography. The results can be found in the internal document VOLS:10216255. The ID of specimens chosen for investigation can be related to the thermal exposure and testing conditions as mentioned in: *VOLS10260879\Tensile properties\Tensile specimens.xlsx*

The results from stereo-microscopy of fractured surfaces are stored in: *VOLS10260879\Tensile properties\Fractography\VHX*. Fractographs from SEM are stored in: *VOLS10260879\Tensile properties\Fractography\SEM*. Results from EDS analysis performed on microstructural features and defects present are stored in: *VOLS10260879\Tensile properties\EDS*. The captured images of $CuAl_2$ precipitates at different thermal exposure conditions are stored in: *VOLS10260879\Tensile properties\Precipitates\Images*. The specimen IDs corresponding to the heat-treatment or testing condition can be retrieved using: *VOLS10260879\LCF properties\Specimens.xlsx*

Appendix 3 – LCF tests

This appendix entails the microstructures of specimens from LCF testing as discussed in Section 4.3. There are three batches of specimens – Batch A, Batch B and Batch C which were solutionized aged to different times. The microstructures of different batches at different aging times are summarized in Table A3.1.

Table A3.1. *Microstructures(100x) of different batches(A, B and C) of specimens at different aging times used for LCF testing*

Batch A	**After a_1 hours of aging at 170°C**	**After a_3 hours of aging at 170°C**
		
Batch B	**After a_2 hours of aging at 170°C**	**After a_4 hours of aging at 170°C**
	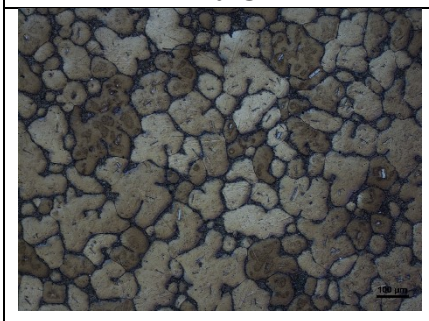	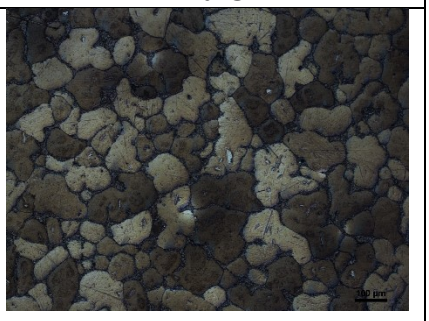
Batch C	**After a_4 hours of aging at 170°C(complete T7 heat treatment)**	
	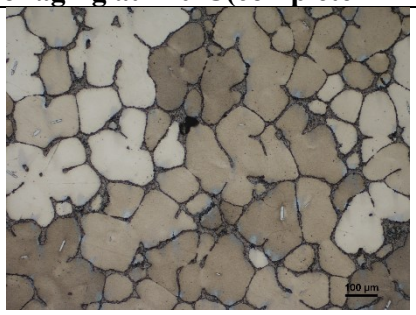	

Presented in table A3.2 are some results of EDS analysis of defects that had initiated the fatigue crack proving that the initiators were mostly oxides.

Table A3.2. *EDS Analysis on oxide inclusions*

Element	**O**	**Cu**	**Al**	**Ti**	**Mg**
Weight%	5.95	3.07	47.49	43.49	-
	1.77	6.49	70.13	21.62	-
	2.33	4.44	70.51	22.72	-
	8.71	2.85	53.5	30.9	4.03

All the EDS results can be found in the directory: *VOLS10260879\LCF properties\EDS*

Appendix 4 - Chemical analysis of A205 specimens tested

Figure A4.1 shows the results from OES(Optical Emission Spectroscopy) analysis of A205 specimens used for different batches. The results are compared against the minimum and maximum values as mentioned in AMS4471 specification. The results suggest that the chemical composition has not been the same for all the batches of specimens tested. The specimen batches correspond to the results discussed in Chapter 4 as:

1. 'Heat treatment' – As discussed in Section 4.1

2. 'Prolonged thermal exposure' – As discussed in Section 4.2

3. 'Batch C' and 'Batch A – LCF test' – As discussed in Section 4.3

In all the batches, the amount of trace elements exceeded the maximum value dictated by AMS4471. Especially in the specimens that were tensile tested after prolonged thermal exposures, the amount of iron detected was abnormally high. The amounts of titanium detected were also lesser than the minimum amount mentioned in the specification.

Clearly there is a need for standardizing the chemistry of A205.

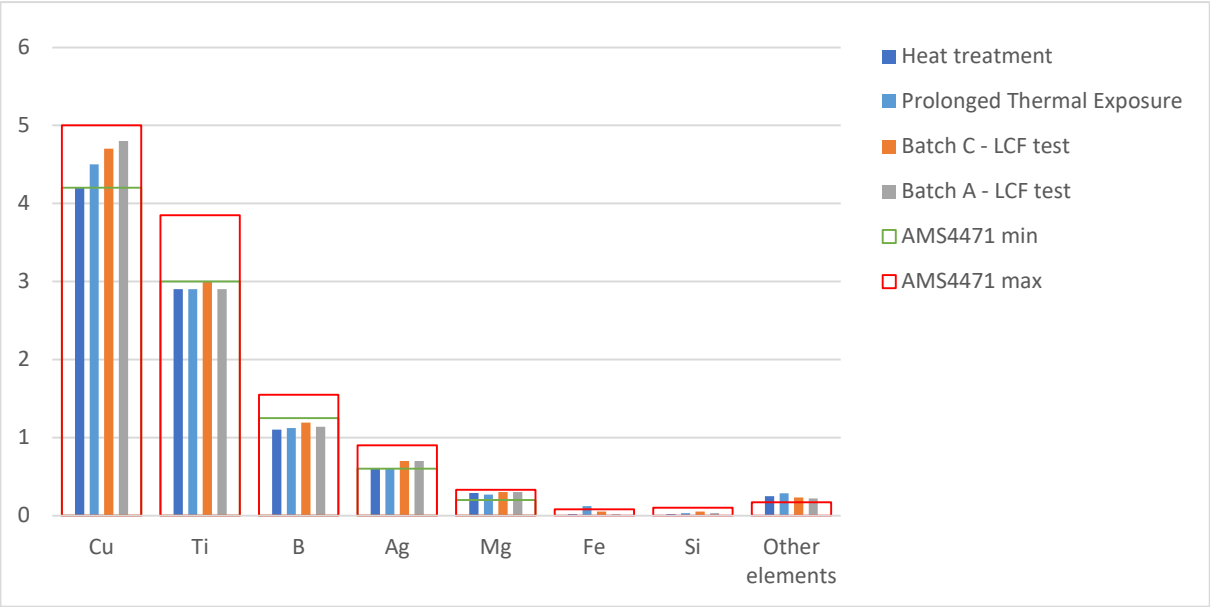

(a)

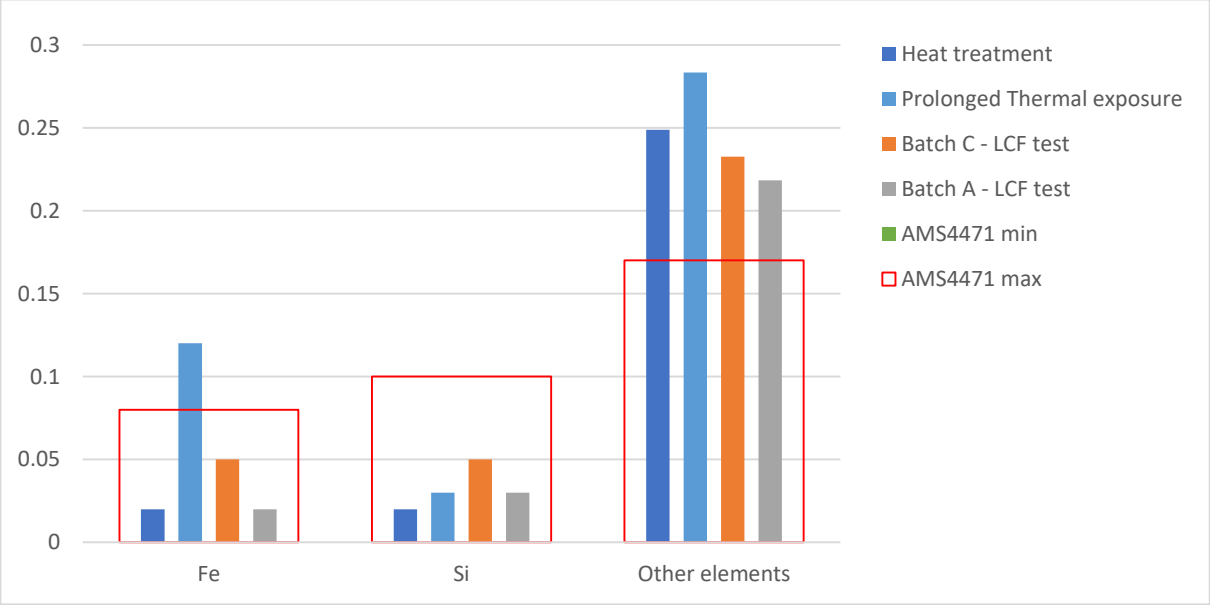

(b)

Figure A4.1. *Chemical analysis of various batches of specimens used for testing - (a) All elements (b) Trace elements*